THE USE OF SURFACE ENHANCED RAMAN SPECTROSCOPY (SERS) FOR BIOMEDICAL APPLICATIONS

A Dissertation

by

MUSTAFA HABIB CHOWDHURY

Submitted to the Office of Graduate Studies of
Texas A&M University
in partial fulfillment of the requirements for the degree of

DOCTOR OF PHILOSOPHY

December 2005

Major Subject: Biomedical Engineering

THE USE OF SURFACE ENHANCED RAMAN SPECTROSCOPY (SERS) FOR BIOMEDICAL APPLICATIONS

A Dissertation

by

MUSTAFA HABIB CHOWDHURY

Submitted to the Office of Graduate Studies of
Texas A&M University
in partial fulfillment of the requirements for the degree of

DOCTOR OF PHILOSOPHY

Approved by:

Chair of Committee,	Gerard L. Coté
Committee Members,	Lihong Wang
	Kenith Meissner
	Henry F. Taylor
Head of Department,	Gerard L. Coté

December 2005

Major Subject: Biomedical Engineering

ABSTRACT

The Use of Surface Enhanced Raman Spectroscopy (SERS) for Biomedical Applications.

(December 2005)

Mustafa Habib Chowdhury, B.S., Purdue University;

M.S., California State University, Long Beach

Chair of Advisory Committee: Dr. Gerard L. Coté

Recent advances in nanotechnology and the biotechnology revolution have created an immense opportunity for the use of noble metal nanoparticles as Surface Enhanced Raman Spectroscopy (SERS) substrates for biological sensing and diagnostics. This is because SERS enhances the intensity of the Raman scattered signal from an analyte by orders of 10^6 or more. This dissertation deals with the different aspects involved in the application of SERS for biosensing. It discusses initial studies performed using traditional chemically reduced silver colloidal nanoparticles for the SERS detection of a myriad of proteins and nucleic acids. It examines ways to circumvent the inherent aggregation problems associated with colloidal nanoparticles that frequently lead to poor data reproducibility. The different methods examined to create robust SERS substrates include the creation of thermally evaporated silver island films on microscope glass slides, using the technique of Nanosphere Lithography (NSL) to create hexagonally close packed periodic particle arrays of silver nanoparticles on glass substrates as well as the use of optically tunable gold nanoshell films on glass substrates.

The three different types of SERS surfaces are characterized using UV-Vis absorption spectroscopy, Electron Microscopy (EM), Atomic Force Microscopy (AFM) as well as SERS using the model Raman active molecule *trans*-1,2-bis(4-pyridyl)ethylene (BPE). Also discussed is ongoing work in the initial stages of the development of a SERS based biosensor using gold nanoshell films for the direct detection of β-amyloid, the causative agent for Alzheimer's disease. Lastly, the use of gold nanoshells as SERS substrates for the intracellular detection of various biomolecules within mouse fibroblast cells in cell culture is discussed. The dissertation puts into perspective how this study can represent the first steps in the development of a robust gold nanoshell based SERS biosensor that can improve the ability to monitor biological processes in real time, thus providing new avenues for designing systems for the early diagnosis of diseases.

DEDICATION

All religions, arts and sciences are branches of the same tree. All these aspirations are directed toward ennobling man's life, lifting it from the sphere of mere physical existence and leading the individual towards freedom.

- Albert Einstein

This dissertation is dedicated to my family

ACKNOWLEDGEMENTS

I would like to thank the Food and Drug Administration (FD-U-002091), the National Institutes of Health (NIH-STTR- 1R41AG025586-01), and the Whitaker Foundation for providing the funds to carry out the research covered in this dissertation. I would also like to thank my committee for their patience, guidance and understanding throughout the years. I would like to specifically express my deepest gratitude to Dr. Theresa Good for the guidance and insight she gave me all these years. A special thank you goes to Dr. Gerard Coté, my advisor, without whom none of the accomplishments documented in this dissertation would have been possible. He has been an outstanding mentor and a great friend throughout my stay at Texas A&M University.

On a personal note, I would like to express my most sincere gratitude to my family whose love, sacrifice and dedication are the biggest reasons behind all my success. They will always be a source of great inspiration in my life. I will always keep to heart my father's simple advice which is to try to understand and celebrate the Creator in every fabric of existence. That has been the strongest guiding force in my life. I would like to express my warmest love and gratitude for my dearest friend Sabrina, whose mere presence has given me the strength and inspiration to be myself. Words fail to express how lucky I feel to have her by my side.

And finally I would like to express my gratitude and support for all the genuine electronic music DJ's, producers, promoters and connoisseurs. It is your passion, creativity, honesty and dedication that has given me the strength to believe in magic.

TABLE OF CONTENTS

CHAPTER Page

CHAPTER Page

LIST OF FIGURES

FIGURE Page

FIGURE Page

FIGURE Page

FIGURE Page

FIGURE Page

LIST OF TABLES

CHAPTER I

INTRODUCTION

Traditional dispersive Raman spectroscopy is an inefficient modality for the detection of bioanalytes. This is due in part to the relatively low number of Raman scattered photons compared to Rayleigh scattered ones (typical Rayleigh scattering cross sections of molecules are in the range of $\sigma = 10^{-26}$ cm^2 and typical Raman scattering cross sections are in the range of $\sigma = 10^{-29}$ cm^2).[1] The scattering cross section of a particle is defined by relating the rate of photons striking a molecule to the rate of scattering in all directions.[1] Hence it can be viewed as an area presented by a molecule for the scattering of incident photons and will be described in detail in a later section of this dissertation. Broadband fluorescence signals of much higher intensity than the Raman signals are often generated by the molecule of interest as well as other surrounding molecules (typical fluorescence cross sections of molecules is in the range of $\sigma = 10^{-19}$ cm^2).[1] These factors demand the use of highly sophisticated equipment in order to use Raman spectroscopy for analyte detection at trace levels.

Surface Enhanced Raman spectroscopy (SERS) is a technique developed more recently which has been used quite successfully to enhance the Raman signal of a molecule by factors of 10^6 or more.[2-11] This is done by using low to medium powered lasers to excite vibrational transitions in molecules adsorbed on a rough metallic surface.

This dissertation follows the style and format of the *Journal of Biomedical Optics*.

The metallic surface can be in the form of a thin layer of the metallic island film on an electrode or glass slide, or in the form of aqueous colloidal nanoparticles. Typical metals used for SERS are gold, silver and copper. The exact nature of the enhancement of Raman signals through SERS is not fully understood but appears to be caused by two contributing mechanisms of enhancement, namely the electromagnetic mechanism and the chemical mechanism. These will be discussed in greater detail in the appendix section of this dissertation. SERS is an attractive tool for biomedical applications because it has several advantages over competing optical techniques. They are: (i) minimal sample preparation required for SERS tests; and (ii) weak Raman scattering of hydroxyl groups which means that water and silica do not manifest themselves as serious sources of background noise. As a result, biological samples can be tested in aqueous media using commercially available glass substrates.

SERS has been used for the development of ways to study biologically relevant molecules and events. One of the most widely used substrate for SERS has been water based silver and gold colloidal nanoparticles. This is primarily the case as they are relatively easy to prepare. Silver colloidal particles prepared by reduction of silver nitrate with sodium borohydride and sodium citrate respectively according to the protocol prescribed by Lee and Meisel [12] has been used as SERS substrates to study a variety of aromatic and aliphatic amino acids in order to determine the specific Raman bands associated with these molecules in physiologically relevant conditions.[13-15] Others have used aqueous gold colloidal nanoparticles as SERS substrates to study the effects of changes in pH on the adsorption of solutions of amino acids and their polymers to the

colloids and to monitor the strength and variation of the SERS signal with pH.[16-17] This gives insight into the nature of attachment of the amino acids and their corresponding polymers to the colloidal surface and hence provides insight on conformational changes that the molecules undergo under different pH conditions. Aqueous metal colloidal nanoparticles have also been used extensively to study the SERS spectra of various proteins as well the nature of interaction of drugs with different proteins such as the interaction of the antiretroviral drug hypericin with serum albumins.[18-22] This biomedical application for SERS has the potential to be of crucial importance in the development of new drugs for curing a variety of fatal diseases.[21-22]

Colloidal metal nanoparticles have also been extensively used as SERS substrates for the characterization and detection of individual nucleosides, oligonucleotides and nucleic acids at physiologically relevant concentrations.[23-27] Graham *et al.* have been able to use modified DNA and novel aggregating agents for silver colloids to detect DNA down to concentrations of 8×10^{-13} M.[28] The increased sensitivity of this SERS detection technique offers two advantages: first it circumvents the need for any amplification step which is a marked improvement when compared to traditional fluoresence and polymerase chain reaction (PCR) amplification based DNA detection techniques. Secondly the sharp peaks associated with the SERS spectra are easier to detect and analyze when compared with broadband fluorescent signals and thus opens the road for a greater degree of multiplexing.[28] Kneipp *et al*. have also been successful in using colloidal gold and silver clusters as SERS substrates in conjunction with various statistical algorithms to detect single molecules of the base adenine and its

nucleotide.[29-30] Others have used metal colloidal nanoparticles as SERS platforms to study the differences in structure and nature of adsorption of intrinsically "straight", "bent" and "kinked" oligonucleotides.[31] There have been several studies that report the use of colloidal gold nanoparticles to detect native chemical constituents of cells such as various DNA and protein constituents inside cells [32-33] as well as the use of novel aggregated gold nanoparticle coated SiO_2 chips to detect various strains of Gram-positive and Gram-negative bacteria.[34]

SERS have also been used for the creation of microarray type gene probes for the detection of cancer [35-37] as well as in a variety of ELISA (enzyme-linked immunosorbent assay) like techniques for the detection of mouse IgG [38] and the enzymes prostaglandin H synthatase-1 and -2 in normal human hepatocytes and human hepatocellular carcinoma (HepG2) cells.[39] These techniques adapt a regular ELISA type assay by replacing the chromogenic read out of the enzyme reaction with nanoparticle based SERS detection. Another group of studies reported the application of a novel class of SERS active nanostructures for biodetection.[40-42] These studies use an initial gold nanoparticle bound to both a Raman reporter molecule (giving signal specificity) and a protein (which acted as the bioreconition element). After binding of this conjugate with the target analyte, electro-less deposition techniques were employed to develop a silver shell around the gold seed in a process termed 'silver enhancement'. The gold seed is used as it generally binds well many biological molecules via oxidation of the surface thiol groups thus giving the necessary specificity for the secondary silver layer. This silver layer possessed the required size and nanoscale surface roughness to provide

efficient SERS enhancement from the reporter molecule. This seeded growth method has been used for nucleic acid detection as well as extended to protein detection in cell and tissue.[40-42] Innovative application of SERS have been reported by Mulvaney *et al*. [43] and Doering *et al*. [44] which used nanoparticles bound to a Raman reporter molecule like Rhodamine 6G and encapsulated by silica in multiplexed bioassays. The encapsulated particles were stable in the presence of high salt (common in biological buffers) because the silica protected the nanoparticles from the environment as well protected the environment from the potentially toxic reporter molecule. This review of current literature goes to show the tremendous potential for the application of SERS in biomedical research.

The major contribution of this dissertation to the field of biomedical science/engineering is an attempt to investigate ways in which SERS can be applied to solve biomedically relevant problems. This includes both the fabrication and characterization of several SERS platforms for potential use in biosensors. It also deals with using one such SERS active substrate (gold nanoshells) for the development a biosensor for the direct detection of β-amyloid proteins as well as the intracellular detection of cell constituents.

This dissertation will begin with early work done in the Optical Biosensing Laboratory at Texas A&M University using chemically reduced colloidal silver nanoparticles for the detection of differences in SERS spectra between α-helical and β-sheet proteins, single stranded DNA and double stranded DNA and two different forms of human integrins that are present in vascular smooth muscle cells (VSMC). This work

was done as proof of concept preliminary studies with the ultimate goal of developing biosensors for certain proteins and DNA using silver colloidal particles. Although the colloids were successful in generating unique SERS spectra of the target analytes of interest, the reproducibility problem due to the need for their aggregation to provide the necessary plasmonic conditions for optimal SERS enhancement was quickly revealed. That set off the search for the development of robust SERS platforms with plasmonic properties that are not based on any aggregation mechanism. It was this search that led to the work that forms the fundamental basis of this dissertation. This dissertation explores ways to circumvent the aggregation problem by fabricating and characterizing solid phase SERS substrates of nanometer scale silver island films deposited on glass substrates via thermal evaporation. It also reports on early work done by using the technique of Nanosphere Lithography (NSL) to create ordered periodic particle arrays of silver nanoparticles on glass substrates with controllable morphological and optical properties. It will then report on work done in simulating the optical properties of the NSL based silver surfaces. Another solid phase SERS substrate that this dissertation characterizes is the gold nanoshell film on glass substrates that has been fabricated by Nanospectra Biosciences Inc (Houston, TX), a collaborator with the Optical Biosensing Laboratory (OBSL) at Texas A&M University. Nanoshells are unique particles made of a dielectric core and an outer metallic shell layer. It has the unique property of having a highly tunable surface plasmon resonance wavelength from the visible through the near-infrared and thus can be potentially useful for biomedical sensing and therapeutics. This tunability is achieved by varying the ratio of the core diameter to the shell thickness. The

dissertation will discuss the theoretical principles behind the nature of gold nanoshells. The dissertation then proceeds to report on work done in laying the foundation for the creation of a novel SERS based biosensor using gold nanoshell films for the direct detection of beta-amyloid proteins (the causative agent of Alzheimer's disease) in physiological buffer. Currently there is no definitive diagnosis for the detection of beta amyloid proteins. Most of the current methods that are being developed to test for beta amyloid involve several indirect imaging modalities and other complex detection techniques which are not definitive to beta amyloid. In many cases they also involve several intermediate amplification steps which are cumbersome, unreliable and technically demanding. This makes it unsuitable for implementation in a normal clinical setting. It is hoped that the research presented in this dissertation will lead to the development of a definitive SERS based biosensor for beta amyloid which can be implemented in a normal clinical setting without the need of highly qualified staff to use the biosensor. This dissertation will also report on the novel use of gold nanoshells for the detection of various intracellular components in mouse fibroblast cells in cell culture This work is expected to play a crucial role in laying the foundation for the creation of SERS based intra-cellular biosensors which can be functionalized and engineered to probe specific cell organelles and/or target specific intracellular biochemicals.

CHAPTER II

SERS BIOSENSING WITH COLLOIDAL SILVER NANOPARTICLES

Introduction

The intent of this early work using metal colloidal nanoparticles for the detection of several different proteins and nucleic acids was for proof of concept to see if SERS could indeed be used to detect these bioanalytes under physiological conditions. In the following experiments, citrate reduced silver colloidal nanoparticles prepared according to a modified version of the Lee and Miesel method [12] were successfully used to obtain SERS spectra of native and thermally denatured bovine serum album (BSA), which served as model molecules for α-helical and β-sheet proteins. The long term goal was to be able to develop a biosensor for pathological proteins such as prions which have a highly β-sheet structure. Prion proteins are thought to be the causative agent in transmissible spongiform encephalopathies (TSEs), a group of fatal neurodegenerative diseases that include chronic wasting disease (CWD) and bovine spongiform encephalopathy (BSE) in animals, and Creudzfeld Jakob disease in humans.[45] Until definitive methods of treatment or prevention of the disease have been established, the best hope of preventing the spread of TSEs is through surveillance of animals and animal products including foods and pharmaceutical materials. The diseases are highly contagious in certain species, with transmission from animals to humans thought to be

possible, at least for BSE.[45] Most biorecognition molecules like antibodies that are used in biosensors have a globular structure with high α-helical content. In order for the sensor to be effective, the SERS spectra of the target analyte would have to be distinct from that of the biorecognition molecule, as both would be in close proximity to the metal surface and thus be subjected to the SERS effect. A second goal was to develop a biosensor for the detection of presence of pathogens in food products by detecting the presence of the DNA of the pathogen. One such pathogen is the *Listeria* bacteria. In this regard, the unique SERS spectra of double stranded and single stranded DNA were also obtained where the single stranded DNA served as the model for the biorecognition element and the double stranded DNA served as the model for the DNA probe/target hybrid.

The third and final goal of these early studies were to detect two forms of human integrins that are present in Vascular Smooth Muscle Cells (VSMC) using silver colloids and SERS. This is because integrins are class of cell surface proteins that are involved in various vital physiological functions such as blood clotting, regulation of blood pressure, tissue blood flow, wound healing, gene expression and vascular remodeling.[46-52] The key to integrin functionality is its ability to mediate force transmission by interacting with the extracellular matrix and cytoskeleton. In addition, they play a role in signal transduction via their connection with the proteins in focal adhesion points (FA).[46-52] In order to understand this complex mechanism of cell-cell and cell-extracellular matrix (ECM) adhesion that is responsible for these diverse biochemical interactions, it is necessary to identify the integrins on cells and monitor their interaction with various

ligands. It is hoped that such SERS information, when coupled with force measurements currently obtained using Atomic Force Microscopy (AFM), would hold promise toward helping to elucidate the mechanism of integrin-ligand interactions in vascular smooth muscle cells and could be potentially extrapolated to understand other similar interactions of physiological importance.

Materials and Methods

BSA was purchased from Sigma-Aldrich Inc(St. Loius, MO), and stock solutions of concentration 10 mg/ml (167 μM) were prepared by adding 100 mg of BSA in 10 ml distilled deionized water (18 megaohm/cm). Heating aqueous BSA at 90°C for 6 minutes produced the denatured samples. DNA samples were purchased from Sigma Chemicals, Lot 21K9000, Product No: G2526. The samples were Lambda DNA EcoR I Digest, with a stock concentration of 400 μg/ml. The Storage buffer consisted of 0.1 M EDTA and 0.5 % (w/v) sodium lauryl sulphate (SDS) at a pH of 8.0. The DNA samples were thawed and then roughly 100 μl of the thawed DNA sample was denatured by heating it up to 100 ^{o}C for ten minutes in a test tube immersed in a water bath. The integrin samples tested were purified human integrin αVβ3 and α5β1 (Cat. # CC1021 and CC1027 respectively, Chemicon International, Temecula, CA) in 25 mM Tris-HCl, 150 mM NaCl, 1mM $MgCl_2$, 0.1 mM $CaCl_2$, 100 mM Octyl-β-D-Glucopyranoside buffer, pH = 7.4. Citrate reduced silver colloids were prepared according to a modified protocol found in the literature.[12] All glassware (a 250 ml Pyrex Erlenmeyer flask, a 500 ml Pyrex glass flask with a plastic cap, Pyrex 100 mL and 10 mL graduated cylinder) were

rigorously cleaned with aqua regia (3:1 v/v HCl, HNO_3) under a fume hood, and then rinsed with distilled water, scrubbed with soapy water followed by a final rinse with distilled water. The extinction spectra of the final colloids were taken using a Beckmann DU 640 spectrophotometer in the range of 350 nm – 800 nm using a standard 1 cm path length disposable polystyrene cuvette (VWR International Inc., West Chester, PA). All SERS spectra were collected using a Renishaw System 1000 Raman Spectrometer coupled to a Leica DMLM microscope. The laser used was 514.5 nm Ar^+ laser (Spectra Physics Model 263C) delivering approximately 4.50 mW power to the sample and the SERS data were collected in 180 ^{o} backscattered geometry. A block diagram of the system is shown in Figure 2.1. It involves the incident laser first passing through a beam expander (in order to increase its size so as to fill the microscope objective lens for creating a tighter focus), followed by reflection from a series of mirrors to the first notch filter (NF 1). The notch filter is designed to reject the incident laser line and serves a dual purpose in both reflecting the incident beam to the microscope as well as also rejecting the Rayleigh scattered light in the back reflected beam from reaching the detector. After reflection from notch filter 1, the incident beam then travels through a tunnel connecting the spectrometer to the microscope and strikes the sample. The back reflected light that is scattered from the sample travels via the same path back to the spectrometer to hit notch filter 1 again. As mentioned earlier, the NF 1 rejects the Rayleigh scattered light. The rest of the back reflected beam then passes through a second notch filter (NF 2) which further rejects any Rayleigh scattered light that might have bled through NF 1. The remaining light then passes through a series of lenses and

mirrors to strike a diffraction grating which diffracts the light and then the diffracted light proceeds to strike a thermoelectrically cooled CCD camera.

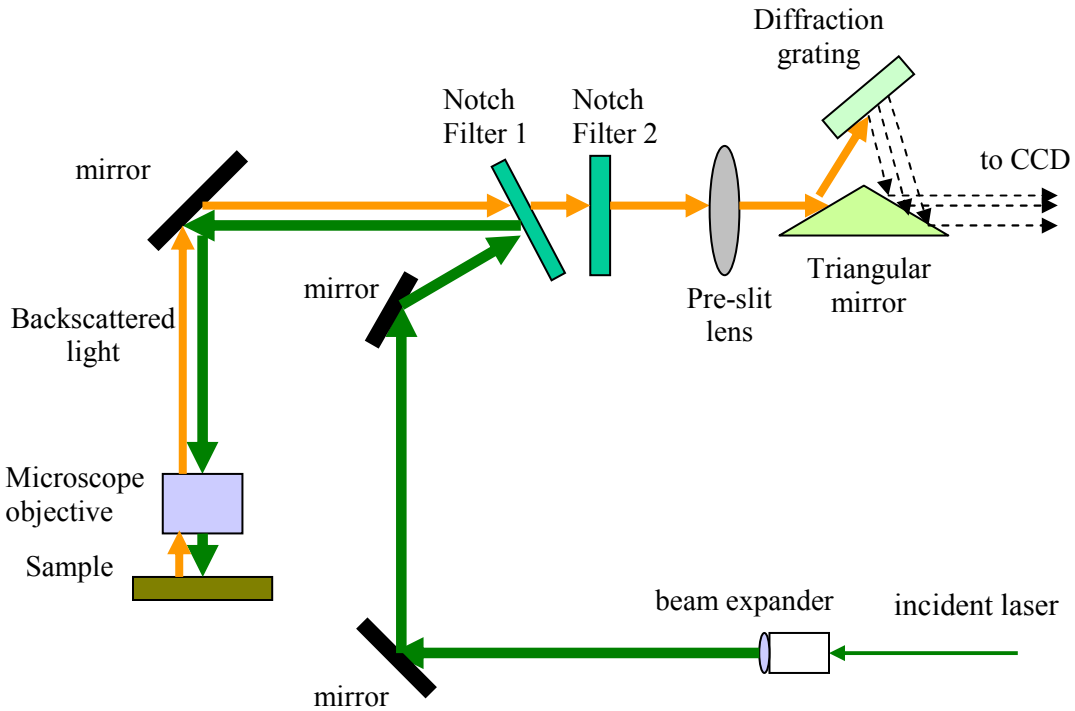

Figure 2.1: Block diagram of the Raman system used to obtain all SERS data presented in this dissertation.

The silver colloidal particles prepared above were activated prior to the addition of the analyte by adding 100 µl of 1M NaCl to a glass test tube containing 1 ml of the original colloid. Immediately after this, 500 µl of both the regular and denatured BSA solution was added to the colloid separately bringing the final concentration of the BSA samples to 52 µM. The forming colloidal complex was allowed to sit for approximately 5 min and then 30 µl of this complex was transferred onto a microscope glass slide setup and then the SERS studies were performed.

Samples of the DNA-colloid complex were prepared in a method almost identical to that done previously with the BSA protein, the only difference being that 50 µl of the citrate reduced silver colloid was first activated by 5 µl of 1M NaCl, followed by the separate addition of 20 µl of both the regular and denatured DNA to the colloid bringing the final concentration of the DNA samples to 106 µg/ml. These newly formed complexes were allowed to sit for approximately 5 minutes and then approximately 30 µl of this complex was transferred into a custom built well which consisted of a delcron block into which individual wells were patterned attached on top of a microscope glass slide which acted as a support. The SERS studies were performed with the analytes in these wells.

The samples for the integrin SERS tests were prepared by adding 5 µl of 1M NaCl to 50 µl of the Ag colloid in order to activate it. After uniform mixing, 5 µl of αVβ3 integrin and α5β1 integrin of various concentrations were added respectively to separate aliquots of activated Ag colloid mixtures. These newly formed complexes were allowed to sit for approximately 5 minutes and then approximately 50 µl of this complex was transferred into a custom built well and the SERS studies were performed. The highest concentration of the α5β1 and αVβ3 integrin tested was 131 nM and 122 nM respectively.

Results and Discussion

Of the many colloids available, the citrate reduced silver colloids was the most attractive one primarily due the long term stability of the colloids and the presence of a

layer of citrate ion on the surface of the particle, that controls protein adsorption and prevents any denaturization of the protein once adsorbed on the silver particle.[53] Typical citrate reduced silver colloids are polydispersive, containing spherical, spheroidal and other polygonal three-dimensional structured particles. The silver colloids used in the studies were activated for aggregation prior to the addition of the target analyte with 1M NaCl. Figure 2.2 shows the extinction spectra of the colloidal silver nanoparticles before the addition of salt and after 1 minute, 5 minute and 20 minutes on addition of the salt. The extinction spectrum before addition of salt has a maximum located at 415 nm (spectrum A). The figure clearly shows the change in the profile of the silver nanoparticle once aggregation commences on the addition of salt. It is clearly seen that the value of the extinction at 415 nm drops with time along with the appearance of a new red shifted peak/shoulder. The peak at 415 nm is due to the surface plasmon resonance of single spatially isolated silver colloidal nanoparticles, which occurs due to the collective oscillations of the conduction band electrons in the silver nanoparticle while the red-shifted peak/shoulder is the result of the surface plasmon resonance of aggregated clusters of much larger size. The formation of aggregated clusters translates into a different light scattering/absorption profile of the nanoparticles according to Mie scattering theory and causes the appearance of the new red shifted peak/shoulder.[10, 54] It is worth noting that while the 415 nm peak decreases in magnitude with time (spectra A-D), the new red shifter peak/shoulder increases in magnitude with time from 0 - 5 minutes (spectra A-C) and then drops in magnitude (spectrum D). This is because somewhere between 5 and 20 minutes the size of the aggregated cluster become too

large to remain suspended in water. As a result it starts to settle to the bottom of the cuvette thus leading to an overall drop in the extinction value. It should be noted that the value of the extinction at 514.5 nm (the wavelength of the incident laser for the SERS studies) increases with the extent of the colloidal aggregation between 0 – 5 minutes. This will correspond to greater SERS enhancement and thus 5 minutes was chosen as the time required keeping the samples mixed with the aggregated colloid prior to obtaining any SERS spectra.

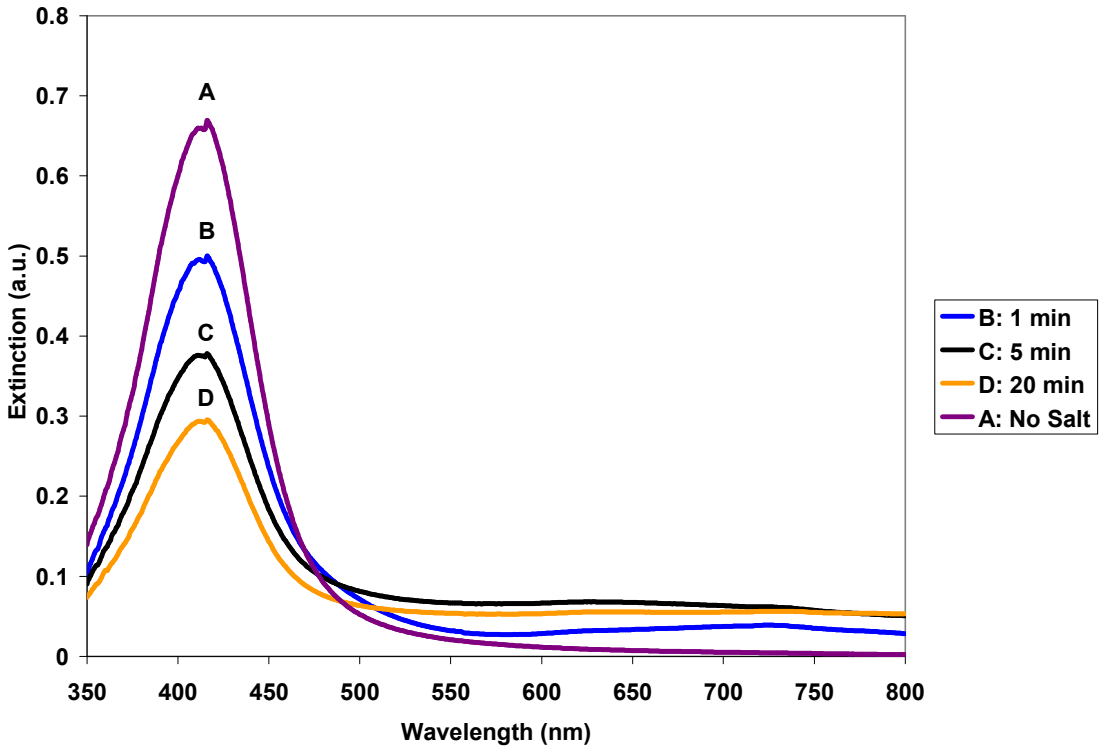

Figure 2.2: Extinction spectra of native silver colloid (A) and at various times after inducing aggregation. Note the magnitude of extinction at 514 nm increases with time on addition of salt.

Figure 2.3(A) shows the SERS spectra of regular BSA (spectrum A), denatured BSA (spectrum B) and the background scan which consists of aggregated colloid only (spectrum C). Bovine serum albumin (BSA) in its native form has a conformation which is approximately 55% α-helix and 45% random coil.[55] A comparison of the spectra in Figure 2.3(A) with other published SERS spectral data for various amino acids, polypeptides and proteins strongly suggests that the sharp peak observed at 1004 cm^{-1} for regular BSA stems from phenylalanine (Phe).[18-19] A possible source which contributes to the appearance of the peak at 1162 cm^{-1} for regular BSA could be the aromatic amino acid tyrosine (Tyr).[13] Denatured bovine serum albumin (BSA) should in all likelihood loose its native stable conformation, thereby, the highly α-helix order of the molecule should be drastically reduced. The absence of any discernable peaks in the 1004 cm^{-1} area at all for denatured BSA suggests that heating indeed brought about a conformational change in the protein structure. The peak located at 960 cm^{-1} might remotely be a weak indication of a β-sheet structure or quite simply a random coil effect.[18, 56] The denatured BSA spectra also shows the appearance of fresh new bands at 1042 cm^{-1} and 1087 cm^{-1}. These are due to changes in protein conformation of either the polypeptide backbone or may also stem from side chain residues. Another source for these peaks could well be the C-C and C-N single bond stretching vibration of the β-sheet backbone.[56] The peaks appearing at roughly 215 cm^{-1} for all three spectra comes from the Ag colloid and shows consistency of the data, thus serving as an internal standard.[19]

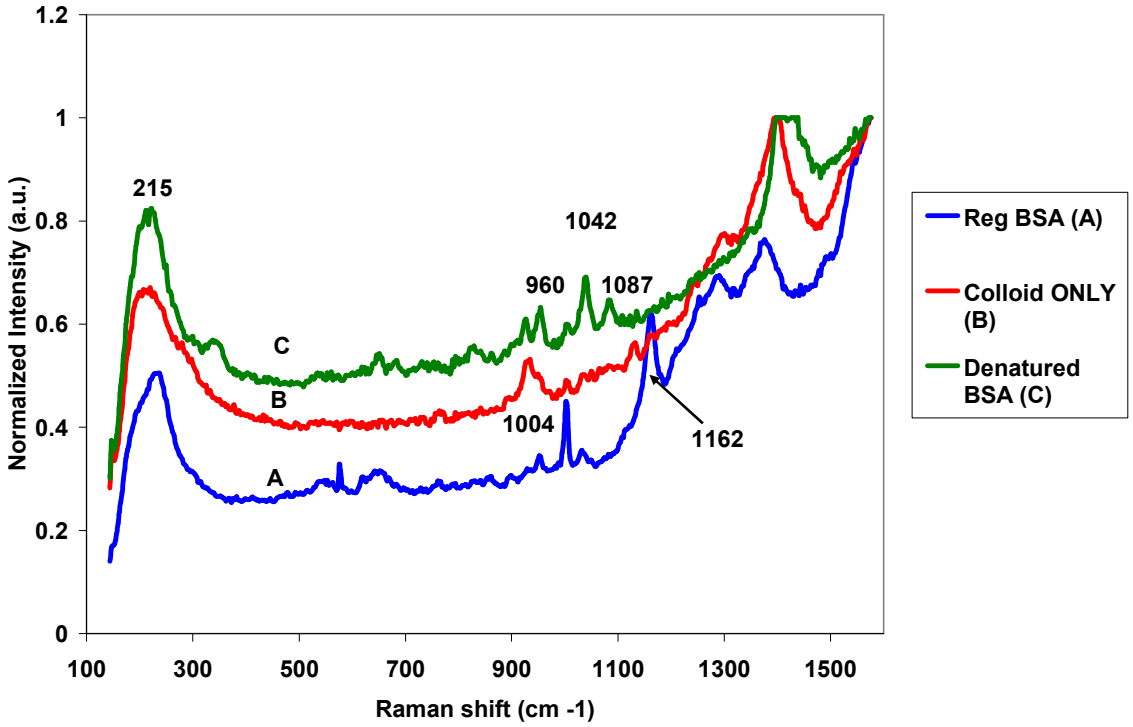

Figure 2.3(A): SERS spectra of regular BSA(A), denatured BSA(C) and background colloidal silver(B).

Regular DNA in its native form is known to have a double stranded helical structure. Once denatured by heating, this highly ordered conformation breaks down into a single stranded random coil structure. Figure 2.3(B) shows the SERS spectra of double stranded regular DNA (spectrum B) and single stranded denatured DNA (spectrum A) on silver colloid as well as the background (spectrum C). Most of the discernable peaks and shoulders in the spectra of the regular double stranded DNA shown in the figure were sitting on top of native colloid spectra. Of these the notable peak and shoulder located at 1393 and 1342 cm^{-1} respectively likely stems from the vibration and stretching modes of the guanine ring. [25] The small peak at 1015 cm^{-1} could be due to dioxyribose-

phosphate vibrations, which provides information on the helical double stranded backbone of the DNA.[57] This is a common region for backbone structural information. The SERS spectrum of denatured DNA showed remarkable differences from that of the spectrum of regular DNA. The strong peak at 733 cm^{-1} indicates the transition from a double helical structure into a disordered single stranded structure at the silver surface and represents the classic adenine peak.[24, 29] The appearance of the strong peaks at 656, 962 and 1467 cm^{-1} can be attributed to the ring vibrating and stretching modes of guanine.[24, 26] The band at 1570 cm^{-1} and the shoulder at 1379 cm^{-1} can be a result of guanine and/or adenine and adenine and/or thymine respectively.[57] This is probably due to the denaturization of the DNA, which has lead to more accessible sites on the single stranded molecule for binding onto the metal substrate, thus yielding a large number of strong peaks in the spectra. Of the various bands present in the SERS spectrum of DNA, it is known that bands due to the vibrations of the bases show highest enhancement.[25] This is due to the presence of double bonds and π-electrons in the rings of the bases, which are more highly polarizable than electrons involved in the single bonds that constitute the bulk of the backbone dioxyribose-phosphate structure. A higher polarizability translates into a stronger SERS enhancement. It seems that guanine generally dominates most of the strong peaks that occur in the SERS spectrum of denatured DNA. This might have something to do with the surface potential of the colloidal silver favoring guanine adsorption over the other bases.[26]

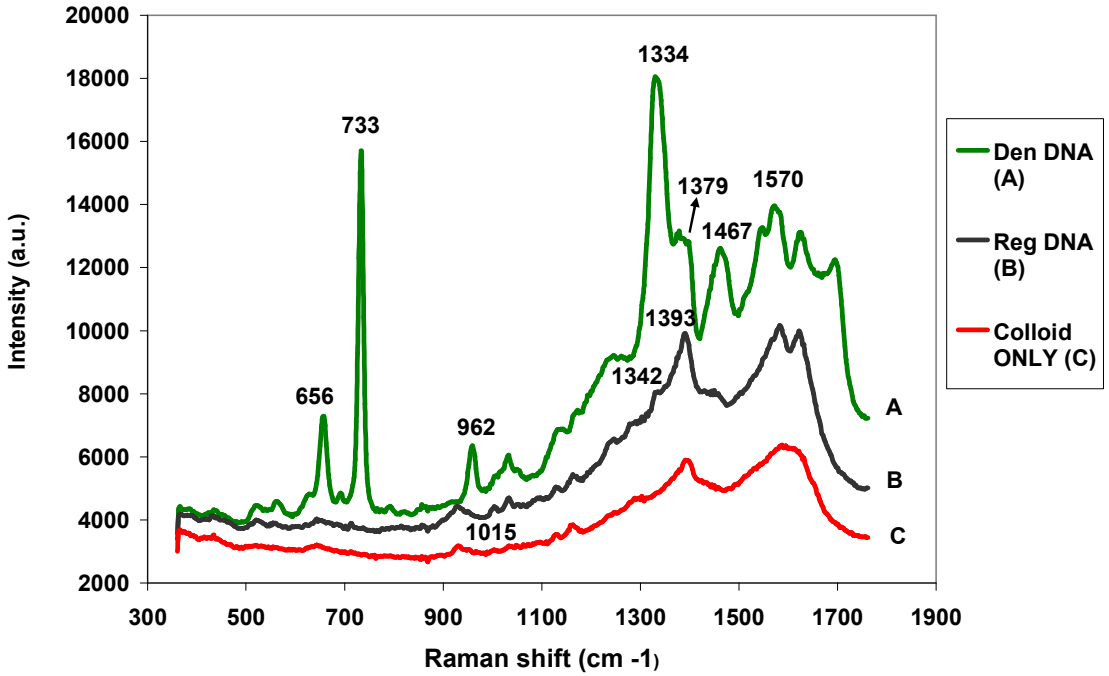

Figure 2.3(B): SERS spectra of regular DNA(B), denatured DNA(A) and background colloidal silver(C).

The baseline corrected and background subtracted SERS spectrum of 131 nM α5β1 integrin is shown in Figure 2.4(A) with the major SERS peak locations marked. A survey of existing literature reveals the bonds that are responsible for the appearance of the SERS peaks. The high correlation between the structural properties of the protein molecule and the location of its SERS peaks makes this technique a powerful tool for the detection of protein structure. The 1645 cm^{-1} peak is the amide I band of the α-helix structure and the 1306 cm^{-1} peak lies in the region of the amide III band for the α-helix structure, thus suggesting that the α5β1 integrin is adsorbed on the colloidal Ag particles in an α-helix region.[18,19] Amide I and III are the peptide backbone modes. The amide I

mode generally has a high contribution from the carbonyl stretching vibration. On the other hand, the amide III mode generally consists of C-N-H in plane bending and C-N stretching modes.[19, 58] The peak located at 1569 cm^{-1} originates from tryptophan and the 1507 cm^{-1} peak is from either phenylalanine or histidine.[18, 19] The peak located at 1359 cm^{-1} can be attributed to tryptophan vibration which is sensitive to the environment of the indole rings.[18,19,58] The fact that this band is so pronounced is indicative of the existence of a hydrophobic environment around the indole rings that is created by the aggregated Ag colloids.[18] The peak located at 1177 cm^{-1} is the result of either tyrosine or phenylalanine and the 1127 cm^{-1} peak can be assigned to the C-N bond stretching vibration.[13,18-20] The 771 cm^{-1} peak can be attributed to either tryptophan or histidine and the 608 cm^{-1} peak can be attributed to phenylalanine.[18-19]

The corrected SERS spectrum of 122 nM αVβ3 integrin is shown in Figure 2.4(B) with the major SERS peak locations marked. Most of the SERS peaks of αVβ3 are identical to that of α5β1 except the four peaks marked in large bold letters located at 1618 cm^{-1}, 1439 cm^{-1}, 908 cm^{-1} and 802 cm^{-1} respectively. The 1618 cm^{-1} peak originates from either of the aromatic amino acids tryptophan, tyrosine or phenylalanine and the Cα-C-N vibration at 908 cm^{-1} along with the location of its amide I and amide III peaks indicates the presence of α-helical structure in αVβ3.[18-19] The 1439 cm^{-1} peak results from the C-H_2 stretching vibrations and the 802 cm^{-1} band also seems to originate from the protein backbone as has been observed previously.[19,58,59] This shows that these two separate integrins adsorb with a different orientation on the surface of the silver

colloid and thus lends credibility to the idea that the two integrins are different in structure.

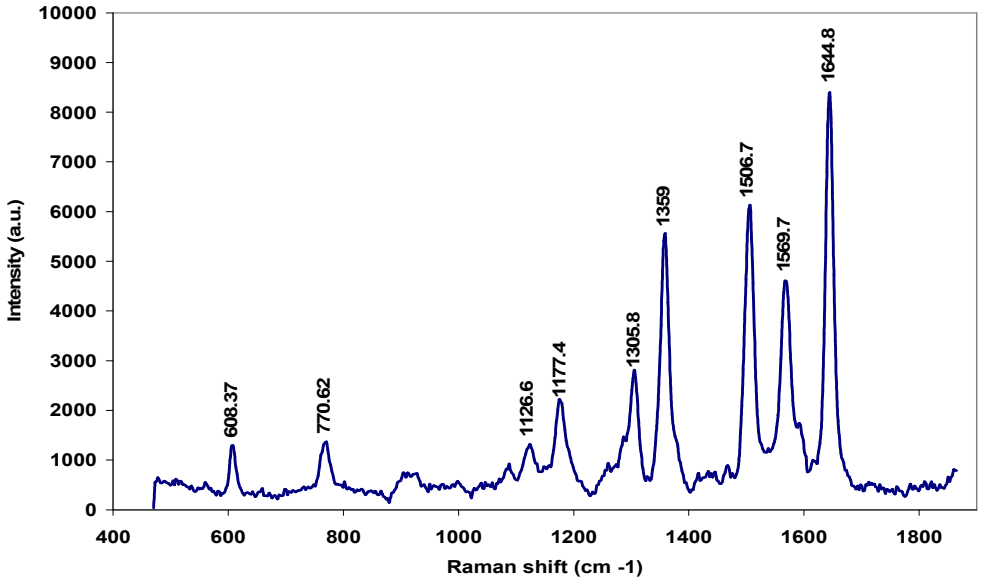

Figure 2.4(A): SERS spectrum of 131 nM α5β1 integrin.

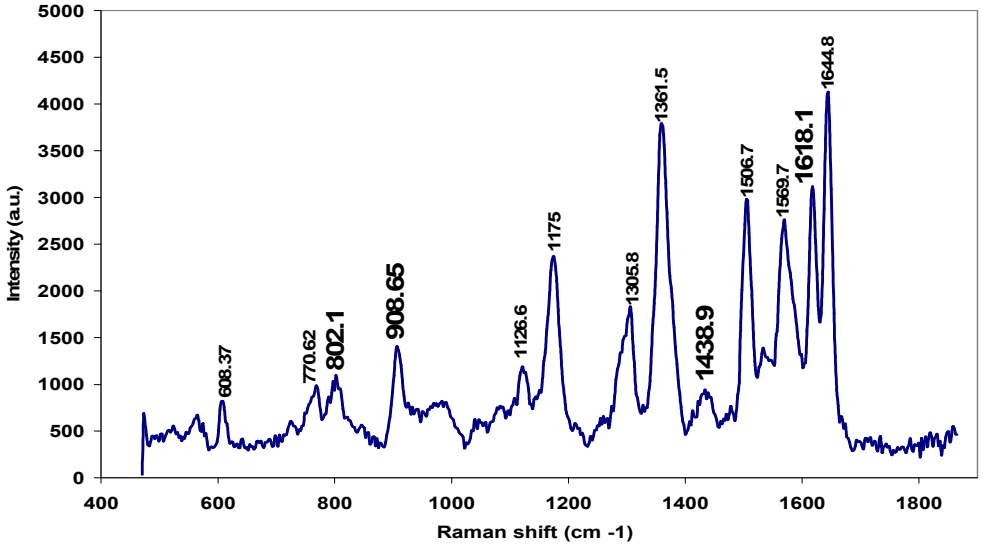

Figure 2.4(B): SERS spectrum of 122 nM αVβ3 integrin.

The SERS results in Figures 2.3(A) - 2.4(B) clearly demonstrate the ability of silver colloidal nanoparticles to provide strong enhancements of Raman signals from bio-molecules adsorbed on its surface. It also shows the ability of the colloidal nanoparticles to distinguish subtle differences between various forms of proteins and nucleic acids. This shows its potential as a powerful tool for the generation of SERS signals from biological molecules. Figure 2.2 however, demonstrates one of the inherent limitations of metal colloidal nanoparticles that compromise their robustness as SERS substrates. The need for aggregation to create the necessary plasmonic conditions for the generation of significant SERS enhancement runs the risk of compromising the reproducibility of SERS data obtained using colloidal nanoparticles. This is because once aggregation commences, the kinetics of the process becomes uncontrollable and sometimes even unpredictable. These limitations make chemically reduced colloidal metal nanoparticles unattractive for potential implementation in biosensors.

CHAPTER III

UNAGGREGATED SERS SUBSTRATES FOR BIOSENSING

Vapor Deposited Silver Island Films on Microscope Glass Slides

Introduction

One way to overcome the problems with colloidal based systems is to develop SERS substrates via vapor deposition of silver onto ultra clean microscope glass slides.[60-65] This is done by the thermal deposition of vaporized silver under high vacuum onto microscope glass slides. The glass slides have to be pretreated to make it extremely clean in order to prevent any particles on it to react with silver and form nucleation sites for silver aggregation. This technique is relatively simple and can be used to produce silver island films of varying amount of thickness. Control of deposition rate, deposition geometry, temperature, post deposition annealing, quality of glass substrate and the rigorousness of the cleaning process are factors that control reproducibility of substrate preparation.[60-63]

The purpose of this study was to develop vapor deposited silver island films onto glass substrates and then characterize their structure and optical properties using UV-Vis absorption spectroscopy, Atomic Force Microscopy (AFM) and SERS. In the case of the SERS studies the strong Raman active molecule *trans*-1,2-bis(4-pyridyl)ethylene (BPE) was used to study the variability of SERS response in different areas of the silver covered slide as well as to observe the overall responsiveness of the substrate to increasing BPE concentrations.

Materials and Methods

Materials

Silver powder 5-8 μm (99.9+%) was used for preparation of the island films and potassium hydroxide (KOH) was used for the slide cleaning step. These items and BPE powder (97%) were purchased from were purchased from Sigma-Aldrich (St. Louis, MO). The microscope glass slides were purchased from VWR Scientific (West Chester, PA).

Microscope Slide Precleaning

The microscope slides were rigorously cleaned by washing them in a 3M KOH solution for at least 90 minutes followed by sonication in deionized water for 5 – 10 minutes. This was followed by sonication in methanol for 5 minutes. A final sonication step in deionized water was performed on the slides. The slides were dried at 110 ^{O} C an hour before silver deposition and allowed to cool for 20 minutes before introduction into the vacuum deposition chamber.

Thermal Deposition of Silver Island Films Under High Vacuum

Silver island films of 5 nm thickness were deposited onto the glass slides using an Edwards Auto 306 Vacuum Coating System in a Class 100 Clean Room at the Materials Characterization Facility at Texas A&M University. The silver deposition rate was controlled by current passing through a molybdenum boat carrying the silver powder. The deposition rate of 0.1 Å/sec (0.01 nm/sec) was established prior to exposing the glass slides to the source. The slow deposition rate allowed the formation of a relatively uniform silver layer. The vacuum inside the metal coating chamber was

maintained in the range of $5 \times 10^{-6} - 1 \times 10^{-7}$ Torr during the deposition process. The thickness of the deposited layer was monitored by an MTM-20 quartz crystal microbalance which was a part of the Metal Deposition chamber. The slides were allowed to cool down for 20 minutes after the end of the deposition process before the vacuum seal was broken with air.

UV-Vis Absorption Studies

The UV-Vis absorption studies were performed using a converted CCD based spectrometer (Spectra Pro 150 Imaging Dual Grating Monochromator/Spectrograph containing a Roper Scientific/Princeton Instruments HAM 256 × 1024 CCD camera) delivering incident light via a 1mm core fiber optic (Thorlabs, Newton NJ) to the sample held in a delron sample chamber built in-house as depicted in Figure 3.1. The collection fiber was a 400 μm core fiber. The light source used was a tungsten halogen lamp (Oriel Systems). Extinction spectra were collected with an integration time of 5 seconds between 360 – 830 nm. A normal clean microscope glass slide was used as a blank for the study.

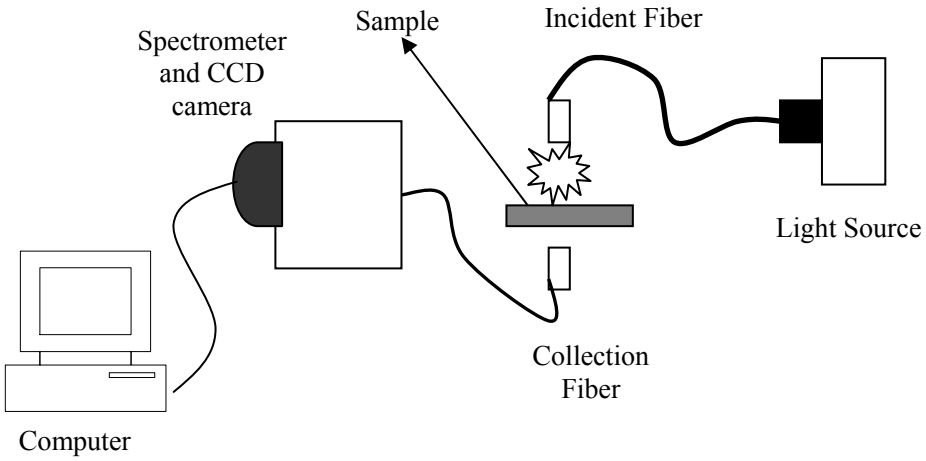

Figure 3.1: Setup for collection of UV-Vis absorption spectra.

Atomic Force Microscopy (AFM) Studies

All AFM studies were done using a Digital Instruments Nanoscope IIIA (Digital Instruments) microscope in tapping mode operation at the Materials Characterization Facility at Texas A&M University. Commercial Si_3N_4 cantilever tips (Digital Instruments) with spring constants of approximately 0.12 nm^{-1} were used. The tips were pyramidal in shape with a cone angle of 70^o and an effective radius of curvature of the tip R_C = 20 – 40 nm. The images presented are raw unfiltered data.

SERS Studies

All SERS spectra were collected using a Renishaw System 1000 Raman Spectrometer coupled to a Leica DMLM microscope. The laser used was 514.5 nm Ar^+ laser (Spectra Physics Model 263C) delivering approximately 4.50 mW power to the sample. The Raman active molecule BPE was used to characterize the silver island films. This was done by dip coating the slide for 1 minute in a solutions of 5, 50 and 500 μM

BPE in acetone and then letting the slides dry for several minutes before obtaining SERS spectra. All SERS spectra were collected with the diffraction grating centered at 1500 cm^{-1} and with an integration time of 5 seconds. The final spectra presented are SERS spectra of BPE with the background (spectra of slide dip coated in acetone only) subtracted upon which a baseline correction routine was performed. The baseline correction routine used was a GRAMS/32 based routine (Galactic Industries Corporation, Salem, NH) which was a built-in feature of the WiRE™ software (version 1.2) that controlled the Raman spectrometer. The BPE studies were also repeated with a set of regular clean microscope slides (with no silver) in order to verify if SERS was actually taking place.

Results and Discussion

Figure 3.2 represents the extinction spectrum of a 5 nm silver coated slide. The spectrum was collected with a 4 second integration time. It can be seen that the extinction maximum (λ_{max}) is located at approximately 514 nm. This shows that the surface plasmon resonance of 5 nm silver island films match exactly with the wavelength of the laser used and is thus optimal for SERS studies. This plasmon resonance wavelength is the result of the collective oscillation of the conduction band electrons of the spatially isolated silver islands and red shifts with increasing thickness of deposition. It was seen that above a thickness of 10 nm silver, the extinction spectrum showed a loss of the appearance of an extinction maximum as well as the loss of SERS properties (data not shown). This has also been observed by other groups [60-62] and is a

result of the silver island films beginning to merge together to form a continuous film at high thicknesses leading to the substrate behaving like bulk silver.

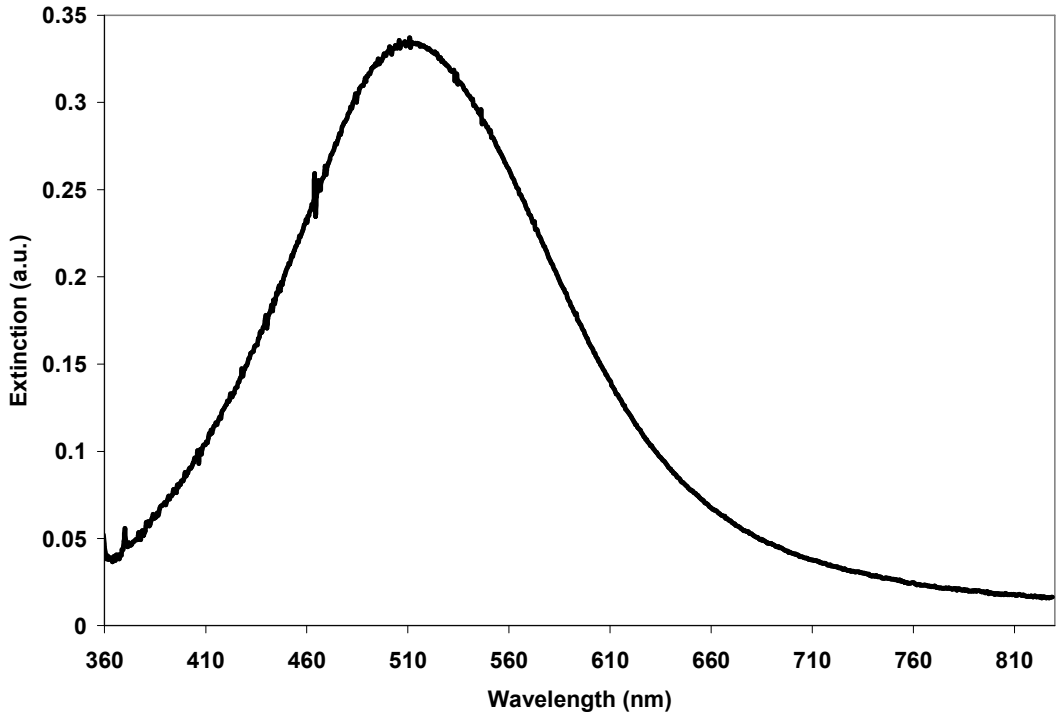

Figure 3.2: Extinction spectrum of 5 nm silver island film on a microscope glass slide.

Figure 3.3 shows a 500 nm × 500 nm AFM image of silver island films on a microscope slide. The image shows that the surface is composed of distinct well separated spherical particles of various sizes. It has been suggested that the shapes and sizes of these islands are dependent upon the migration of the metal atoms on the surface.[62] An independent migration time is associated with each metal atom as it approaches the surface. The structure of the island films is a function of the arrival rate

of atoms on the substrates, which is a function of the deposition rate.[62] Thus, slow deposition rates leads to the formation of well separated isolated metal islands that grow in height. For higher deposition rates this leads to the formation of aggregates of lesser height and particles that are interconnected in a quasi-continuous state.[62] The roughness analysis shows the mean diameter of these islands to be in the range of 60 nm with a mean height of approximately 5.50 nm. A box analysis has also been performed which analyzes the image roughness in the range of roughly 180 × 180 nm. The results of the box analysis are in accordance with the roughness of the entire image. As is clearly demonstrated in the figure, the silver islands are neither uniform in size, shape nor spacing. It is impossible to control these parameters via this technique. This distribution of size, shape and interparticle spacing can at best be minimized by control of the quality of reagents and experimental protocol.

Another inherent limitation of this technique in producing uniform silver island films is depicted in the AFM image of Figure 3.4 which spans a scale of 50 μm × 50 μm. In the image several macroscopic silver aggregates are observed that span the range of 2-5 μm. These silver aggregates can form as a result of several causes, namely dust particles that were not successfully cleaned from the glass slide and the unevenness in the surface of the glass slide. The surface quality of commercially available microscope glass is inhomogeneous with the presence of micrometer sized valleys and pits. These pits and valleys strongly affect the attachment and migration of silver particles on the glass surface and hence also influence the local optical properties.[60-62] Thus the lack of

uniformity at the 500 nm scale and the presence of macroscopic silver aggregates leads to a lack of reproducibility of SERS signals from analytes on such slides.

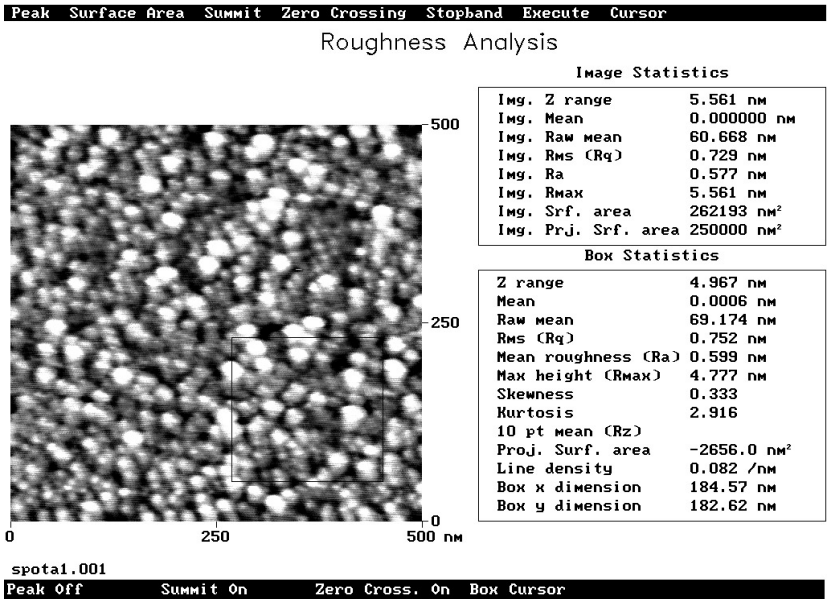

Figure 3.3: Roughness analysis performed on an AFM image of vapor deposited silver island film on a microscope glass slide. Scale of image is 500 nm × 500 nm.

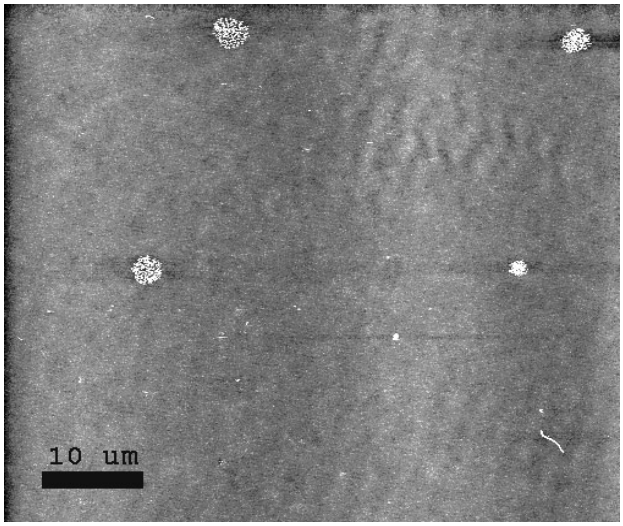

Figure 3.4: AFM image of vapor deposited silver island film on a microscope glass slide. Size of image is 50 μm × 50 μm showing the formation of macro-aggregates.

All of the SERS characterization studies were performed as mentioned above by dip coating the silver coated slides for one minute in varying concentrations (5 μM, 50 μM and 500 μM) BPE solution in acetone and then taking SERS spectra at several spots throughout the slides. Since acetone is quite notorious for the presence of various impurities in it, a background sample was created by dip coating a silver coated slide in similar conditions in the acetone used to make the BPE solution. The spectrum obtained from this sample was then subtracted from all the BPE SERS spectra to get the final BPE spectra.

Shown in Figure 3.5 is a structure of the *trans*-1,2-bis(4-pyridyl)ethylene (BPE) molecule. BPE is well know as a highly Raman active molecule which has pronounced Raman bands at 1635 cm^{-1} and 1605 cm^{-1} due to (C-C) stretching modes, 1201 cm^{-1} due to both stretching and rocking modes of (C_r - C_b) where C_r is a ring carbon attached

to a bridging carbon and C_b is a bridging carbon and 1013 cm $^{-1}$ due to both (C-C) and (C-N) stretching modes.[66]

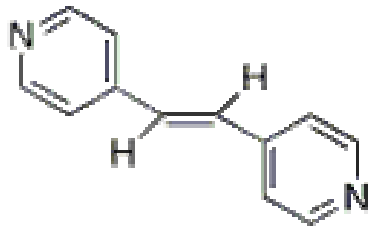

Figure 3.5: Structure of *trans*-1,2-bis(4-pyridyl)ethylene (BPE).

Figure 3.6(A) shows the SERS spectrum of 50 μM BPE on a silver coated microscope glass slide showing that the major BPE peaks at 1638 cm $^{-1}$, 1607 cm $^{-1}$, 1200 cm $^{-1}$ and 1015 cm $^{-1}$ are clearly visible. Figure 3.6(B) shows the spectrum of 50 μM BPE on a clean uncoated microscope glass slide that was dipped in the same BPE solution and dried as in the previous case. There are no BPE peaks at all. This shows it is indeed the presence of the silver island films that is responsible for the generation of the SERS signal from the BPE molecules. Figure 3.7 shows the spectrum of a silver coated slide dipped in the acetone used to make the BPE solutions. It is believed that the peaks observed in this spectrum are the due the presence of a myriad of organic impurities in acetone which were adsorbed on the surface of the silver once the slide was dipped in the acetone. As a result, the SERS spectra of the various concentrations of BPE are background subtracted to remove the contribution of the peaks from impurities in acetone.

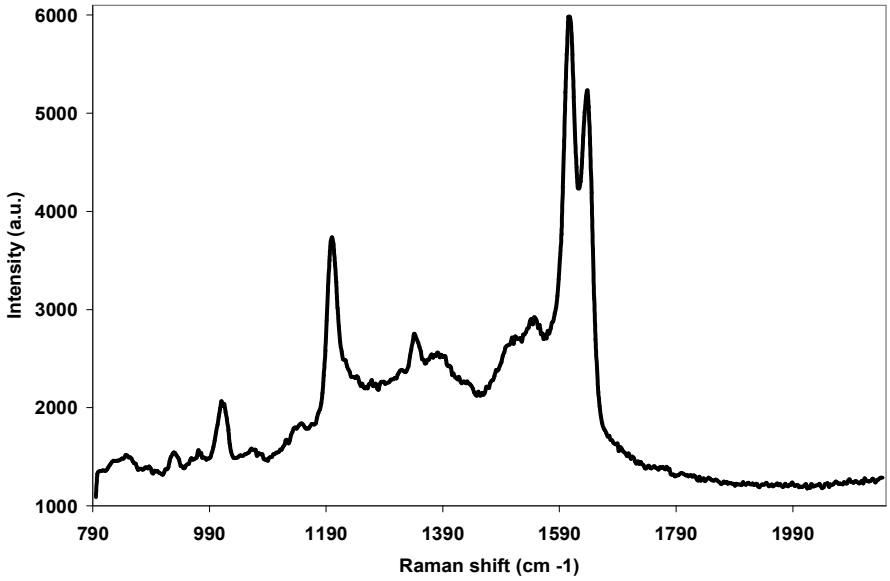

Figure 3.6(A): SERS spectrum of a silver covered microscope glass slide dip coated in 50 μM BPE solution.

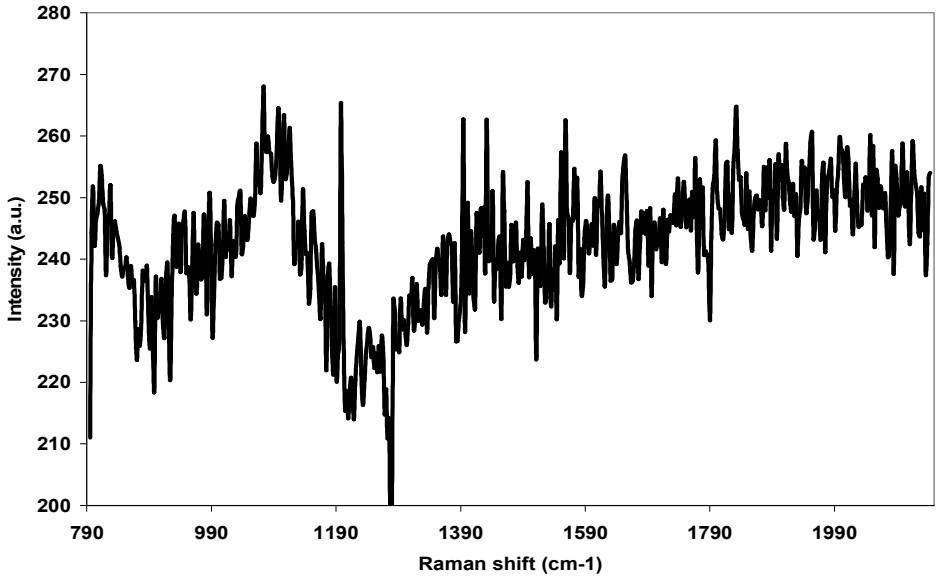

Figure 3.6(B): SERS spectrum of a clean uncoated microscope glass slide dip coated in 50 μM BPE solution. This shows the need for the presence of the silver island films to elicit a SERS response.

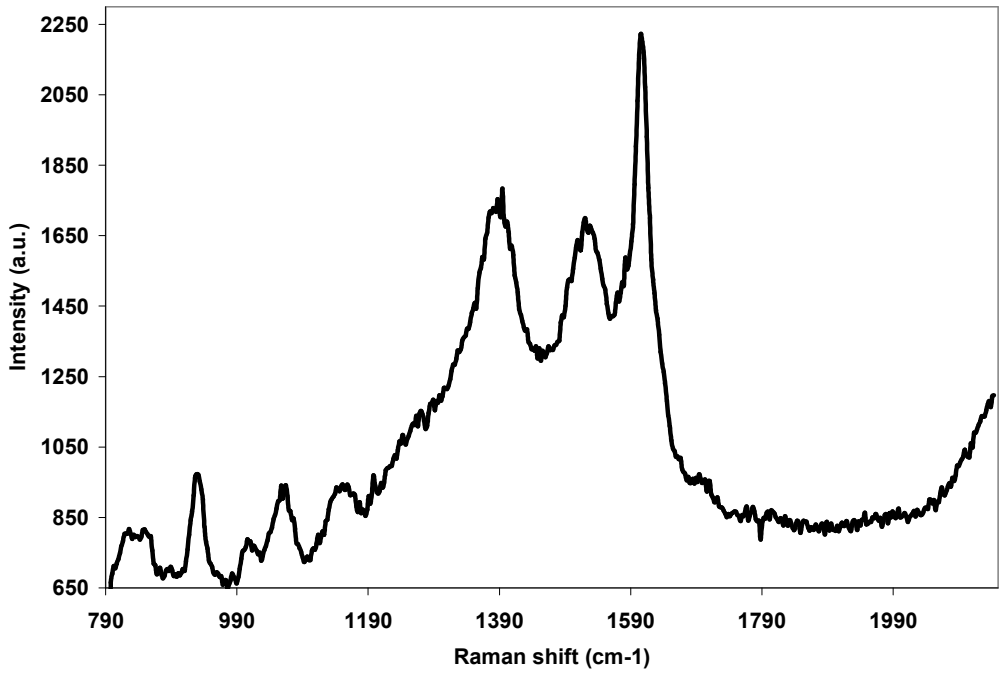

Figure 3.7: Background SERS spectrum of a silver coated slide dipped in acetone.

Shown in Figure 3.8 are the spectra of 5 μM (A), 50 μM (B) and 500 μM (C) BPE on silver coated slides showing a concentration dependent response of the SERS signal. The spectrum at each concentration level is the result of an average of 30 different spots on the slide. The figure clearly shows that the silver coated slides gives SERS signals whose intensity directly correlates to the concentration of the target analyte on its surface. The spectra were intentionally separated for purposes of clarity.

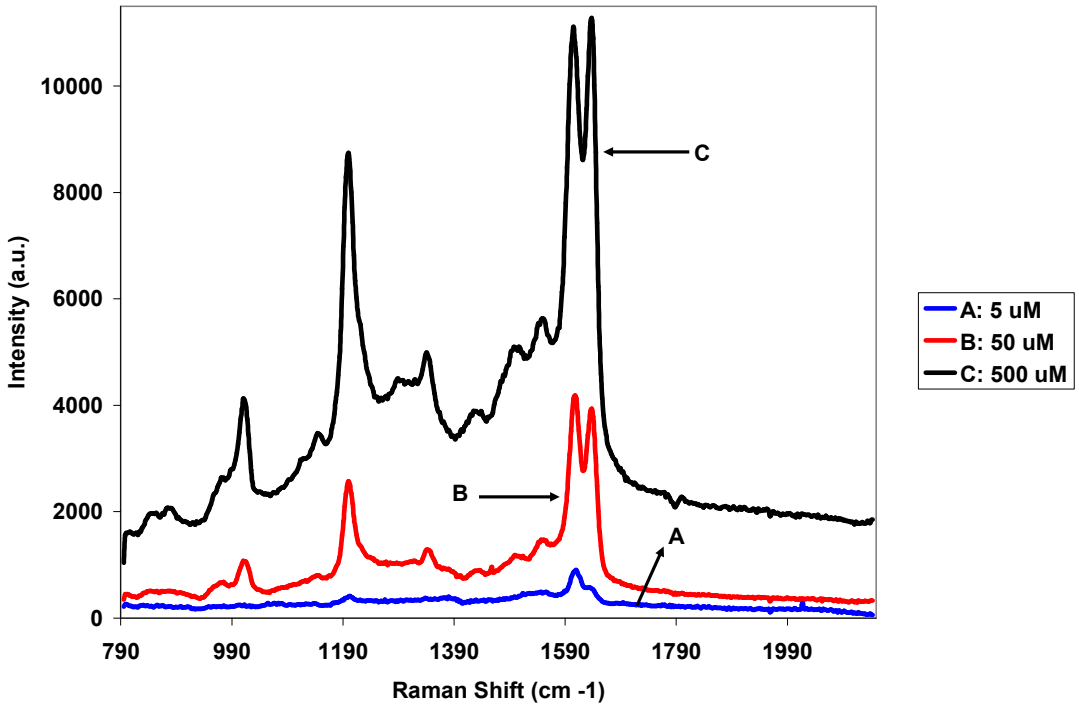

Figure 3.8: SERS spectra of 5 µM (A), 50 µM (B) and 500 µM (C) BPE on silver coated slides showing a concentration dependent response of the SERS signal. The spectrum at each concentration level is the result of an average of 30 individual spectra taken from various spots on the slide.

An inherent limitation of the SERS substrate made by the vapor deposition of silver island films on glass slides is the inability to have proper control of the morphology of the island films in terms of control of their shape, size, interparticle spacing and reduction in the formation of aggregated complexes. The rigorous control of glassware cleansing procedure, silver deposition rate and geometry can at best give only nominal control of the morphology of the silver films deposited. This leads to the generation of inconsistent SERS signals at various locations on the slide. Figure 3.9 illustrates this problem. The data presented in this figure were obtained by averaging the

SERS spectra of five individual spots approximately 5μm apart in two distinct regions of a silver coated slide dipped in 500 μM BPE solution. These two distinct regions were approximately 3 cm apart from one another. The major BPE peaks sometimes show as much as 100 % increase in intensity from one region to another. Such variability was obtained for slides dipped in all the concentrations of BPE mentioned in this study. This kind of variability is unacceptable in SERS substrates if they are to be incorporated in a biosensor as it would compromise the robustness, reproducibility, sensitivity and response time of the sensor.

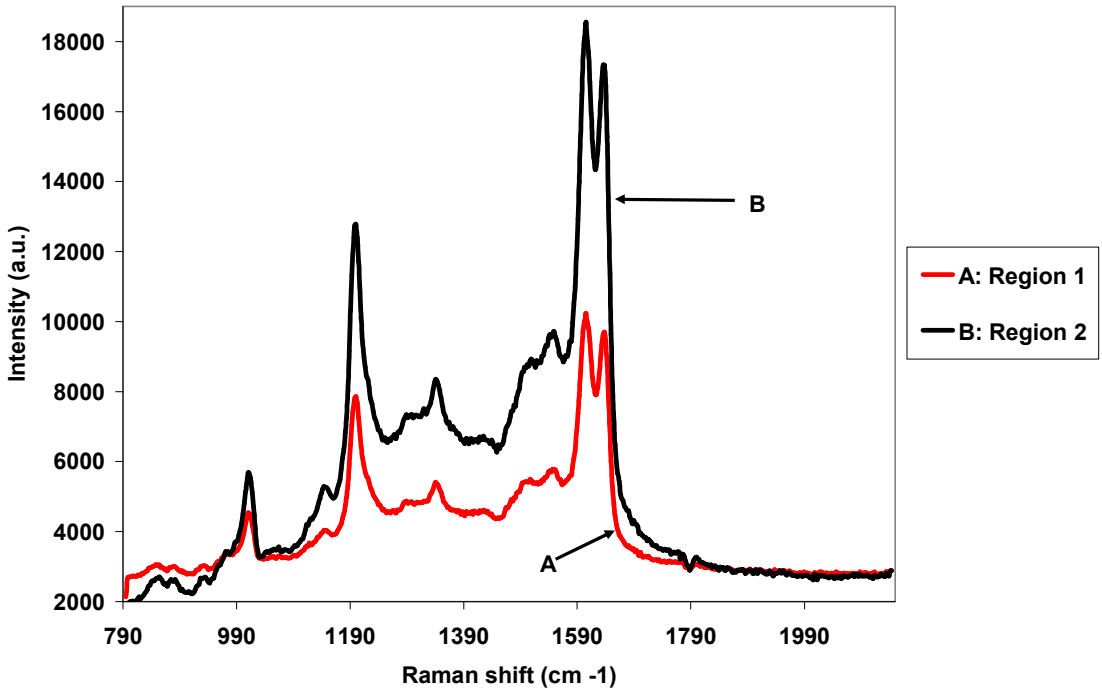

Figure 3.9: SERS spectra of 500 μM BPE on a silver coated slide showing variability in the intensity of the SERS signal at two different regions of the slide separated by 3 cm. The spectrum within each region is the result of an average of 5 individual spectra taken at spots 5 μm apart.

Use of Nanosphere Lithography (NSL) for the Fabrication of Controllable SERS Substrates

Introduction

Recent advances in nanotechnology have lead to a number of fabrication methods for creating substrate bound nanostructures with potential for use as SERS platforms. The leading nanotechnologies for sub-optical (between 10-200 nm) fabrication are electron-beam lithography (EBL) [67-70] and X-ray lithography (XRL).[71-74] In EBL, the desired pattern is serially produced by exposing a thin layer of photo-resist on a substrate to high energy electrons usually in an EBL writer connected to a Scanning Electron Microscope (SEM), followed by chemical development and thermal deposition of the noble metal. This is followed by a mask removal step that leaves the noble metal in the nanometer sized structures that were initially drawn on the substrate. [67-70] Although EBL has outstanding resolution which can yield features in the range of 1 – 2 nm in the best of cases, it is quite an expensive procedure and its serial processing format is a limitation to achieving commercial acceptable throughputs of 1 $cm^{-1}s^{-1}$.[75] XRL is similar to photolithography but uses X-rays photons instead of UV and deep UV photons to create the pattern of interest. The wavelength of interest in XRL is 0.5-1.5 nm.[71-74] This is because at these wavelengths scattering is negligible thus overcoming the severe problem of proximity effects that generally plague EBL.[71-72] Although the parallel processing capabilities of XRL permit simultaneous fabrication of large numbers of

nanostructures, XRL resolution is limited by photoelectron range and diffraction effects to 20 – 50 nm.[71-75]

An alternative approach for the large scale fabrication of surface bound nanoparticle arrays with morphological and optical properties that can be tightly controlled is Nanosphere Lithography (NSL).[75-85] NSL is generally an efficient fabrication technique to inexpensively produce nanoparticle arrays with controlled shape, size and interparticle spacing.[75-85] The NSL mask is created by the self-assembly of size-monodispersed polystyrene nanospheres of diameter *D* to form a two-dimensional colloidal crystal mask on a myriad of substrates such as fused silica, borosilicate optical glass and SF-10 glass among others. As the solvent in which the nanospheres were originally dispersed evaporates, capillary forces draw the nanospheres together and the nanospheres crystallize together to form a hexagonally close packed pattern on the substrate. In areas where the nanospheres formed a uniform monolayer, the hexagonal close packing pattern contains uniformly shaped gaps between adjacent nanospheres where a metal or any other material can be deposited via thermal evaporation, electron beam deposition, or pulsed laser deposition. In areas where the nanospheres formed a uniform bilayer the holes between adjacent nanospheres are themselves also hexagonal in shape. In higher ordered structural alignments of the nanospheres all holes are covered up. After the metal deposition step, the nanosphere mask can be removed by sonicating the substrates in methylene chloride or ethanol. This dissolves the nanospheres leaving behind just the deposited metal in the form of surface confined nanoparticles with triangular-like or hexagonal footprints (called periodic particle arrays PPL). As in all

naturally occurring crystals, nanosphere masks include a variety of defects that arise as a result of nanosphere polydispersity, site randomness, point defects, slip dislocations and grain boundaries. Typical defect free domains are in the range of 10 – 100 μm.[75-85] Schematic diagrams of single layer (SL) and double layer (DL) nanosphere masks and the corresponding periodic particles array surfaces are shown in Figure 3.10.[75]

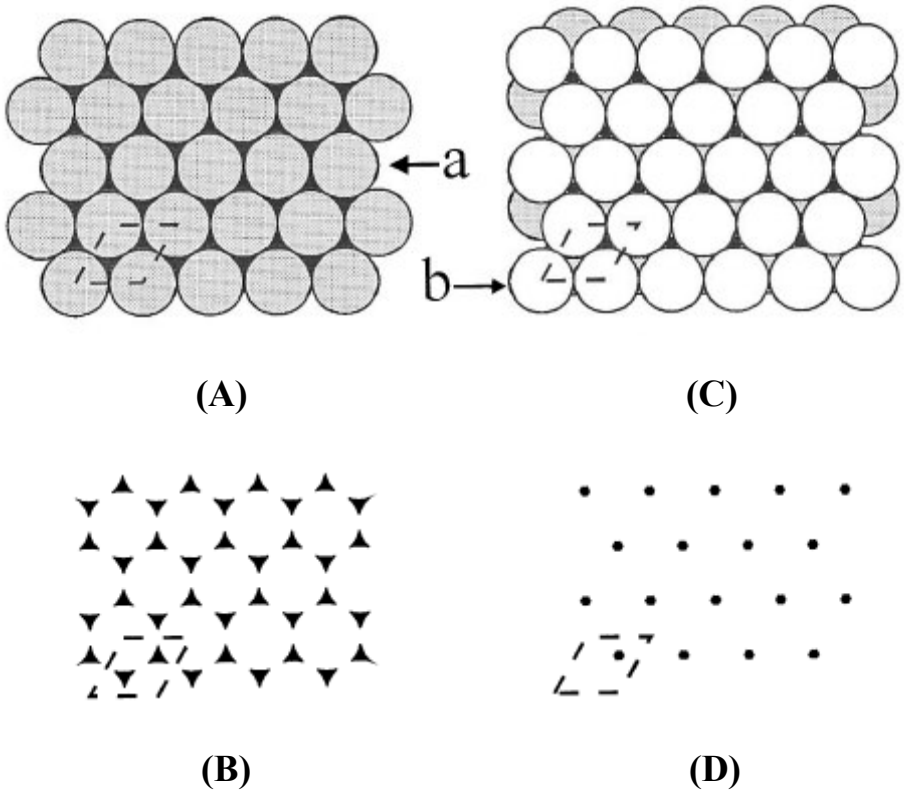

Figure 3.10: Schematic diagram of nanosphere masks and corresponding nanoparticle periodic particle arrays. (A) Single layer nanosphere mask and (B) its corresponding periodic particle array (B). (C) Double layer nanosphere mask and (D) its corresponding periodic particle array. Reprinted with permission from J.C. Hulteen and R.P. Van Duyne, "Nanosphere lithography: A materials general fabrication process for periodic particle array surfaces," *J. Vac. Sci.Technol. A* **13**(3), 1553-1558 (1995). Copyright 1995, American Institute of Physics. [75]

Figure 3.10(A) shows the single layer nanosphere mask with the triangular-like interparticle gaps where metal can be deposited. Figure 3.10(B) shows the corresponding periodic particle array shape that would emerge after metal deposition followed by mask removal. Here the "truncated tetrahedron" metal footprints arranged in a hexagonal pattern is clearly observed. Similarly Figure 3.10(C) shows the double layer nanosphere mask with the hexagonal interparticle gaps where metal can be deposited. Figure 3.10(D) shows the corresponding periodic particle array shape that would emerge after metal deposition followed by mask removal. Here the hexagonal metal footprints arranged in a hexagonal pattern is observed.

There are three crucial parameters for each of the metal nanostructures that will control its optical properties, namely its height which is controlled by the deposition depth, its in plane particle diameter $a_{SL/DL}^{geom}$ and the interparticle spacing $d_{ip,SL/DL}^{geom}$, both of which are a function of the diameter, *D*, of the nanospheres used to create the colloidal crystal mask. For the single layer case the in plane diameter a_{SL}^{geom} and the interparticle spacing $d_{ip,SL}^{geom}$ are given by the following equations:[75]

$$a_{SL}^{geom} = \frac{3}{2}\left(\sqrt{3} - 1 - \frac{1}{\sqrt{3}}\right)D = 0.233D \qquad \text{Eq. 3.1(A)}$$

$$d_{ip,SL}^{geom} = \frac{\mathrm{D}}{\sqrt{3}} = 0.577D \qquad \text{Eq. 3.1(B)}$$

For the double layer case the in plane diameter a_{DL}^{geom} and the interparticle spacing $d_{ip,DL}^{geom}$ are given by the following equations:[75]

$$a_{DL}^{geom} = \left(\sqrt{3} - 1 - \frac{1}{\sqrt{3}} \right) D = 0.155D \qquad \text{Eq. 3.2(A)}$$

$$d_{ip,DL}^{geom} = D \qquad \text{Eq. 3.2(B)}$$

For the purposes of this study the focus will primarily be on single layer structures. The aim of this study was to develop silver periodic particle arrays as described for use as substrates for SERS. Although such work is currently in its insipient stages at the Optical Biosensing Laboratory, it is believed that this technique will allow for the fabrication of SERS substrates with optical properties that can be controlled as well as modeled with relative ease. The long term goal of this project is the incorporation of these substrates in a future biosensor. The work presented here was done in collaboration with Dr. Raymond E. Schaak and his students Rob Cable and Eric Hendrickson from the Chemistry department at Texas A&M University.

Materials and Methods

Materials

600 nm carboxyl functionalized polystyrene nanospheres (5% CV) were purchased from Interfacial Dynamics Corporation (Portland, OR). All other chemicals were identical to those described in the materials section in page 24.

NSL Mask Preparation

Glass substrates were cut from microscope glass slides to a size of 1 cm^2 and were cleansed by immersion in piranha solution (3:1 concentrated H_2SO_4: 30% H_2O_2) at 80 ^oC for one hour. After cooling, the substrates were rinsed repeatedly with millipure

deionized water (18 MΩ/cm) and then sonicated for 60 minutes in 5:1:1 H_2O:NH_4OH:30%H_2O_2 solution. 5 μl of the nanosphere suspension as received (in water) was dropped onto each of the substrates where they self-assembled into a hexagonally close-packed 2D colloidal crystal mask as the water evaporated. These substrates then acted as the deposition mask.

Scanning Electron Microscopy (SEM)

SEM images of the colloidal crystal masks were taken at the Microscopy and Imaging Center at Texas A&M University using a JEOL-JSM 6400 SEM operating at 15 kV with magnification between 5,000 × and 20,000 ×.

Periodic Particle Array (PPA) Formation

After successful creation of the deposition mask, the substrates were loaded inside the chamber of an Edwards Auto 306 Vacuum Coating System in a Class 100 Clean Room Facility. The details of the deposition procedure have been discussed in the earlier section. Substrates with 20 nm, 40 nm and 80 nm silver deposition depth were sequentially made by thermal evaporation of silver. The silver deposition rate in each case was maintained at 1 nm/sec. After the silver deposition was complete, the nanosphere mask was removed by sonicating the entire substrate in methylene chloride (CH_2Cl_2) for 2 minutes. This dissolved the polystyrene nanospheres leaving behind an array of triangularly shaped silver nanoparticles in a closed hexagonal pattern on the glass substrate.

Atomic Force Microscopy (AFM) Studies

All AFM studies were done using a Digital Instruments Nanoscope IIIA (Digital Instruments) microscope in tapping mode operation. The details of the AFM imaging procedure have been discussed in the earlier section.

UV-Vis Absorption Studies

All UV-Vis absorption spectra were collected using an identical setup as described in page 25. The only difference was the spectral window of interest which was from 560 – 1020 nm.

SERS Studies

All SERS studies were carried out using a similar experimental setup as described in the previous section. The SERS spectra were collected between 1700 – 900 cm^{-1} with a 240 sec integration time and using a 785 nm SDL High Powered Diode Laser delivering approximately 1.40 mW power to the sample surface. The spectra were collected using the 50× air objective (NA = 0.75). All SERS data were processed as described previously. As in the previous section the strongly Raman scattering molecule BPE was used to characterize the SERS capability of the substrates.

Results and Discussion

Figure 3.11(A) shows an SEM image of the nanosphere colloidal crystal mask taken at a magnification of 5,000 ×. Here several lattice defects are clearly observed. There are several cases where point defects (holes due to absence of nanosphere) are seen. Along with that several slip dislocations (thin dark lines where there was slight

lattice mismatch between spheres) and grain boundaries (thick dark lines which form individual areas of nanosphere deposition) are also observed. Figure 3.11(B) shows another SEM image taken at a higher magnification of 20,000 ×. This higher magnification image clearly shows the orderly hexagonal packing of the individual nanospheres and also shows the presence of polydispersity in the size of the nanospheres. Here the dark lines represent gaps due to slip dislocations in the lattice.

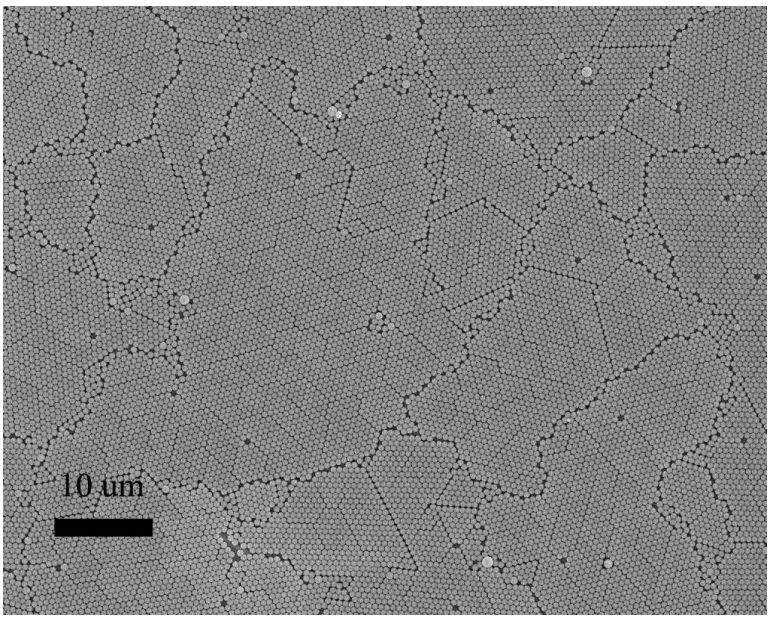

Figure 3.11(A): SEM image taken at 5,000 × magnification of the self-assembled colloidal crystal mask showing point defects, grain boundaries and slip dislocations.

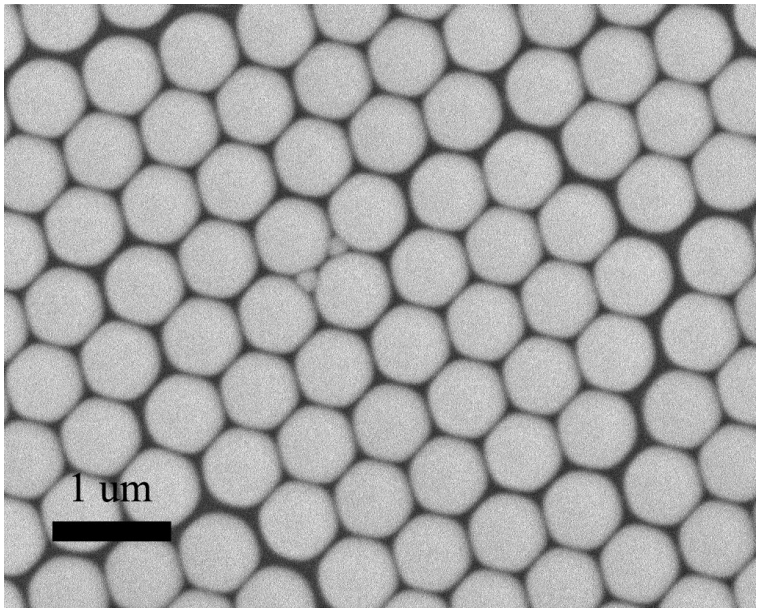

Figure 3.11(B): SEM image taken at 20,000 × magnification of the self-assembled colloidal crystal mask showing slip dislocations. The field of view is too small to observed grain boundaries. Note the close hexagonal packing of the 600 nm polystyrene beads and also polydispersity of their size.

The results of the AFM analysis performed on the substrates after silver deposition and the subsequent mask removal step are shown in Figures 3.12(A) - 3.12(D). The sample used in obtaining these set of images had 40 nm silver deposited on it. Figure 3.12(A) shows an image in the range of 30 μm × 30 μm. Here the periodic particle array of silver nanoparticles are clearly seen arranged in a hexagonally closed packed pattern on the glass substrate. The lattice defects that were observed in the previous SEM images manifest themselves here as continuous patches of silver deposited in the gaps within slip dislocations as well as large circular deposits of silver in areas where there were point defects (absence of nanosphere) in the mask lattice. Figure 3.12(B) is a blowup of Figure 3.12(A) with an image size of 10 μm × 10 μm. It

has been presented for purposes of increased clarity. Here the triangular shape of each silver nanoparticle is seen with the usual slip dislocations. Figure 3.12(C) is again a blowup of Figure 3.12(B) with an image size of 2 μm × 2 μm. This has been presented to capture the silver nanoparticles that were formed in the gaps between a group of seven adjacent nanospheres arranged in a hexagonally packed shape. Figure 3.12(D) performs a section analysis on the silver nanoparticles in Figure 3.12(C). Here the dimension of the in plane diameter of the silver nanoparticles and the vertical height of the particles are measured along the line that has been drawn through the nanoparticles. The in plane diameter a_{SL}^{geom} of the nanoparticle is measured to be approximately 244 nm and the out of plane height b is measured to be approximately 42 nm. Although the out of plane height b is in agreement with the deposition silver height of 40 nm, the in plane diameter a_{SL}^{geom} dimension from the AFM image (244 nm) is misleading as equation 3.1(A) predicts it should be approximately 140 nm (0.233D where D is 600 nm). This is the result of in plane feature size broadening which is a common problem associated with AFM studies.[79,86-89] When this occurs, the results of the AFM image reveals a consistently larger size of structures in the x and y plane (in plane parameters) due to the convolution of the real surface morphology with the AFM tip function. Several deconvolution algorithms exist in the literature (which are non trivial to implement) to recover the correct feature size from the experimental AFM images.[79, 86-89] The tip functions used for these deconvolution algorithms are derived from tip specifications obtained from the AFM tip manufacturers. No such algorithm has been developed here to extract the real feature size from this set of AFM images and hence the disconnect

exists between the theoretical and experimental in plane diameter values. This tip convolution problem however does not exist when measuring features in the z-axis (out of plane features). Figures 3.13(A) and 3.13(B) illustrates how the tip convolution problem occurs when measuring in plane features and how is does not pose a problem when measuring out of plane features.

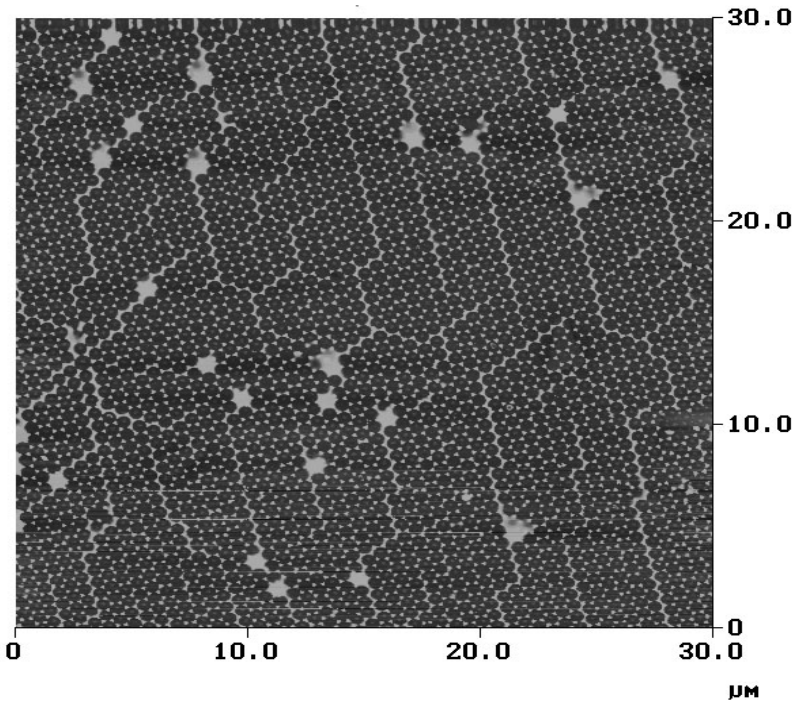

Figure 3.12(A): 30 µm × 30 µm AFM image of the surface of a substrate created by Nanosphere Lithography (NSL). Image was obtained after removal of colloidal crystal mask showing silver nanoparticles arranged in a hexagonally packed array. Lattice defects such as point defects and slip dislocations can be seen.

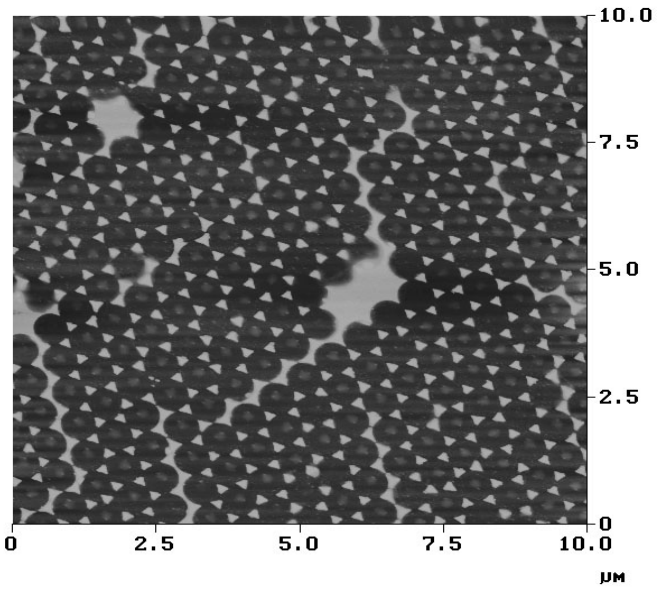

Figure 3.12(B): 5µm × 5µm AFM image of the surface of a substrate created by Nanosphere Lithography (NSL). Image was obtained after removal of colloidal crystal mask and shows silver nanoparticles arranged in a hexagonally packed array. Lattice defects such as point defects and slip dislocations can be seen.

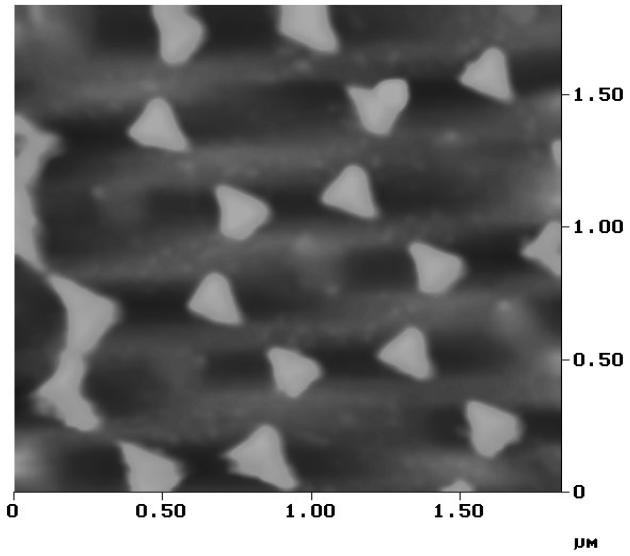

Figure 3.12(C): 2µm × 2µm AFM image of the surface of a substrate created by Nanosphere Lithography (NSL). Image was obtained after removal of colloidal crystal mask showing two groups of silver nanoparticles arranged in a hexagonally packed array. This zoomed in image is presented to show the detailed morphological structure of a group of adjacent silver periodic particle arrays.

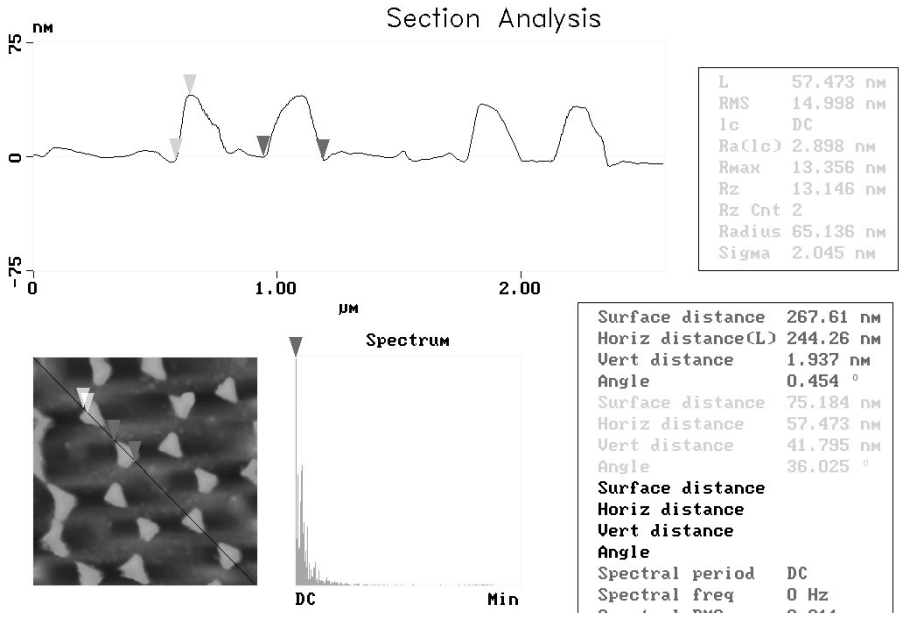

Figure 3.12(D): Section analysis performed on the silver nanoparticle arrays of Figure 3.12(C) showing the dimension of the in plane diameter and out of plane height.

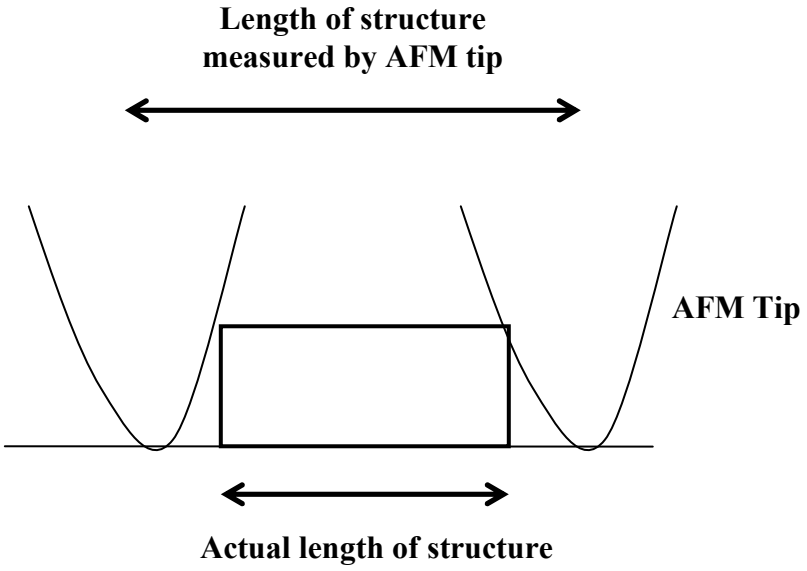

Figure 3.13(A): Schematic showing in plane line broadening of features measured in the x and y axes in an AFM image due to convolution of the AFM tip shape function with the real surface morphology.

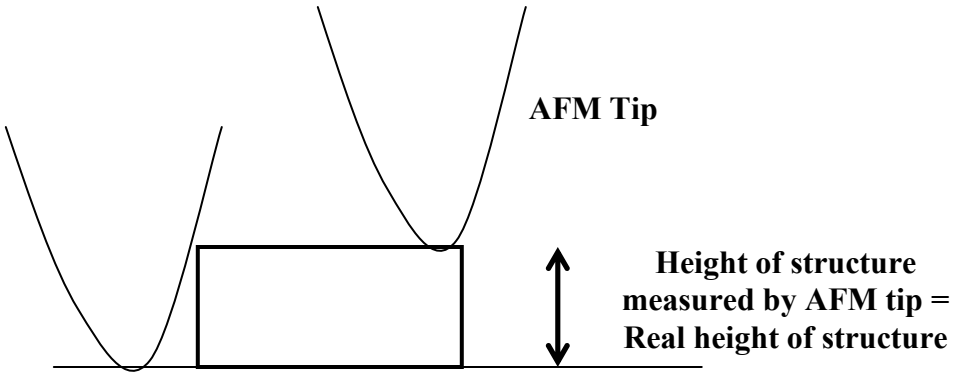

Figure 3.13(B): Schematic showing no increase in size of features measured in the z- axis in an AFM image as there is no convolution of the AFM tip shape function with the real surface morphology.

Figure 3.14(A) shows the raw extinction spectra of silver nanoparticle substrates fabricated with the Nanosphere Lithography technique. The three substrates were all made with the 600 nm diameter nanosphere mask and had an out of plane height of 20 nm, 40 nm and 80 nm respectively. The figure shows a distinctive blue shift in the location of the extinction maximum (λ_{max}) with increasing thickness of the deposited silver layer. The λ_{max} were at 850 nm, 835 nm and 710 nm for an out of plane height of 20 nm, 40 nm and 80 nm respectively. This pattern is in agreement with data obtained by other groups.[80] Each truncated tetrahedron has two parameters that are used to describe its aspect ratio: they are the in plane diameter *a* and out of plane height *b*. The in plane diameter has been described previously and the out of plane is just the thickness of the thermally deposited silver layer. Assuming the in plane diameter of the silver nanoparticles in each of the substrates remains constant (which is a function of only the diameter of the nanosphere mask) we define the aspect ratio of the individual silver

nanoparticles R as a/b. The extinction maxima data presented thus far is in agreement with the case of a theoretically determined formula for the dependence of the peak of the plasmon absorption band of gold nanorods λ_{max} as a function of their aspect ratio R and the dielectric constant of the surrounding medium ε_m which was derived by Link *et al.*:[90-91]

$$\lambda_{\max} = (33.34R - 46.31)\varepsilon_m + 472.31 \qquad \text{Eq. 3.3}$$

This formula shows that for a constant value of ε_m, the location of the extinction maxima λ_{max} increases linearly with aspect ratio R. Figure 3.14(B) shows a plot of the location of the extinction maximum with increasing out of plane height of the silver nanoparticles (for a constant in plane diameter). The data portrays the red shift of the extinction maximum wavelength with decreasing height of silver (i.e. increasing aspect ratio). A linear fit to the data is included with an R^2 value of 0.945. The slope of the linear fit approximates a 2.4 nm change in the extinction maximum for a 1 nm change in height of the silver nanoparticles.

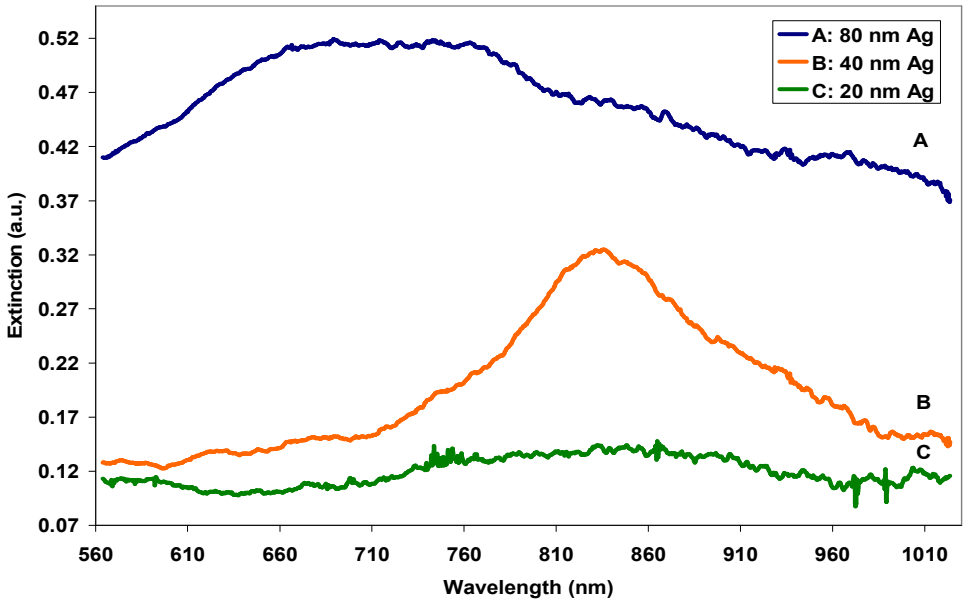

Figure 3.14(A): Extinction spectra of silver periodic particle arrays on glass substrate with (A) 80 nm, (B) 40 nm and (C) 20 nm deposition depth.

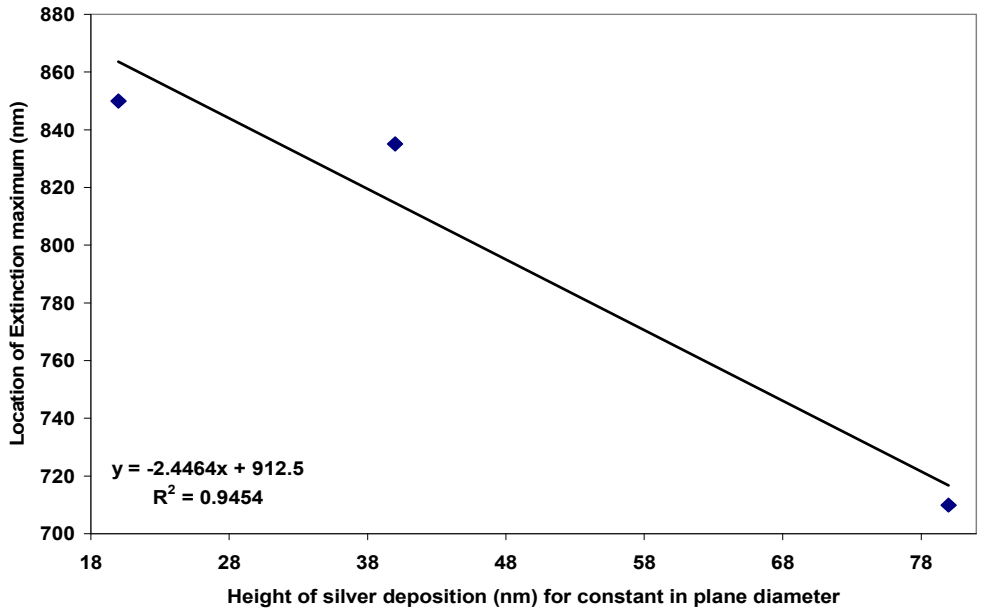

Figure 3.14(B): Plot of the location of the plasmon resonance peak of various silver periodic particle arrays with a constant in plane diameter and differing height of deposition. The decrease in height corresponds to an increase in aspect ratio of the particles.

The SERS characterization studies were done by pipetting 10 μl of 50 μM BPE solution (in acetone) on each of the substrates and allowing them to dry before locating relatively good spots on the sample via regular brightfield microscopy before striking the sample with a 785 nm laser for performing the SERS studies. SERS spectra were taken at ten different spots on each of the substrates between 1700 – 900 cm^{-1} with a 240 sec integration time. The raw spectra were then background subtracted from the background spectrum and then baseline corrected before averaging them to obtain the final SERS spectra of BPE for each substrate that is presented in Figures 3.15(A). Before presenting the SERS data it is necessary to mention a few observations on the extinction spectra of the nanoparticles that are presented in Figure 3.14(A). The quality of the SERS signal from an analyte molecule adsorbed on the surface of the silver nanoparticles is directly proportional to the extent of defect free lattice structure of the silver nanoparticle array. Defects in the nanosphere mask such as variations in packing morphology, and insufficient or overabundant quantities of nanospheres result in defects in the metal nanoparticle array structure.[77] These defects manifest themselves as perturbations in the extinction spectra as well as low magnitude of SERS signals. A lack of reproducibility of SERS signals within approximately ±20 μm of a particular spot can also allude to defects in the lattice structure. In the case of localized surface plasmon resonance (LSPR) of the silver nanoparticles manifested as a maximum in the extinction spectrum, wide bandwidths in LSPR (specially for particles within the Rayleigh size limit) can indicate the presence of heterogeneous structures within the spot size and hence can allude to the

presence of large areas of lattice defects i.e. the wider the bandwidth, the more the density and severity of the nature of defects.

Thus Figure 3.14(A) shows that the nanoparticles with an out of plane height of 80 nm has the broadest FWHM of the plasmon resonance peak. This indicates a contribution of multipole resonances in addition to the dipole resonance (as 80 nm in the axis of silver deposition is outside the Rayleigh range of nanoparticles – mutipole resonances occur at a shorter wavelengths than the dipole resonance and hence their superposition appears to broaden the dipole resonance peak), and large extent of lattice defects. In addition the broadband spectra also had very high extinction values which results from high scattering from macroscopic silver structures (it is commonly observed that large silver islands form in gaps where there were not sufficient packing of the nanospheres). The presence of the large macroscopic silver structures are shown later in this section. This along with the fact that its plasmon resonance peak at 710 nm is farthest away from the incident laser wavelength (785 nm) indicate that the SERS signal from this substrate is expected to have poor quality. The FWHM of the extinction maximum of the 40 nm height sample is narrow and together with the magnitude of the plasmon resonance peak, it indicates areas with fewest lattice defects. This along with the location of the plasmon resonance at 835 nm indicate that the 40 nm sample will give SERS signal of high quality. Although the magnitude of the extinction maximum of the 20 nm height sample was the lowest of the three samples considered, the shape of the plasmon resonance peak indicates areas of normal distribution of nanoparticles.

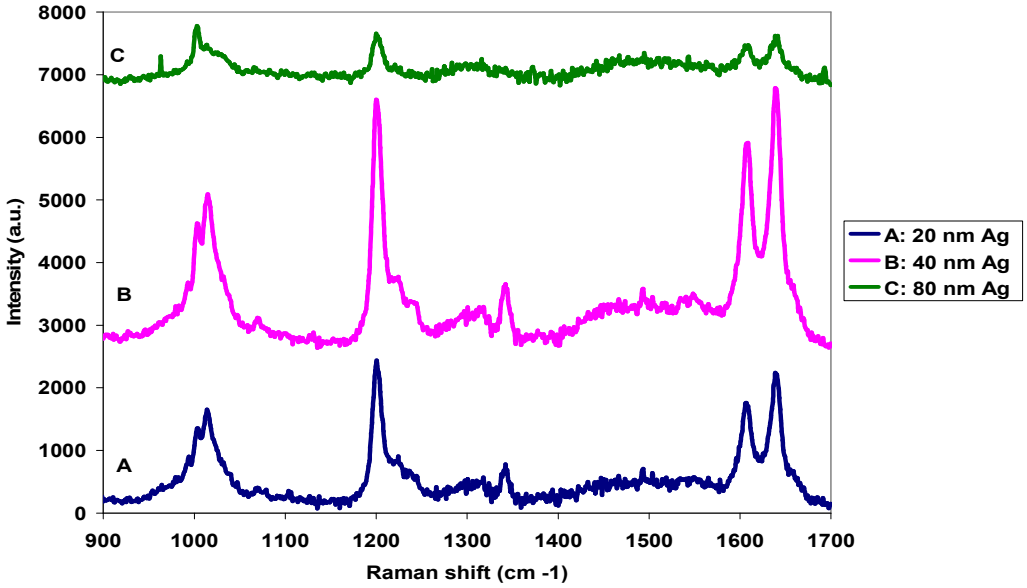

Figure 3.15(A): Average SERS spectra of 50 µM BPE collected from 10 different spots on silver periodic particle arrays. Heights of the nanoparticle are (A) 20 nm, (B) 40 nm and (C) 80 nm.

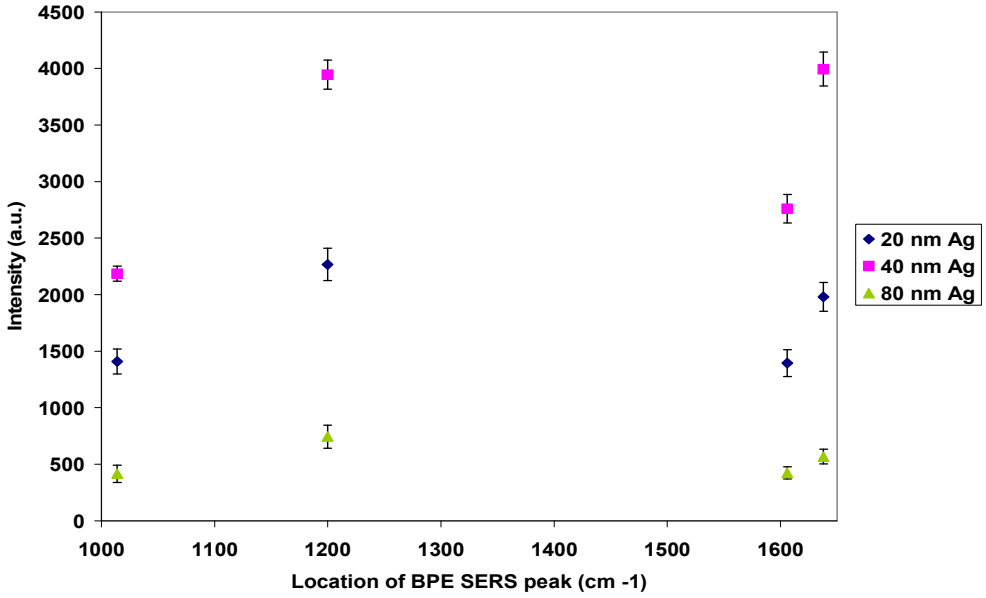

Figure 3.15(B): Plot of the magnitude of the major SERS peaks of 50 µM BPE on silver periodic particle arrays. Heights of the nanoparticles are (♦) 20 nm, (■) 40 nm and (▲) 80 nm.

The average of ten scans obtained in each of the three substrates with 50 μM BPE is presented in Figure 3.15(A). The spectra have deliberately been separated from each other for reasons of clarity of presentation. These spectra indicate that the substrate with 40 nm out of plane height of the nanoparticles provide the strongest SERS enhancement. This is followed by silver nanoparticle with a height of 20 nm and lastly 80 nm. It is expected that the substrate with plasmon resonance maximum closest to 785 nm (the incident laser wavelength used for the SERS studies) would give the strongest SERS enhancement and this is corroborated by the experimental data. Figure 3.14(B) however reveals that a substrate with a height of approximately 50-55 nm would provide optimal SERS enhancement as its plasmon resonance peak would roughly lie at 785 nm. It may be speculated that in addition to the location of the plasmon resonance peak, the presence of high areas of lattice defects in the 80 nm sample also contributed to the deterioration in the quality of SERS signal from that substrate. Figure 3.15(B) plots the average height of the major BPE SERS peaks from ten spectra obtained from each substrate. The error bars represent the standard error in the data. It is clear that the peaks at 1200 cm^{-1} and 1638 cm^{-1} are the two strongest BPE peaks obtained and the intensity of each of the peaks follow closely to both the optical properties and surface morphology of the nanoparticle substrate.

Figures 3.16(A) - 3.16(C) depict how a region in the substrate with 40 nm out of plane nanoparticle height was deemed to be a “good area” with regular arrays of hexagonally packed nanoparticles structures before it was chosen for SERS analysis. This was done through regular brightfield imaging of the substrates under white light in

the Raman microscope (upright microscope with imaging done in 180^{o} backscattering geometry). Figure 3.16(A) is an image of the substrate obtained using a 5× air immersion objective (NA = 0.12). Here we see grey areas which are areas where there is regular packing of silver periodic particle arrays (i.e. "good area"). The bright white areas are areas where there are large deposits of continuous silver. These are areas where there were no packing of the nanospheres and hence were left open to direct silver deposition. The high concentration of silver in these areas makes them highly reflective and hence they appear white in the back-reflected image. The area of the image which is circled is the area that was "zoomed" in with the 20× air immersion objective (NA = 0.40) shown in Figure 3.16(B). An interesting pattern is seen in Figure 3.16(B) which are the white lines streaking across the surface of the substrates. These are areas of lattice defects (grain boundaries) where gaps in the nanosphere mask due to lattice domain misalignment allow the deposition of large quantities of silver and hence their high reflectivity. The circled area was again "zoomed" in with the 50× air immersion objective (NA = 0.75) shown in Figure 3.16(C). This figure reveals the presence of both grain boundaries (thicker white lines) along with slip dislocations (thinner white lines) which result due to slight misalignment of adjacent nanospheres in the mask. These gaps are generally smaller in size than those in grain boundary defects and hence allow the deposition of smaller quantities of silver leading to a lower reflectivity in the back-reflected image and hence a thinner white line. In addition there are also numerous other smaller lattice defects that cannot be optically resolved and hence does not appear in these brightfield images. It is generally the presence of all these lattice defects that leads

to broadening of the extinction spectra of these substrates and which also compromises the quality and reproducibility of the SERS signal that is obtained from such substrates.

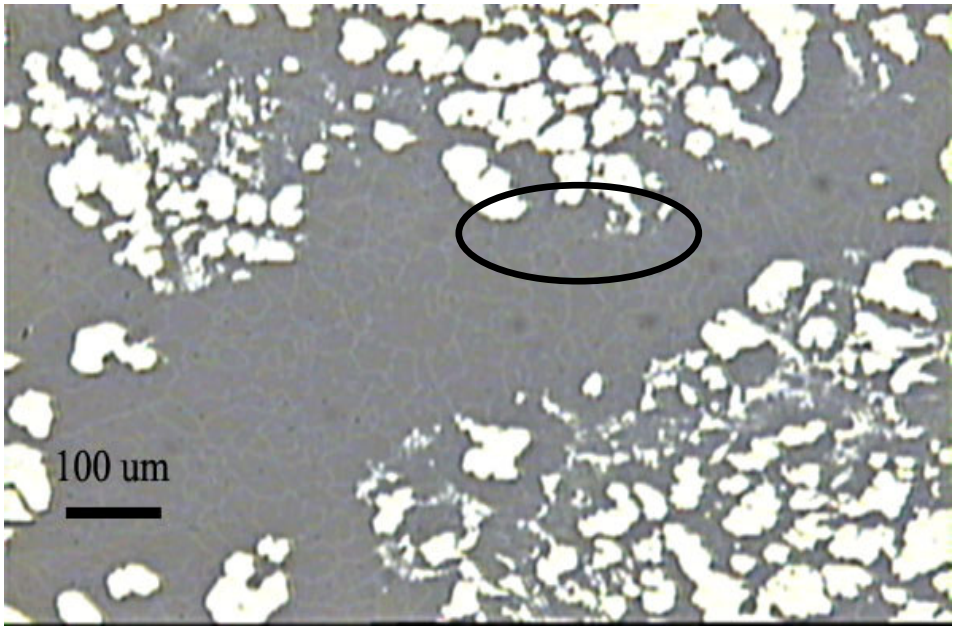

Figure 3.16(A): Brightfield image of silver periodic particle arrays obtained with 5× air objective (NA = 0.12) showing the morphology of the substrate. The grey areas are areas where there was good monolayer formation of the colloidal mask whereas the bright white areas are areas where there are large deposits of silver as no mask formation had occurred. The encircled area was zoomed in as shown in Figure 3.16(B)

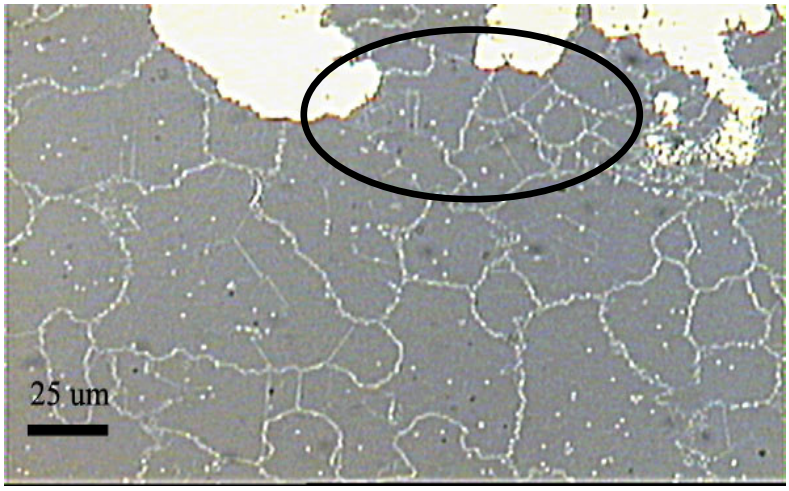

Figure 3.16(B): Zoomed in brightfield image of silver periodic particle arrays obtained with 20× air objective (NA = 0.40) showing the morphology of the substrate. The grey areas are areas where there was good monolayer formation of the colloidal mask whereas the bright white areas are areas where there are large deposits of silver as no mask formation had occurred. Here grain boundaries and point defects are visible. The encircled area was zoomed in as shown in Figure 3.16(C).

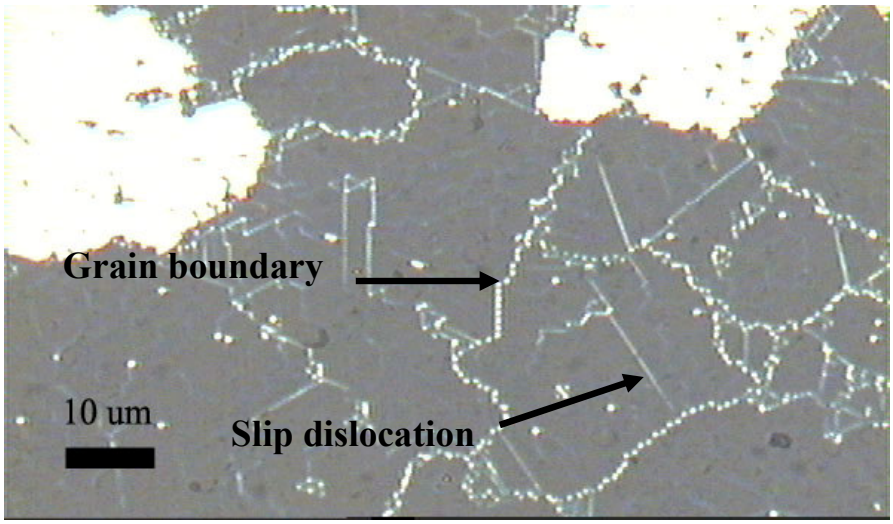

Figure 3.16(C): Zoomed in brightfield image of silver periodic particle arrays obtained with 50× air objective (NA = 0.75) showing the morphology of the substrate. Here grain boundaries point defects, and slip dislocations are clearly visible. All of the SERS studies were done focusing the incident laser beam in the "good" grey areas.

Simulation of Optical Properties of Silver Nanoparticles Using Discrete Dipole Approximation (DDA)

Introduction

Since exact solutions to Maxwell's equation only exist for particles with spherical shape, the need to calculate the scattering and absorption properties for any other arbitrary geometries requires approximate methods to solve Maxwell's equation. The Discrete Dipole Approximation (DDA) is one such method. It is a flexible and powerful technique for computing the extinction, scattering and absorption by targets of arbitrary geometry.[92-93] Recent advances in the development of efficient algorithms and computing power has made the DDA an attractive choice for solving many light extinction problems. The technique was first introduced in the field of astrophysics by Purcell and Pennypacker [94] and has since undergone a number of theoretical developments.

Fundamentally the DDA algorithm works by replacing the solid particle (target) of interest of volume V by an array of N point dipoles of polarizability α_i located at positions $\mathbf{r}_i$. The lattice spacing d of a target of volume V described by N dipoles is represented as:[93]

$$d = (V / N)^{1/3} \qquad \text{Eq. 3.4}$$

Each dipole has an oscillating polarization in response to both the incident wave $\mathbf{E}_{\mathrm{loc},i}$ and the electric field due to all of the other *N-1* dipoles in the array. The solution to the

dipole polarizations can be obtained as the solution to a set of *N* coupled complex vector equations of the form:[95]

$$\mathbf{P}_i = \alpha_i \left(\mathbf{E}_{\mathrm{loc},i} - \sum_{j \neq i} \mathbf{A}_{ij} \mathbf{P}_j \right) \qquad \text{Eq. 3.5}$$

where $\mathbf{E}_{\mathrm{loc},i}$ is the electric field at position $\mathbf{r}_i$ due to the incident plane wave with amplitude $\mathbf{E}_0$ and wave vector $\mathbf{k}$ and is represented as: [95]

$$\mathbf{E}_{\mathrm{loc},i} = \mathbf{E}_0 \exp[i(\mathbf{k} \cdot \mathbf{r}_i - \omega t)] \qquad \text{Eq. 3.6}$$

and the polarizability α is related to the dielectric constant of the target (ε_i) and that of the embedding medium (ε_0) through a factor $\varepsilon_r = (\varepsilon_i/\varepsilon_0)$ according to the following expression:[93]

$$\alpha = \left(\frac{3d^3}{4\pi} \right) \left(\frac{\varepsilon_r - 1}{\varepsilon_r + 2} \right) \qquad \text{Eq. 3.7}$$

In Eq. 3C.2, the term $-\mathbf{A}_{ij}\mathbf{P}_j$ represents the contribution to the electric field at position $\mathbf{r}_i$ that is due to the dipole $\mathbf{P}_j$ at location $\mathbf{r}_j$ which also includes retardation effects. Each element $\mathbf{A}_{ij}$ is a 3×3 matrix defined by: [95]

$$\mathbf{A}_{ij}\mathbf{P}_j = \frac{\exp(ikr_{ij})}{r_{ij}^3} \left\{ k^2 \mathbf{r}_{ij} \times (\mathbf{r}_{ij} \times \mathbf{P}_j) + \frac{(1 - ikr_{ij})}{r_{ij}^2} \left[r_{ij}^2 \mathbf{P}_j - 3\mathbf{r}_{ij} (\mathbf{r}_{ij} \cdot \mathbf{P}_j) \right] \right\} \qquad \text{Eq. 3.8}$$

where $\mathbf{r}_{ij} = \mathbf{r}_i - \mathbf{r}_j$ and $k = \| \mathbf{k} \|$. Defining $A_{ii} = \alpha_i^{-1}$ helps to reduce the extinction problem to finding the polarizations $\mathbf{P}_j$ that satisfy a system of *N* inhomogeneous linear complex vector equations:[95]

$$\sum_{j=1}^{N} \mathbf{A}_{ij} \mathbf{P}_j = \mathbf{E}_{\mathrm{loc},i} \qquad \text{Eq. 3.9}$$

Once the above equation is solved for the unknown polarizations $\mathbf{P}_j$, the extinction C_{ext} , absorption C_{abs}, and scattering cross sections C_{sca} is evaluated from the optical theorem[96] to give:[92, 95, 96, 97]

$$C_{ext} = \frac{4\pi k}{|\mathbf{E}_0|^2} \sum_{i=1}^{N} \text{Im}\left(\mathbf{E}^*_{\text{loc},i} \cdot \mathbf{P}_i\right) \qquad \text{Eq. 3.10(A)}$$

$$C_{abs} = \frac{4\pi k}{|\mathbf{E}_0|^2} \sum_{i=1}^{N} \left\{ \text{Im}\left[\mathbf{P}_i \cdot \left(\alpha_i^{-1}\right)^* \mathbf{P}_i^*\right] - \frac{2}{3} k^3 |\mathbf{P}_i|^2 \right\} \qquad \text{Eq. 3.10 (B)}$$

The scattering cross section C_{sca} = C_{ext} - C_{abs} can be directly evaluated once the polarizations $\mathbf{P}_i$ are computed.

Materials and Methods

Colloidal gold (Au) nanoparticles particles with a mean diameter of 15.5 nm and a coefficient of variation of 10% were purchased from Ted Pella, Incorporated (Redding, California). The complex mathematical operations described above were performed using the publicly available DDSCAT.6.0 program written by Draine and Flatau [98-99] which uses the fast Fourier transform (FFT) and complex-conjugate gradient (CCG) methods to solve the DDA algorithm described above. The DDSCAT program allows the flexibility of user defined targets which were exploited to compute the extinction cross sections of silver nanoparticles with a "truncated" tetrahedron shape that is formed by the use of Nanosphere Lithography (NSL). These cross section calculations are computationally intensive and require considerable amount of computing power and time. As a result they were performed on the COSMOS supercomputer at Texas A&M

University. COSMOS is an SGI Altix 3700 supercomputer, which consists of 128 Itanium-2® processors, and 256 gigabytes of main memory (DDR SDRAM). It is based on a Distributed Shared Memory (DSM) architecture, where memory is physically distributed among 32 Computation-bricks (``C-bricks''). Each C-brick consists of two pairs of 1.3GHz Itanium-2 64-bit μ-processors, locally attached memory, cache-coherence logic and interconnection fabric. The operating system of COSMOS is the IA-64 version of Linux with several SMP and NUMA-aware enhancements provided by SGI and the OSS community.

There are two criteria for the validation (convergence) of the DDA as implemented by DDSCAT.6.0. The first one is that for each point in the calculation, $|m|kd < 1$ where m is the complex wavelength dependent refractive index of the target, d is the lattice spacing between dipoles used to describe the target and is a parameter governed by the number of dipoles N used in the calculation and k is $2\pi/\lambda$. This means that the lattice spacing d needs to be small compared to the wavelength of a plane wave in the target material so that "phase" of the incident wave varies less than ~ 1 radian between dipoles. The second criterion (related to the first) emphasizes that the lattice spacing d must be small enough (N must be large enough) to describe the target shape satisfactorily.[92, 93, 99] Another parameter used by the program to characterize the target is its "effective radius" which is represented by a_{eff} and defined as the radius of a sphere of equal volume V to the target being described in the particular application. It is represented as:[99]

$$a_{\text{eff}} \equiv (3V / 4\pi)^{1/3} \qquad \text{Eq. 3.11}$$

Results and Discussion

The ability of the DDSCAT program to accurately predict the extinction spectrum of nanoparticles was first tested by simulating the extinction spectrum of 15.5 nm diameter spherical gold nanoparticles and comparing it with the experimental extinction spectrum obtained from commercially purchased 15.5 nm colloidal gold nanoparticles. The simulated and experimental spectrum are presented in Figures 3.17(A) and 3.17(B) respectively. The simulation was performed using 7500 dipoles and 20 discrete points between 400 and 800 nm. It should be noted that DDSCAT.6.0. outputs the result as the extinction efficiency factor $Q_{ext} = C_{ext}/\pi\, a_{eff}^2$, where C_{ext} is the extinction cross section and $\pi\, a_{eff}^2$ is the physical cross sectional area of the target. This helps to normalize the output data between particles of various shapes and sizes.[99] Here $|m|kd < 1$ for each point in the simulation was well below 0.2.

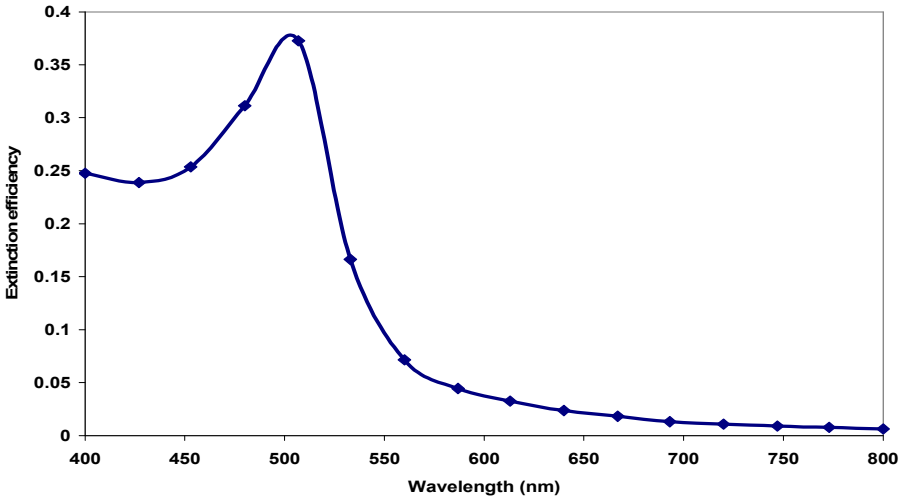

Figure 3.17(A): DDSCAT simulation of the extinction spectrum of 15.5 nm diameter spherical gold nanoparticles using 7,500 dipoles at 20 discrete points between 400 and 800 nm. Note the location of the plasmon resonance peak (λ_{max}) at approximately 510 nm.

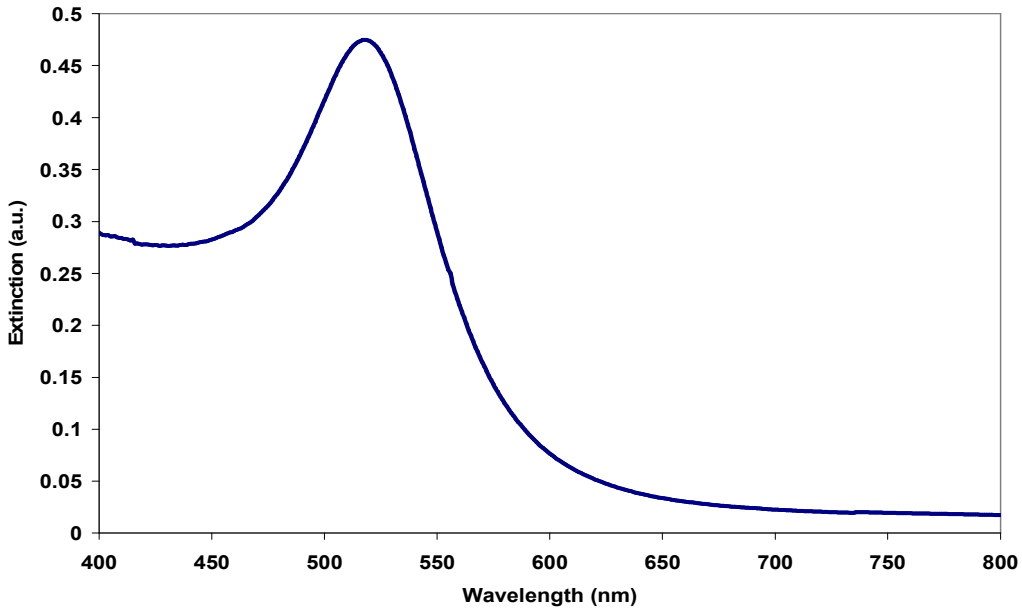

Figure 3.17(B): Experimental extinction spectrum of 15.5 nm diameter spherical gold nanoparticles between 400 and 800 nm. Note the location of the plasmon resonance peak (λ_{max}) at approximately 520 nm.

The results shown in Figures 3.17(A) and 3.17(B) show good agreement between simulated and experimental data. The slight differences in plasmon resonance peaks between the simulated data (λ_{max} at approximately 510 nm) and experimental data (λ_{max} at approximately 520 nm) can arise due to errors in the dielectric functions of gold that was used in the simulation. These values were obtained from Palik [100] and are only approximations obtained from experimental analysis of bulk gold. The experimental data also had a wider bandwidth than that of the simulated data. This can be the result of two factors: (i) inhomogeneity in particle sizes in case of the experimental data as it is extremely difficult to create uniform sized colloidal particles through chemical reduction. In case of the simulation, only one particle size was used; (ii) the gold nanoparticles studied were 15.5 nm in diameter which is well below the mean free path of a

conduction band electrons in gold (≈ 42 nm at room temperature).[101] In this size regime the conduction electrons interact significantly with the nanoparticle surface which changes its bulk collision frequency and thus also alters the dielectric constant of the metal. This phenomenon results in broadening of the plasmon resonance bandwidth.[101] The DDSCAT program uses values of refractive index of gold from Palik [100] (input by the user and in turn converted by DDSCAT to dielectric constant) which are obtained experimentally from bulk metal that does not take into consideration the electron surface scattering phenomena.[92-95]

The next set of simulations presented in this study are that of silver nanoparticles in a "truncated" tetrahedron shape fabricated using the technique of Nanosphere Lithography (NSL) with masks made of 600 nm diameter beads. The different sizes of these substrates were made with various heights of silver deposited. They were 20 nm, 40 nm and 80 nm respectively. The in plane diameter of each of these tetrahedrons were kept constant at 250 nm according to the results of the section analysis studies of Figure 3.12(D). The silver nanoparticles thus had a volume of 7.3×10^{-4} μm^3 (a_{eff} = 0.056 μm), 1.1×10^{-3} μm^3 (a_{eff} = 0.065 μm) and 2.0×10^{-3} μm^3 (a_{eff} = 0.078 μm) respectively. These nanoparticles were modeled with approximately 7500 dipoles with extinction spectra computed at 16 discrete wavelengths between 500 nm to 1100 nm. Each of the computation required approximately 30 hours of CPU time and 22224 kb of physical memory. The limited amount of CPU time allocated to each individual account by the Supercomputing Center at Texas A&M University restricted the number of dipoles that could be used to describe the target. The value of $|m|kd$ for all the different sized targets

used at each specific wavelength was well below 0.5 and thus the convergence of the DDA algorithm can be expected.

Figure 3.18(A) shows the results of the DDSCAT simulation of the three silver nanoparticles with constant in plane diameter of 250 nm and out of plane heights of (A) 80 nm, (B) 40 nm and (C) 20 nm. These simulation show the location of the extinction maximum to red shift from 820 nm for spectrum A (80 nm Ag) to 860 nm for spectrum B (40 nm Ag) and finally to 960 nm for spectrum C (20 nm Ag).

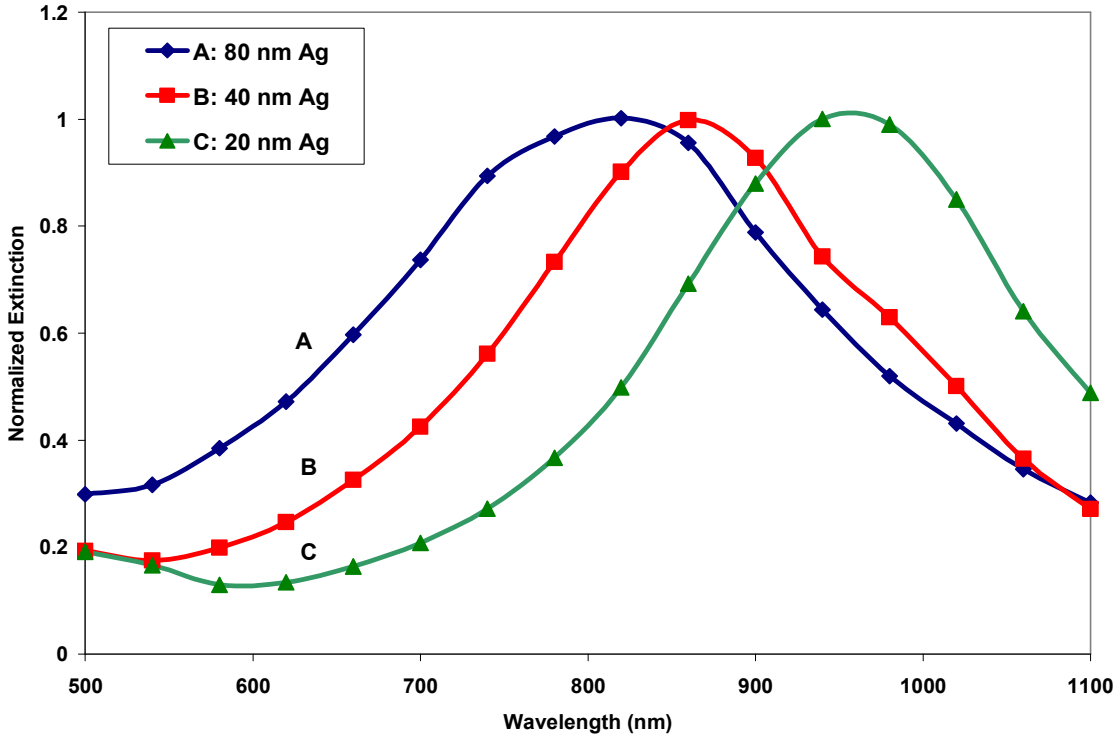

Figure 3.18(A): DDSCAT simulation of the normalized extinction efficiency spectra of silver periodic particle arrays on a glass substrate with various deposition depths. They are (♦) 80 nm, (■) 40 nm and (▲) 20 nm deposition depth. Each simulation was done with approximately 7,500 dipoles and 16 discrete points between 500 nm to 1100 nm.

The plot of the change in location of extinction maximum with increase in height of silver deposited (decreasing aspect ratio) is shown in Figure 3.18(B). This monotonic increase in the wavelength of the extinction maximum with increase in aspect ratio of the nanoparticles is in agreement with similar work done by Link *et al.* [90-91] on gold nanorods and is in qualitative agreement with the experimental variations in extinction maximum locations as observed in Figure 3.14(B). The careful examination of Figure 3.18(A) reveals that the plasmon resonance bandwidth increases with increasing depth of silver deposition. This can be explained as a result of higher order multipole resonances occurring for the larger particle sizes as the dimension of the particle in the axis of silver deposition crosses the Rayleigh limit (≈ 30-40 nm). These multiple resonances occur at shorter wavelengths to the dipole resonance and increases in magnitude with particle size. Hence the superposition of the higher order multiple resonances with the dipole resonance results in an overall broadening of the bandwidth of the extinction peak. This can be seen in the appearance of a shoulder at 740 nm for the 80 nm silver sample. A more detailed explanation of dipole and multipole resonances is provided in the following section of this dissertation.

The three data points in Figure 3.18(B) gives a linear fit according to the equation provided in the inset. The linear fit implies that a change of 1 nm in particle height leads to approximately a 2.1 nm change in location of the plasmon resonance peak. The low R^2 value of the linear fit occurs because while there is a 40 nm shift of the extinction maximum location between the 80 nm and 40 nm of out of plane height silver nanoparticles, the change in extinction maximum location between the 40 nm and 20 nm

out of plane height silver nanoparticles is 100 nm. This discrepancy might be due to size of the lattice spacing *d* used to describe the target. Since the number of dipoles for each simulation was held constant at 7,500, *d* had a progressively larger value from the 20 nm to the 80 nm sample respectively. This discrepancy might be accounted for by varying the number of dipoles (*N*) used to define each target so that the value of *d* for each target remains the same. This variation in dipole number must be done within the restrictions of CPU time that is allocated for each individual account by the Supercomputing Center at Texas A&M University.

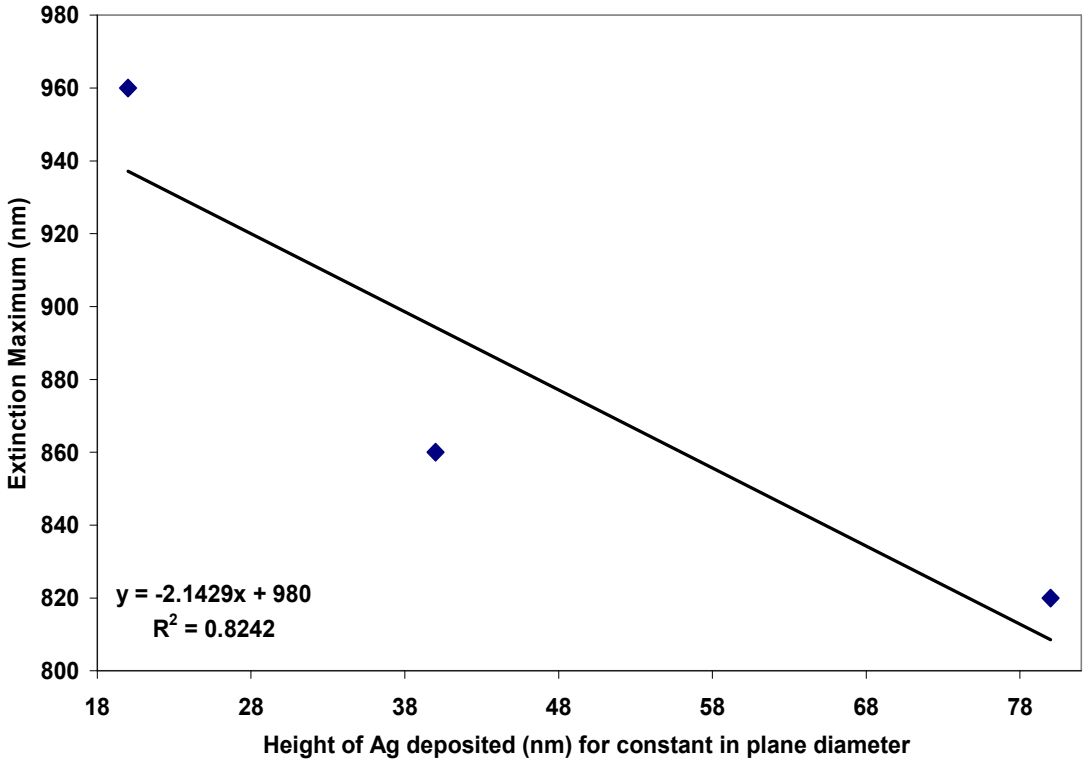

Figure 3.18(B): Plot of the location of the plasmon resonance peak of silver periodic particle arrays as a function of height with constant in plane diameter simulated using DDSCAT.

A comparison of Figures 3.18(A) and 3.18(B) with Figures 3.14(A) and 3.14(B) shows that the location of the extinction maximum for the simulations are always at a longer wavelength when compared to the experimental data for all the sizes of nanoparticles considered. There is however a qualitative agreement between the two cases which both show a monotonic red shifting of the extinction maximum with increased aspect ratio of the nanoparticles. This observation is also in agreement with previous work of Schatz and Van Duyne.[78, 102] This discrepancy between experimental and simulated data can occur for a number of reasons: (i) The simulations only take into consideration one nanoparticle whereas in the experimental case, there is the interaction of hundreds of thousands of nanoparticles within the beam spot size; (ii) The experimental case also involves the presence of lattice defects which influence its optical properties which is not accounted for in the simulation; (iii) The presence of an oxide layer coating on the silver nanoparticles in the experimental case (not accounted for in the simulation) which is inevitably produced during fabrication of the nanoparticle. This oxide layer can alter the optical properties of the silver nanoparticle; (iv) The simulations also do not take into account the presence of the glass substrate that the silver nanoparticles are attached to; (v) There might also be other chemical interactions between the highly reactive silver and its surroundings that are not accounted for in the simple dielectric environment model used in the simulations;

Gold Nanoshell Theory and Substrate Characterization

Introduction

Metal nanoparticles display a wide range of interesting and useful optical properties which makes them a primary focus of current research. Fundamentally, metal nanoparticles bridge the gap between the bulk and the atomic level, and thus exhibit properties that are unique to this particular size regime. Recent advances in nanotechnology has allowed the precise fabrication of a wide range of metal nanostructures with well characterized optical properties that have been functionalized for incorporation into devices.[85,103-104] These advances in fabrication techniques have also helped reduce nanoparticle size distribution, thus improving the morphological and optical properties of the nanoparticles by reducing the inhomogeneity problem.

The most ubiquitous of these exploited optical properties of metal nanoparticles is the optical plasmon resonance which is associated with the collective oscillation of conduction band electrons that are confined in nanoparticles. The resonance in nanoscale metallic structures is determined by the size, shape and dielectric properties of the nanoparticle as well as its local chemical environment thus making it an attractive phenomenon to exploit in the design of optically based biological or chemical sensors.[101,105-107] The plasmon resonance phenomenon is also responsible for large local field enhancements at the surface of the metal nanoparticles which can also be exploited in surface enhanced Raman scattering (SERS) based applications.[108] A qualitative explanation of plasmon resonance can be presented in the simplest case of a spherical

metal nanoparticle as depicted in Figure 3.19.[109] When a small spherical metallic nanoparticle is irradiated by light, the oscillating electric field causes the conduction electrons to oscillate coherently. When the electron cloud is displaced relative to the nuclei, a restoring force arises from Coulombic attraction between electrons and nuclei that results in oscillation of the electron cloud relative to the nucleus.[109] This oscillation frequency is governed by four parameters namely, the density of electrons, the effective electron mass, and the shape and size of the charge distribution. The collective oscillation of the electrons is called the dipole plasmon resonance of the particle. For larger particles, higher modes of plasmon excitation can occur, such as the quadrupole mode where half of the electron cloud moves parallel to the applied field and half moves antiparallel.[101, 109] For noble metals like silver and gold which have completely filled d-orbitals and half filled s-orbitals, the plasmon frequency is also influenced by the electrons in the d-orbitals. The plasmon frequency can be related to the metal dielectric constant, which is a property that can be measured as a function of wavelength for bulk metal.[101, 109]

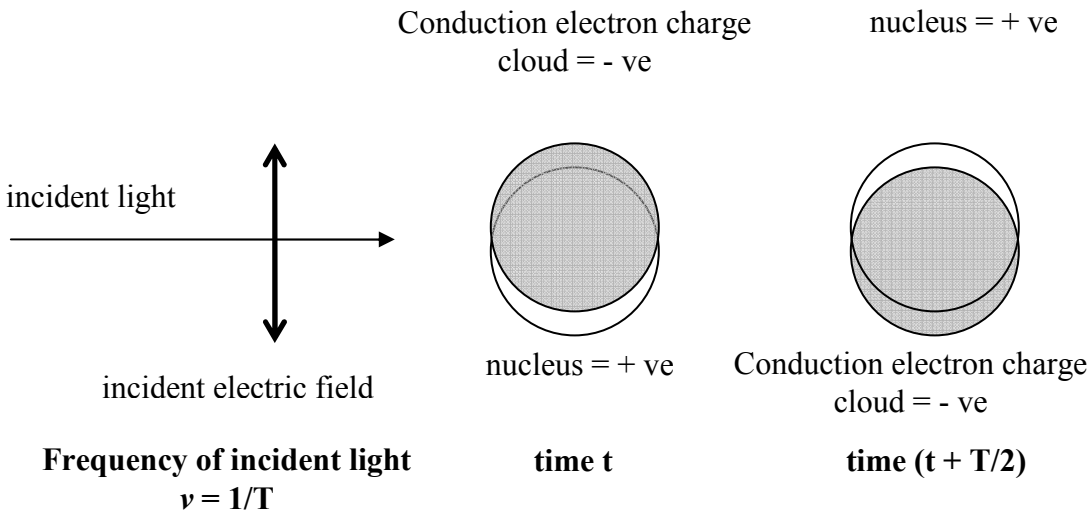

Figure 3.19: Plasmon oscillations in spherical metal nanoparticles showing the displacement of the conduction electron charge cloud relative to the nuclei. Diagram adapted from Kreibig Vollmer.[101]

As mentioned earlier, a convenient way to study the optical properties of metal nanoparticles is via metal nanospheres. In this regard Mie theory is of paramount importance.[54] This is because Mie presented an exact solution to Maxwell's equations that describes the extinction spectra (extinction = absorption + scattering) of spherical particles of arbitrary size.[54,96,110] This was of importance because most of the early standard metal colloidal preparation techniques that were used to fabricate metal nanoparticles resulted in approximately spherical structures whose optical properties were investigated and characterized by probing a large ensemble of these particles. Hence Mie theory allowed for the design and execution of insightful theory-experiment studies.

Following the famous notation of Bohren and Huffman, [96] the extinction, scattering and absorption cross sections of metal nanoparticles when excited by

electromagnetic radiation can be calculated from Mie theory by series expansions of the involved fields into partial waves of different spherical symmetries:[96,101]

$$\sigma_{ext} = \frac{2\pi}{|\boldsymbol{k}|^2} \sum_{L=1}^{\infty} (2L+1)\,\mathrm{Re}\{a_L + b_L\} \qquad \text{Eq. 3.12(A)}$$

$$\sigma_{sca} = \frac{2\pi}{|\mathrm{k}|^2} \sum_{L=1}^{\infty} (2L+1)\left(|a_L|^2 + |b_L|^2\right) \qquad \text{Eq. 3.12(B)}$$

$$\sigma_{abs} = \sigma_{ext} - \sigma_{sca} \qquad \text{Eq. 3.12(C)}$$

with a_L and b_L are the "Mie coefficients" following from the appropriate boundary conditions and can be described as: [96,101]

$$a_L = \frac{m\psi_L(mx)\psi_L'(x) - \psi_L'(mx)\psi_L(x)}{m\psi_L(mx)\eta_L'(x) - \psi_L'(mx)\eta_L(x)} \qquad \text{Eq. 3.13(A)}$$

$$b_L = \frac{\psi_L(mx)\psi_L'(x) - m\psi_L'(mx)\psi_L(x)}{\psi_L(mx)\eta_L'(x) - m\psi_L'(mx)\eta_L(x)} \qquad \text{Eq. 3.13(B)}$$

where $m = n/n_m$, where n denotes the complex index of refraction of the particle and n_m the real index of refraction of the surrounding medium. $\boldsymbol{k}$ is the wavevector and $x = |\boldsymbol{k}|R$ the size parameter. $\psi_L(x)$ and $\eta_L(x)$ are Riccati-Bessel cylindrical functions. The prime indicates differentiation with respect to the argument in parentheses. The summation index L gives the order of the partial wave, as described by the vector spherical harmonic functions for the electric and magnetic fields and so represents the order of the multipole excitations in the nanoparticle. Hence L = 1 corresponds to the dipole field, L =2 corresponds to the quadrupole field, L = 3 the octupole fields and so on.[96,101] The scattering cross section of a particle is defined by relating the rate of

photons striking a molecule to the rate of scattering in all directions shown by the equation:[1]

$$P_{sc} = \sigma_{sc} E_{in} \qquad \text{Eq. 3.14(A)}$$

where P_{sc} is the rate of scattering form a molecule in all directions (in W), and E_{in} is the irradiance of incident light (W cm^{-2}). The units of the scattering cross section, σ_{sc} are in cm^2. The rate of scattering in all directions (P_{sc}) can be calculated from the scatter intensity (I_{sc}): [1]

$$P_{sc} = 2\pi \int_0^{\pi} I_{sc}(\theta) \cos(\theta) d\theta \qquad \text{Eq. 3.14(B)}$$

The scattering cross section can thus be viewed as an area presented by a molecule for the scattering of incident photons.[1] The absorption and extinction cross section are likewise defined as an area presented by a molecule for the absorption of incident photons and an area presented by a molecule for absorption and scattering of incident photons respectively.

A simple way to explain the optical properties of metal nanoparticles is to consider the interaction of light with a spherical particle that is much smaller than the wavelength of light. Under such circumstances, the electric field of the light is assumed to be spatially constant (but still time dependent), and hence the interaction is governed by electrostatics rather than electrodynamics. This is often called the quasistatic approximation and the solution to the quasistatic approximation of Mie theory employs only the dipole term (L = 1) and the wavelength-dependent dielectric constant of the metal particle, ε_i , and of the surrounding medium, ε_o.[101,108,109]

Suppose an electromagnetic wave described by $\boldsymbol{E}_0 = E_0\,\mathbf{x}$ where E_0 is the electric field and $\mathbf{x}$ is the unit vector in the direction of the field, is incident on a spherical metal nanoparticle of radius *a*. The electromagnetic field surrounding the particle can be described by solving LaPlace's equation which forms the fundamental basis of electrostatics, $\nabla^2\varphi = 0$, where φ is the electric potential and the field $\boldsymbol{E}$ around the particle is related to φ by $\boldsymbol{E} = -\nabla\varphi$. The solution to this problem requires the application of two boundary conditions to the quasi static approximation of Mie theory: (i) φ is continuous at the sphere surface and (ii) the normal component of the electric displacement $\boldsymbol{D}$ is also continuous where $\boldsymbol{D}$ is defined as $\boldsymbol{D} = \varepsilon\boldsymbol{E}$ ($\boldsymbol{E}$ is the electric field and ε is the dielectric constant of the metal) [109]. Restricting the solution to only *L = 1* term (the dipole term only), it has been previously shown that the resulting φ can be solved to determine the field outside the metal nanosphere $\mathbf{E}_{out}$:[109]

$$\mathbf{E}_{out} = \mathrm{E}_0\mathbf{x} - \alpha\mathrm{E}_0\left[\frac{\mathbf{x}}{\mathrm{r}^3} - \frac{3x}{\mathrm{r}^5}(x\mathbf{x} + y\mathbf{y} + z\mathbf{z})\right] \qquad \text{Eq. 3.15}$$

where $\mathrm{E}_0\,\mathbf{x}$ is the incident wave, α is the metal sphere polarizability and $\mathbf{x}$, $\mathbf{y}$, and $\mathbf{z}$ are the usual Cartesian unit vectors. Hence the first term in the right hand side of Eq. 3.15 is the applied incident electromagnetic field and second term is the induced dipole field that results from the polarization of the conduction electron density.

It has been shown that for a metal nanosphere with a frequency dependent dielectric constant, the LaPlace equation gives the metal polarizability as:[109]

$$\alpha = g_{\mathrm{d}}a^3 \qquad \text{Eq. 3.16(A)}$$

where:

$$g_{\mathrm{d}} = \frac{\varepsilon_i - \varepsilon_0}{\varepsilon_i + 2\varepsilon_0} \qquad \text{Eq. 3.16(B)}$$

here ε_i is the complex frequency dependent dielectric constant of the metal ($\varepsilon_i(\omega) = \varepsilon_{iR}(\omega) + i\varepsilon_{iI}(\omega)$.....where ε_{iR} and ε_{iI} are respectively the real and imaginary portions of the metal dielectric constant) and ε_0 is the dielectric constant of the embedding medium which is taken to be a dielectric material (i.e. with a constant real component and zero imaginary component of its dielectric constant in the visible and near-infrared region of the electromagnetic spectrum) [101,109]. Using the dipole field equation terms of the Eq. 3.15 and Eq. 3.16(A-B), the extinction and scattering efficiencies of the metal nanosphere has been expressed as:[109]

$$Q_{ext} = 4x\,\mathrm{Im}(g_{\mathrm{d}}) \qquad \text{Eq. 3.17(A)}$$

$$Q_{sca} = \frac{8}{3}x^4\left|g_{\mathrm{d}}\right|^2 \qquad \text{Eq. 3.17(B)}$$

where Q_{ext} and Q_{sca} are the extinction and scattering efficiencies respectively and $x = 2\pi a(\varepsilon_0)^{1/2}/\lambda$. Both Q_{ext} and Q_{sca} are can be related to the metal and embedding medium dielectric constant in the following manner:

$$Q_{ext}\ \&\ Q_{sca} \propto \frac{1}{(\varepsilon_{iR} + 2\varepsilon_0)^2 + \varepsilon_{iI}^{\ 2}} \qquad \text{Eq. 3.17(C)}$$

The absorption efficiency is then computed as $Q_{\mathrm{abs}} = Q_{\mathrm{ext}} - Q_{\mathrm{sca}}$. The extinction or scattering efficiency is simply the ratio of the extinction or scattering cross section to the geometric cross section of the metal nanoparticle πa^2. It is important to note the key role played by the term g_{d} in determining the wavelength dependence of the cross sections.

This is because the metal dielectric function ε_i is strongly dependent on wavelength. Hence strong resonance conditions occur when the polarizability and extinction shows a maximum at wavelengths where the magnitude of $\varepsilon_i + 2\varepsilon_0$ (i.e. the denominator of Eq. 3.17(C)) is minimum. This occurs when $\varepsilon_{iR} = -2\varepsilon_0$.and ε_{iI} is small.

The equations derived above apply to particles in the quasi-static regime where only the dipole oscillations contribute to the extinction, scattering and absorption cross sections. In the case of larger particles higher multipoles ($L > 1$), especially the quadrupole term ($L = 2$) become important in the extinction and scattering spectra. Retaining the same notation as the dipole equations above and including the $L = 2$ quadrupole term in the LaPlace equation solution, the resulting field outside the sphere $\mathbf{E}_{out}$ can now be expressed as:[109]

$$\mathbf{E}_{out} = \mathrm{E}_0\mathbf{x} + \mathrm{ikE}_0(x\mathbf{x} + z\mathbf{z}) - \alpha\mathrm{E}_0\left[\frac{\mathbf{x}}{\mathrm{r}^3} - \frac{3x}{\mathrm{r}^5}(x\mathbf{x} + y\mathbf{y} + z\mathbf{z})\right] - \beta\mathrm{E}_0\left[\frac{x\mathbf{x} + z\mathbf{z}}{\mathrm{r}^5} - \frac{5z}{\mathrm{r}^7}(x^2\mathbf{x} + y^2\mathbf{y} + xz\mathbf{z})\right] \quad \text{Eq. 3.18}$$

where α is the dipole polarizability as described by Eq. 3.16(A) and β is the quadrupole polarizability described by:[109]

$$\beta = g_q a^5 \quad \text{Eq. 3.19(A)}$$

where

$$g_q = \frac{\varepsilon_i - \varepsilon_0}{\varepsilon_i + 3/2\varepsilon_0} \quad \text{Eq. 3.19(B)}$$

Using the above terms and using a similar derivation like the dipole only case, the (dipole + quadrupole) expressions for the extinction and scattering cross section efficiencies can be represented as:[109]

$$Q_{ext} = 4x\,\mathrm{Im}\left[g_{\mathrm{d}} + \frac{x^2}{12} g_{\mathrm{q}} + \frac{x^2}{30}(\varepsilon_i - 1) \right] \qquad \text{Eq. 3.20(A)}$$

$$Q_{sca} = \frac{8}{3} x^4 \left\{ \left| g_{\mathrm{d}} \right|^2 + \frac{x^4}{240} \left| g_{\mathrm{q}} \right|^2 + \frac{x^4}{900} \left| \varepsilon_i - 1 \right|^2 \right\} \qquad \text{Eq. 3.20(B)}$$

An important point to note when comparing Eq. 3.16(B) and Eq. 3.19(B) is the condition required for dipole plasmon resonance is ε_i = -2 ε_{o} and that for the quadrupole resonance is ε_i = -3/2 ε_{o}. For noble metals in the visible and near infrared region, the real part of the dielectric constant decreases (becomes more negative) with increasing wavelength (it approaches -α at infinite λ) and thus for a constant embedding medium the location of the dipole resonance will always be at a longer wavelength than that of the quadrupole resonance.

Metal nanoshells are a unique class of nanostructures with controlled nanoparticle geometry that provide new and tunable optical properties that solid metal nanoparticle do not possess.[111-128] Metal nanoshells consist of a nanometer-sized dielectric core with radius r_1 surrounded by a thin metal shell of thickness r_2 - r_1. These structures have the unique feature of a highly tunable plasmon resonance wavelength that can be achieved by the geometric tuning of the ratio of the core radius to the total radius (r_1/ r_2). The tunable range extends from the visible region of the electromagnetic

spectrum to the near-infrared.[112-128] Although a theoretical description of the optical properties of metal nanoshells based on Mie scattering theory has existed for sometime,[129-130] such nanostructures have only been realized in recent times through advances in nanofabrication techniques. A schematic of the nanoshell geometry is provided in Figure 3.20 and the discussion of its optical properties will follow.[115]

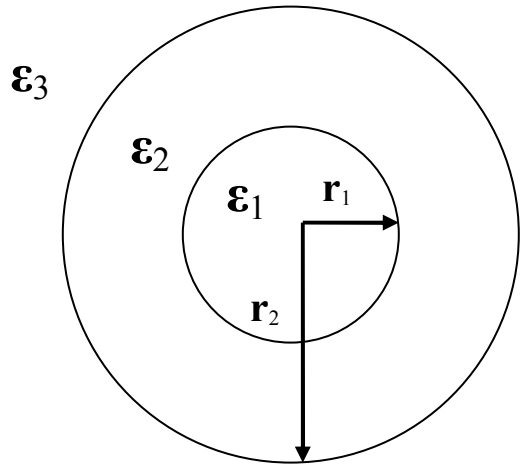

Figure 3.20: Nanoshell geometry. Here ε_i *(i = 1, 2, 3)* are the dielectric functions of the core, shell and embedding region respectively. r_1 is the core radius and r_2 is the total particle radius with the metal shell thickness = $r_2 - r_1$.

The optical properties of metal nanoshells in the quasi-static regime (only $L = 1$ dipole term) can be derived from Mie scattering theory in manner similar to that of the solid metal nanoparticles described above. It involves one additional step where the boundary conditions described for the solid metal nanoparticles is applied to one additional interface i.e. the dielectric core – metal shell interface. As shown in Figure

3.20, region 1 is the area of the dielectric core with dielectric function ε_1 (with radius r_1), while region 2 is the area of the metal shell with dielectric constant ε_2 (shell thickness is $r_2 - r_1$ where r_2 is the total particle thickness). Finally region 3 is the area of the embedding medium (such as air or water) with dielectric constant ε_3. It has been shown that adding the necessary boundary condition to the electric potential in each region and solving for the electric field in each region using the LaPlace's equation results in:[115, 130]

$$\mathbf{E}_1 = \frac{9\varepsilon_2\varepsilon_3}{\varepsilon_2\varepsilon_a + 2\varepsilon_3\varepsilon_b} E_0 (\cos\theta \mathbf{r} \quad \sin\theta\boldsymbol{\theta}) \qquad \text{Eq. 3.21(A)}$$

$$\mathbf{E}_2 = \frac{3\varepsilon_3}{\varepsilon_2\varepsilon_a + 2\varepsilon_3\varepsilon_b} \begin{Bmatrix} \left[(\varepsilon_1 + 2\varepsilon_2) + 2(\varepsilon_1 \quad \varepsilon_2) \times (r_1/r)^3\right] E_0 \cos\theta \mathbf{r} \\ \left[(\varepsilon_1 + 2\varepsilon_2) \quad (\varepsilon_1 \quad \varepsilon_2)(r_1/r)^3\right] E_0 \sin\theta\boldsymbol{\theta} \end{Bmatrix} \qquad \text{Eq. 3.21(B)}$$

$$\mathbf{E}_3 = \left(2 \frac{\varepsilon_2\varepsilon_a - \varepsilon_3\varepsilon_b}{\varepsilon_2\varepsilon_a + 2\varepsilon_3\varepsilon_b} \frac{r_2^3}{r^3} + 1 \right) E_0 \cos\theta \mathbf{r} +$$

$$\left(\frac{\varepsilon_2\varepsilon_a - \varepsilon_3\varepsilon_b}{\varepsilon_2\varepsilon_a + 2\varepsilon_3\varepsilon_b} \frac{r_2^3}{r^3} - 1 \right) E_0 \sin\theta\boldsymbol{\theta} \qquad \text{Eq. 3.21(C)}$$

where

$$\varepsilon_a = \varepsilon_1(3 - 2P) + 2\varepsilon_2 P \qquad \text{Eq. 3.22(A)}$$

$$\varepsilon_b = \varepsilon_1 P + \varepsilon_2(3 - P) \qquad \text{Eq. 3.22(B)}$$

$$P = 1 - (r_1/r_2)^3 \qquad \text{Eq. 3.22(C)}$$

where $\mathbf{E}_i$ (where i = 1, 2, 3) represents the position dependent complex electric vector fields in the core, shell and surrounding medium respectively, E_0 is the magnitude of the incident beam and P represents the ratio of the shell volume to the total particle volume.[115, 130]

The induced dipole field in the region outside the shell can be represented as a dipole with effective moment $\mathbf{p} = \varepsilon_3 \alpha \mathbf{E}_0$ where the polarizability α can be expressed as:[115]

$$\alpha = 4\pi\varepsilon_0 r_2^3 \quad \frac{\varepsilon_2\varepsilon_a \quad \varepsilon_3\varepsilon_b}{\varepsilon_2\varepsilon_a + 2\varepsilon_3\varepsilon_b} \qquad \text{Eq. 3.23}$$

where ε_0 is the permittivity of free space and equals 8.85×10^{-12} F/m.

The absorption and scattering cross sections of the metal nanoshells has been computed from the polarizability and scattering theory and are:[115, 130]

$$\sigma_{sca} = \frac{1}{6\pi\varepsilon_0^2} k^4 |\alpha|^2 = \frac{128\pi^5}{3\lambda^4} \varepsilon_3^2 r_2^6 \left| \frac{\varepsilon_2\varepsilon_a \quad \varepsilon_3\varepsilon_b}{\varepsilon_2\varepsilon_a + 2\varepsilon_3\varepsilon_b} \right|^2 \qquad \text{Eq. 3.24(A)}$$

$$\sigma_{abs} = \frac{k}{\varepsilon_0} \mathrm{Im}(\alpha) = \frac{8\pi^2\sqrt{\varepsilon_3}}{\lambda} r_2^3 \ \mathrm{Im} \ \frac{\varepsilon_2\varepsilon_a \quad \varepsilon_3\varepsilon_b}{\varepsilon_2\varepsilon_a + 2\varepsilon_3\varepsilon_b} \qquad \text{Eq. 3.24(B)}$$

The extinction cross section can then be represented as $\sigma_{ext} = \sigma_{sca} + \sigma_{abs}$. Equations 3.24(A) and 3.24(B) uses the quasi-static approximation of Mie theory to describe both the scattering as well as absorption cross sections as a function of the ratio of the core radius to the total particle radius (incorporated in the ε_a and ε_b terms). Using equations 3.24(A) and 3.24(B) with gold sulfide (Au_2S) as the dielectric core, gold (Au) as the shell layer and using $\varepsilon_3 = 1.78$, Averitt *et al.*[115] calculated the extinction cross sections of gold nanoshells with a 2 nm shell thickness and with total radius r_2 at 4, 10 and 17 nm (increase in core diameter) and compared them with the results obtained from more complex complete Mie theory calculations which used ten multipole terms (L = 1…..10). The results are shown below in Figure 3.21 where circles represent calculations

using the quasi-static approximation and solid curves represent the calculations using generalized Mie scattering theory.[115] These results show that for a given shell thickness r_2, a larger particle size (larger core i.e. larger core/shell ratio) will yield a plasmon resonance that is shifted to longer wavelengths. The results also show good agreement between the two calculations thus justifying the use of quasi-static approximation for particles in this size regime.[115]

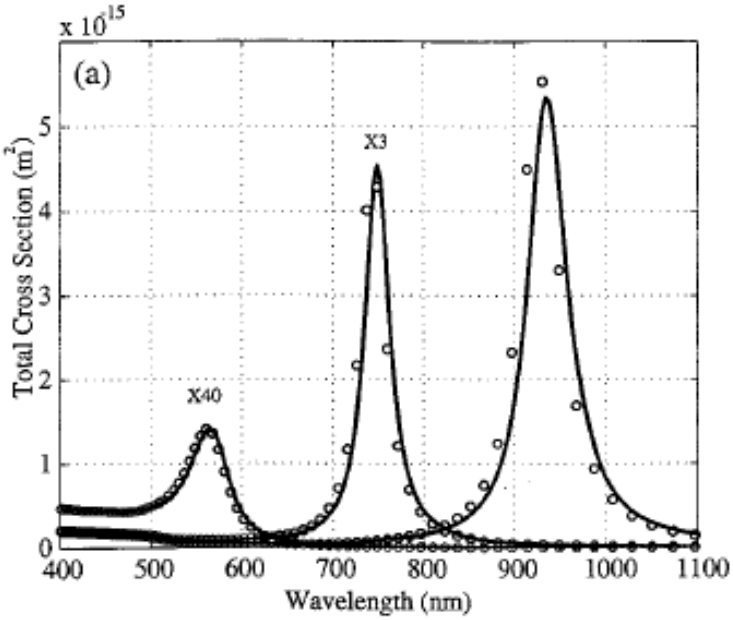

Figure 3.21: Results of calculations of the total extinction cross section vs. wavelength for gold nanoshells with a 2 nm shell thickness. The total particle radius r_2 is 4, 10 and 17 nm from left to right. Circles represent calculations in the quasi-static limit and solid lines represent calculations using generalized Mie scattering theory. Reprinted with permission from R. D. Averitt, S. L. Westcott, and N. J. Halas, "The linear optical properties of gold nanoshells," *J. Opt. Soc. Am. B* **16**(10), 1824-1832 (1999). Copyright 1999, The Optical Society of America.[115] http://www.osa.org/.

Equation 3.23 shows that the resonance condition for a metal nanoshell is obtained when the real portion of the denomination goes to zero i.e. when Re($\varepsilon_2 \varepsilon_a + 2\varepsilon_3$

$\varepsilon_b) = 0$. Since the core and dielectric medium are dielectrics with $\mathrm{Im}(\varepsilon_i) = 0$ ($i = 1, 3$), the following expression for the resonance condition as a function of wavelength has been derived.[115]

$$\frac{r_1}{r_2} = \left[1 + \frac{3}{2} \frac{\varepsilon_2'(\lambda)(\varepsilon_1 + 2\varepsilon_3)}{[\varepsilon_2'(\lambda)]^2 - \varepsilon_2'(\lambda)(\varepsilon_1 + \varepsilon_3) + \{\varepsilon_1\varepsilon_3 - [\varepsilon_2''(\lambda)]^2\}} \right]^{1/3} \qquad \text{Eq. 3.25}$$

This expression shows the ratio of the core radius to the total particle radius that is required to design a metal nanoshell with plasmon resonance located at specific wavelengths. This expression shows the geometric tunability which is an inherent property of metal nanoshells. Although the derivations above are accurate when limited to particles in the quasi-static size regime, they do provide a qualitative appreciation of the underlying principles that govern the optical properties of metal nanoshells of all sizes.

The goal of this study was to characterize the structure and optical properties of gold nanoshells immobilized on microscope glass slides as a thin film using UV-Vis absorption spectroscopy, Atomic Force Microscopy (AFM) and SERS. The characterization was aimed at studying the efficacy and feasibility of using gold nanoshell films as potential platforms for the development of SERS based biosensors for the detection of a myriad of bioanalytes. Although the gold nanoshells films are fabricated by immobilizing individual gold nanoshells via a linker layer on the surface of microscope glass slides, their optical properties (e.g. plasmon resonance wavelength) are still governed by the nature of the individual nanoshells used in the fabrication. It has been shown by Jackson *et al*.[128] that the extinction spectra of nanoshell films contains

two important features: the plasmon resonance band arising from the isolated single nanoshell resonance and the nanoshell aggregate resonance that appears at longer wavelengths (> 1600 nm) which increases in magnitude as the density of packing increases. The increase in density of nanoshell packing also simultaneously increases the magnitude of the single nanoshell resonance.[128] The nanoshell films were provided for this research by Nanospectra Biosciences Inc. (Houston, TX), a collaborator with the Optical Biosensing Laboratory at Texas A&M University. The strong Raman active molecule *trans*-1,2-bis(4-pyridyl)ethylene (BPE) was used to study the variability of SERS response by the nanoshell films at different areas of the film as well as to observe the overall responsiveness of the substrate to increasing BPE concentrations.

Materials and Methods

Gold nanoshell films were fabricated at Nanospectra Bioscience Inc. according to the procedure described by Jackson *et al*. [128] where ultra clean microscope glass slides were submerged in a 1% solution in ethanol of Poly(4-vinylpyridine) (PVP) for approximately 12 hours. The PVP acted as a linker molecule to attach the gold nanoshells to the glass surface. After removing and rinsing the PVP coated slides with ethanol, they were submerged in an aqueous gold nanoshell suspension. The nanoshells used for these experiments were approximately 200 nm in diameter (180 nm diameter silica core and 15-20 nm gold shell thickness). The nanoshell deposition time on the PVP coated slide was in the range of 15 – 20 hours to obtain adequate nanoshell density on the glass slide after which the slides were removed and rinsed with water, dried and

shipped to the Optical Biosensing Laboratory. The nanoshell films came in the form of eight separate wells on each individual glass slide.

The UV-Vis absorption characterization studies were done with the identical set up as shown in Figure 3.1. The only unique parameters were the integration time which was 20 seconds and the location of the diffraction grating which was centered at 800 nm and thus had a window between 560nm and 1020nm. Here too a clean microscope glass slide served as the blank.

The AFM studies were done with the same microscope and tip as mentioned in page 26. The SERS studies were performed by dropping a 10 μl solution of 5, 50 and 500 μM BPE solution (in acetone) on separate wells and allowed to dry before obtaining SERS spectra. The SERS studies were performed with the same Renishaw system as described previously. In this case SERS spectra were obtained for each BPE concentration at 24 different locations on two gold nanoshell film coated slides with each spectra collected between 500 – 2000 cm^{-1} with a 30 second integration time. All data analysis were performed as described in pages 31 and 32.

Results and Discussion

Figure 3.22 shows the extinction spectrum of the gold nanoshell films which were collected with a 20 second integration time. Here it is clearly seen that the extinction maximum (λ_{max}) is located at approximately 700 nm. Although the nanoshells film was originally intended to have its extinction maximum located at 785 nm (to match the wavelength of the laser used for the SERS studies), it is possible that defects in the

original nanoshell suspension used to create the films as well as problems with the film formation procedure caused this deviation.

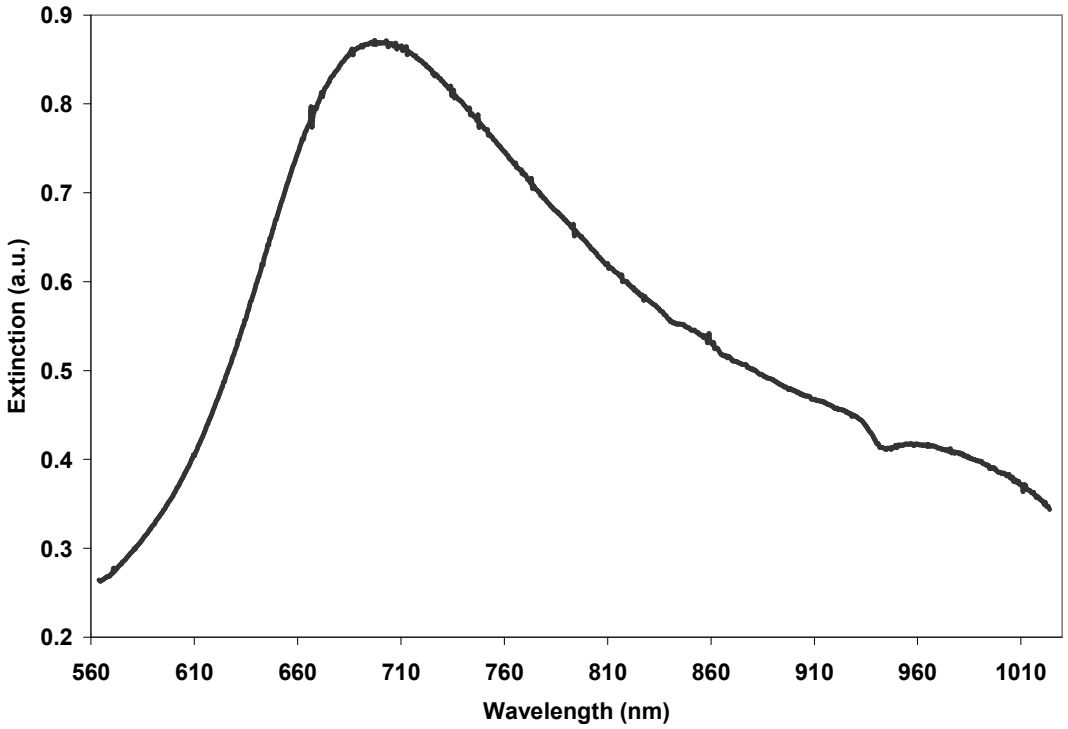

Figure 3.22: Extinction spectrum of a gold nanoshell film on a glass substrate showing an extinction maximum located at approximately 700 nm.

Figures 3.23(A) and 3.23(B) show a 10 μm × 10 μm and a 5 μm × 5 μm sized AFM images taken of the gold nanoshell films respectively. These images show spherical gold nanoshells on the glass surface. The nanoshells do not pack in any ordered shape and seem randomly distributed throughout the surface. This contrasts with the well ordered hexagonally close packed uniform packing of nanoparticles using Nanosphere Lithography (NSL). The introduction of some sort of lithographic mask in the

fabrication process might help enhance control of surface uniformity. It is quite possible that the areas in the glass that did not have any gold nanoshell coverage could be due to insufficient coating of the PVP linker layer or due to insufficient density of the deposited gold nanoshells. The gold nanoshell density problem can be mitigated by increasing the amount of time that the PVP coated slide remains submerged in the aqueous nanoshell suspension. The gold nanoshell density might also be increased by the addition of (a higher concentration) of sodium chloride midway during the gold deposition step as this helps to neutralize the nanoshell surface charge and increase nanoshell packing density.[128] Figure 3.24 shows a section analysis performed on the 5 μm × 5 μm AFM image. The results of the section analysis reveals that the vertical height of the nanoshells are approximately 230 nm which is in good agreement with the size of the nanoshells mentioned earlier (≈200 nm). Figure 3.24 also reveals that the horizontal size of the nanoshells to be approximately 440 nm. This is however misleading as spherical nanoshells should have a size of approximately 200 nm in all dimensions. This is the result of in plane feature size broadening which is a common problem associated with AFM studies and have been discussed in page 46 for AFM analysis on silver periodic particles array formed using Nanosphere Lithography.[79, 86-89]

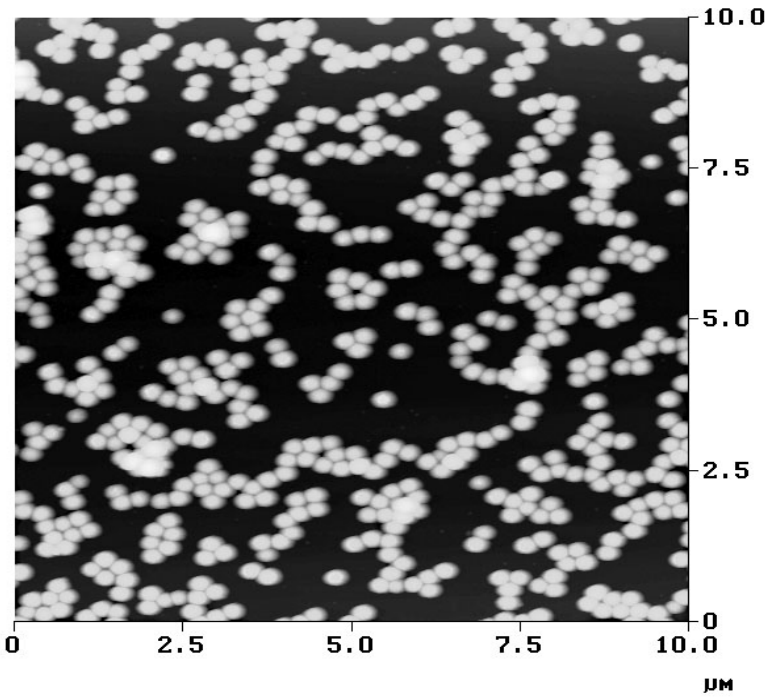

Figure 3.23(A): 10 µm × 10 µm AFM image of gold nanoshells on a glass substrate.

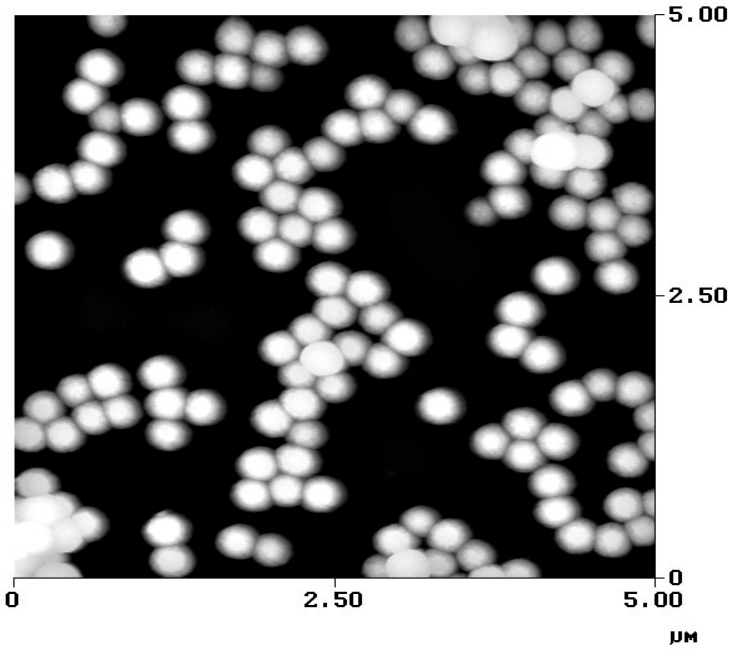

Figure 3.23(B): 5 µm × 5 µm AFM image of gold nanoshells on a glass substrate.

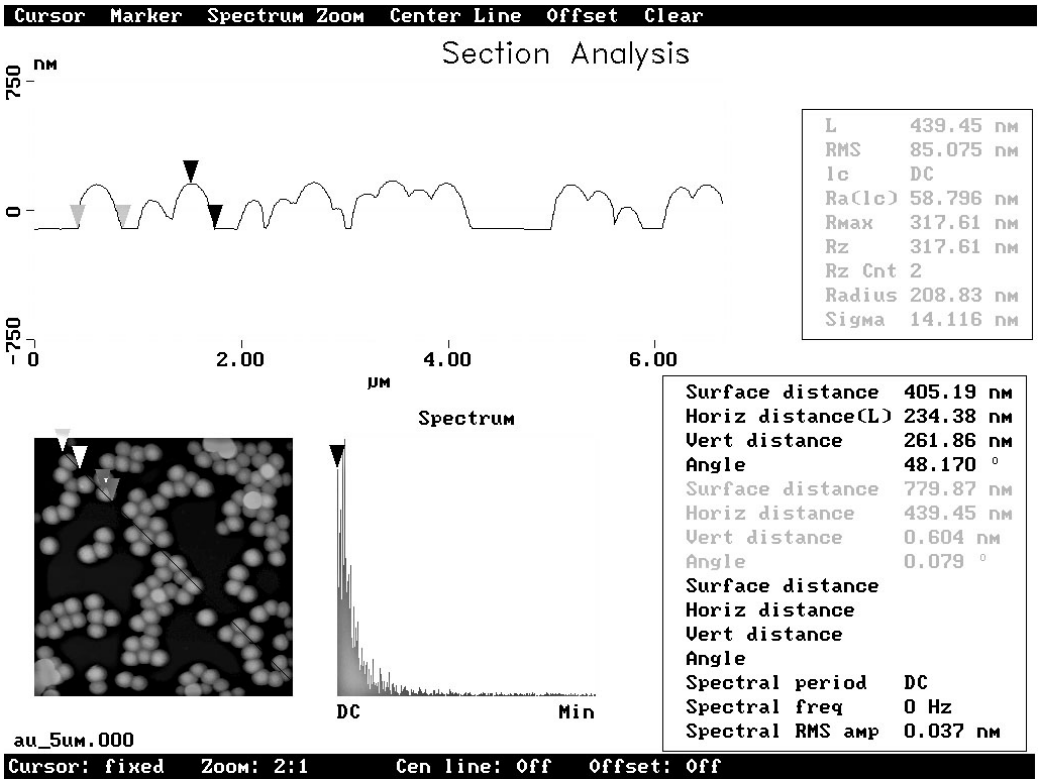

Figure 3.24: Section analysis performed on a 5 µm × 5 µm AFM image of gold nanoshells on a glass substrate.

The results of the SERS characterization studies performed with BPE on the gold nanoshell films are shown in Figures 3.25(A) and 3.25(B). Figure 3.25(A) shows the SERS spectrum resulting from averaging 24 spectra collected at separate locations on the gold nanoshell film coated with 50 µM BPE. The four distinct BPE SERS peaks located at 1633, 1608, 1200 and 1000 cm^{-1} are clearly seen. Figure 3.25(B) shows the average height of these four major BPE peaks in the 24 location along with the standard error in the data. The data shows very low variability in the height of the peaks at 24 different locations. Figure 3.26 shows the average of 24 scans at different locations in

the gold nanoshell films coated with 5, 50 and 500 μM BPE respectively. This figure shows excellent response of the gold nanoshell films to increasing concentrations of BPE. It can however be said that the 5 μM BPE spectrum was approaching the detection limit of the experimental system (at 30 sec integration time). The strength of the 5 μM BPE spectrum could be increased by increasing the integration time for the scans, but this was leading to saturation of the CCD camera for the case of the 500 μM BPE samples. This would not allow for a fair concentration response study and hence 30 sec integration for each scan was accepted as the consensus.

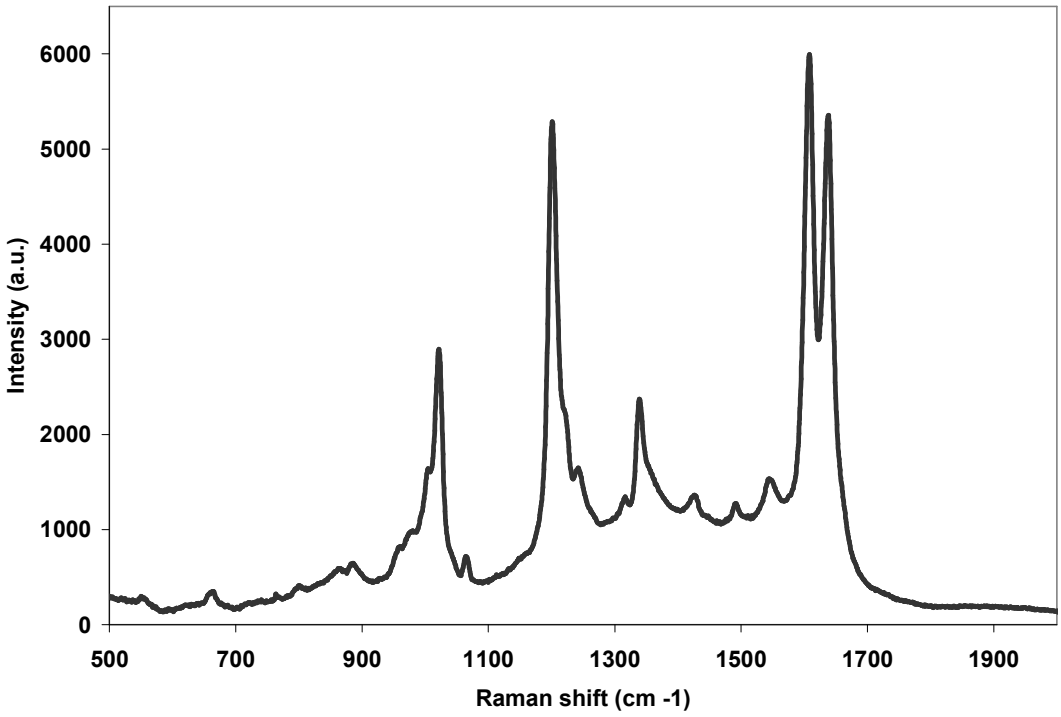

Figure 3.25(A): Average SERS spectrum collected from 24 separate locations on a gold nanoshell film coated with 50 μM BPE.

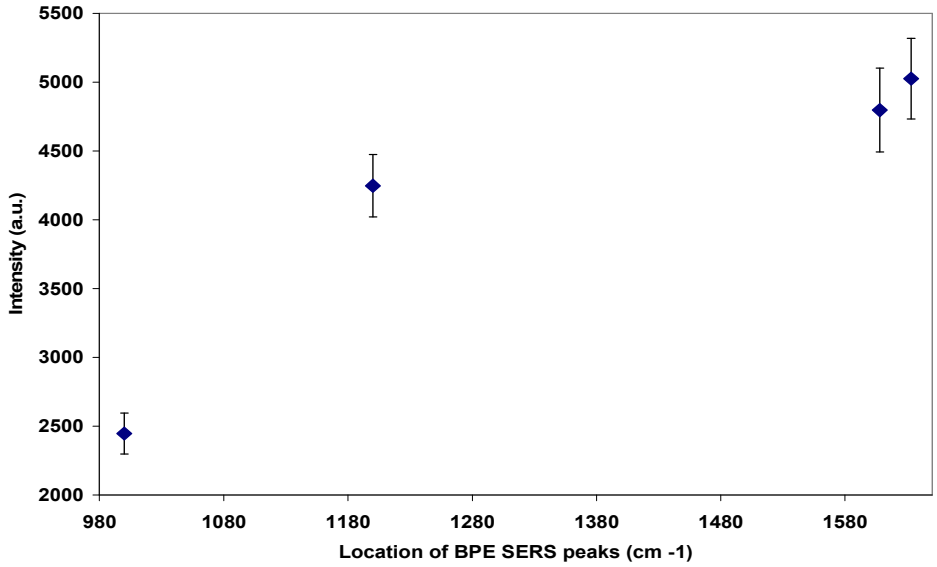

Figure 3.25(B): Average intensity of the major BPE SERS peaks from spectra collected at 24 separate locations on a gold nanoshell film coated with 50 µM BPE. It includes the standard error showing the spread in the data. The data shows good consistency between different locations.

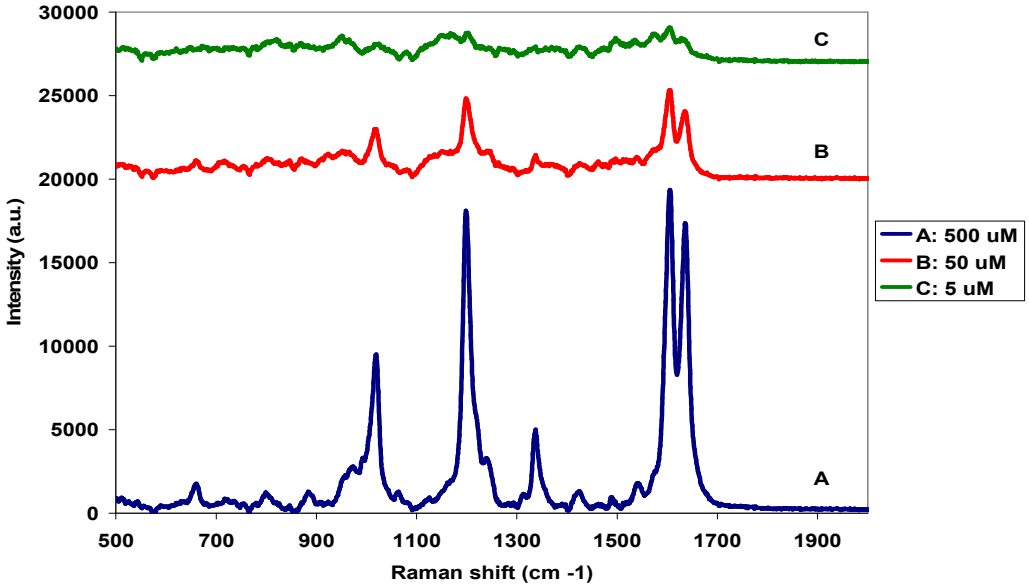

Figure 3.26: Average SERS spectra from 24 different locations each on gold nanoshell films showing the response of the films to increasing concentration of BPE. The spectra are for 500 µM (A), 50 µM (B) and 5 µM (C) of BPE and are purposely separated for reasons of increased clarity.

CHAPTER IV

DEVELOPMENT OF A SERS BASED BIOSENSOR FOR THE DETECTION OF β-AMYLOID

Significance and Pathology of Alzheimer's Disease and Current Methods for β-amyloid Detection

Alzheimer's disease (AD) is a progressive neurodegenerative disease that affects 16 million people worldwide and is characterized by memory loss and cognitive impairment.[106-107, 131-136] It is the leading cause of dementia in people over 65, affects over 4 million Americans and is characterized by various pathological markers in the brain such as: (a) large numbers of amyloid plaques surrounded by neurons containing neurofibrillary tangles, (b) vascular damage from extensive plaque deposition and (c) neuronal cell loss.[106-107, 136] These plaques are composed primarily of fibers of the amyloid β-protein fragments (Aβ). The Aβ molecule is a 39-42 amino acid peptide, part of which forms the hydrophobic transmembrane domain in the COOH terminated portion of the larger amyloid precursor protein (APP).[136] It is derived by the proteolytic processing of APP within acidic intracellular compartments such as the early endosome or distal Golgi complex.[135] Although Aβ is actually a normal component of neuronal cells and is found commonly in cerebrospinal fluid (CSF), it is believed that AD is linked to chronic elevations in brain levels of Aβ which can be related with familial risk factors such as mutations in APP or other risk factors such as head trauma.[134, 137] At

such elevated conditions, thermodynamic stability of the relatively unstable Aβ favors its self-association into oligomers such as amyloid-β-derived diffusible ligands (ADDL) followed at higher concentrations by further self-association into higher ordered structures such as protofibrils and the macroscopic fibrils.[106-107,134-137] It is these macroscopic fibrils which are highly β-sheet in structure and are an essential part of the senile plaques that are commonly associated with AD. The different assembled states of Aβ obtained from synthetic preparation from monomers is shown in Figure 4.1.

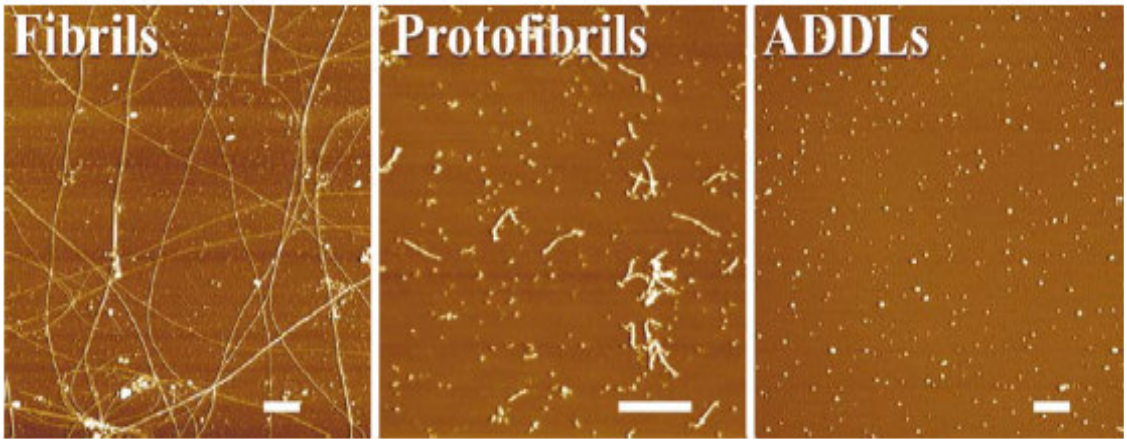

Figure 4.1: AFM images of different assembled states of amyloid β (Aβ). The assembled forms were obtained from incubation of synthetic Aβ. Scale bar is 200 nm. Reprinted from *Trends in Neuroscience*s, **24**(4), W.L. Klein, G.A. Krafft, and C.E. Finch, "Targeting small Aβ oligomers: the solution to an Alzheimer's disease conundrum," 219-224, Copyright (2001), with permission from Elsevier.[134]

The symptoms of the disease begin with mild cognitive impairment that cannot be distinguished from other more benign forms of age-related dementia. Even as the disease progresses, an affirmative clinical diagnosis of the disease is not always successful. There is still no definitive diagnosis of the disease other than postmortem

identification of senile plaques and neurofibrillary tangles in the brain.[106-107, 131-132,138] Work is currently underway to develop a definitive pre-mortem detection method for AD using a wide variety of modalities. These include *in-vivo* brain imaging using Magnetic Resonance Imaging (MRI) and Positron Emission Tomography (PET).[139-141] Although these techniques have been able to detect neuronal cell atrophy as well as alteration in patterns of brain activity in patients with AD when compared with aged matched control patients, no proof has been established that can correlate such irregularities definitively with AD. Hence the possibility of false positive results emerging when diagnosing a patient for AD using such techniques looms large.

Pietschke *et al.* have used Fluorescence Correlation Spectroscopy (FCS) to detect amyloid β-protein aggregates in cerebrospinal fluid of patients with AD.[142] This technique involved the use of an exogenous fluorophore (Cy2) labelled synthetic Aβ peptides for aggregation around Aβ multimers in CSF of patients with AD which acted as "seeds" for polymerization. Although this technique showed promising results for detection of the presence of native Aβ multimers in CSF of AD patients, it is limited by the use of an exogenous fluorophore as well as the use of synthetic Aβ monomers. The functionalization of peptides in many cases can affect its binding/polymerization capability and hence can limit the efficiency of such a system. This technique also involved the use of the surfactant Sodium Dodecyl Sulfate (SDS) to keep the synthetic Aβ peptides in solution. The use of surfactants is not optimal for any bio-analyte detection scheme as it is a physiologically unnatural molecule and hence does not allow the detection of the target analyte in its native state.

There are have been several notable advances in the use of nanotechnology for the development of techniques for the detection of the Aβ oligomers ADDL's. Georganopoulou *et al.* used a novel assay called the bio-barcode amplification assay to measure the concentration of ADDL's in the CSF of patients with Alzheimer's Disease.[131-132,143-144] This assay uses magnetic particle probes (MMP Probe) functionalized with Monoclonal Antibodies (mAbs) that recognize and bind to ADDL's. The ADDL's are then sandwiched with a nanoparticle probe (NP) that is functionalized with a polyclonal anti-ADDL Antibody (pAb) and a double stranded DNA, one strand of which is the barcode DNA. After repeated washing steps while using a magnet to immobilize the MMPs, the barcode DNA strands for each ADDL binding event are then released via a dehybridization step. The released barcode DNA (if necessary is also PCR amplified) are then captured by immobilization on a capture DNA modified glass slide and a silver enhanced gold nanoparticle based light scattering technique is then used to indirectly quantify the captured barcode DNA. This is then correlated to the initial amount of ADDL's in the test sample.[131-132] Although this technique boasts an impressive sensitivity in the range of 100 aM (100×10^{-18} M), it is also quite complicated requiring the need of several kinds of nanoparticles and multiple intermediate steps. This complexity requires highly trained personnel to perform the assay adequately and thus does not make it favorable for use in clinical settings. It is also an indirect quantification of ADDL's and hence susceptible to false positives.

Haes *et al*. have recently reported the development of a localized surface plasmon resonance based nanosensor for the detection of ADDL's in both brain extracts

and CSF of patients with AD.[106-107] This technique exploits the change in the localized surface plasmon resonance (LSPR) condition on anti-ADDL pAb's functionalized silver nano-structures fabricated by the process of Nanosphere Lithography upon binding of ADDL's. This binding event causes a change in the refractive index in the area surrounding the silver nanoparticle and thus alters the nature of its interaction with an incident electromagnetic wave. The change in the condition is manifested as a red shift in the extinction spectra of the silver nanostructure surface when illuminated with white light in transmission geometry. This technique also involves a signal amplification step with a sandwich assay where a secondary anti-ADDL pAb is used to bind to the immobilized ADDL on the primary anti-ADDL pAb. This causes a further change in the refractive index around the silver nanostructures and thus an increase in the red shift of the LSPR wavelength. Although this study claims to successfully detect differences in ADDL concentrations in human brain samples and CSF between patients with AD and aged matched control patients, the data presented is not convincing.

This is because the sensitivity of the system in terms of the red shift in the LSPR wavelength does not change with the use of mAb's instead of pAb's on the silver nanoparticles. It is well established that mAb's have higher affinity for an antigen than pAb's and hence its use should increase the amount of ADDL captured on the silver nanostructure leading to an increase in the red shift of the LSPR wavelength. Thus the assay based entirely on pAb's is prone to false positives. This suspicion is validated by the fact that the LSPR shift caused by ADDL's in the CSF of patients with AD lies outside the biologically relevant range (> 100 nM). In addition it is also outside the range when the model used to characterize the system breaks down.

Indirect SERS Based Detection of β-amyloid Using Congo Red

Introduction

Congo Red (CR) binding as monitored by a yellow green birefringence under cross polarization has been used as a diagnostic test for the presence of amyloid fibrils in tissue sections for decades. In some cases this test also has been used for characterizing *in vitro* amyloid fibrils.[145-150] In addition to its use for the detection of fibrils, several groups have also shown that CR binding can be used as an inhibitor of amyloid formation by stabilizing the monomeric form of Aβ and preventing the peptide from forming insoluble oligomers in cell culture.[151] As a result CR was investigated as a possible biorecognition element for use in the development of a SERS based biosensor for the detection of Aβ. An initial study was conducted to test for CR specificity for Aβ.

In this study the change in the extinction spectra and SERS spectra of CR in phosphate buffer upon binding to Aβ and a confounder molecule (Bovine Serum IgG) was monitored to determine the specificity of CR binding to Aβ.

Figure 4.2 shows the structure of the Congo Red molecule. It is suggested that the binding of CR to proteins occurs through a combination of hydrophobic and electrostatic interactions and is related to its characteristic molecular structure: two amino substituted napthalenesulfonic acid moieties connected by azo linkages to a central biphenyl group.[145-146] Studies on the binding of CR with amyloids have revealed that the sulfonic groups as well as the central conjugated rings are involved in the interaction of CR with highly β-sheet structured amyloid proteins.[146]

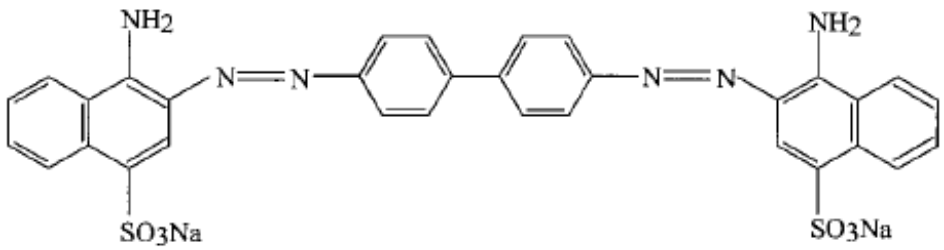

Figure 4.2: Structure of the Congo Red molecule.

Materials and Methods

Materials

Congo Red powder and Bovine Serum IgG was purchased from Sigma Alrich (St. Louis, MO), Aβ as above, Potassium Phosphate used to make Phosphate Buffer was

purchased from Sigma-Aldrich (St. Louis, MO). Silver coated glass slides were created via thermal evaporation as described in page 24.

UV-Vis Absorption Studies

20 μl of (60 μM stock) CR (dissolved in 70 mM phosphate buffer, pH = 7.2) was mixed with 180 μl of (100 μM stock) Aβ, Bovine Serum IgG, leucine and buffer respectively. These were then separately pipetted into a semi-micro quartz cuvette respectively and their extinction spectra were obtained by a Beckman DU 640 spectrophotometer. The ranges of wavelengths monitored were from 400 nm to 700 nm. The final concentration of CR in samples were 6 μM and that of each of the other analytes tested were 90 μM.

SERS Studies

5 μl of each of the samples prepared above were pipetted onto the surface of a silver coated microscope glass slide and the water was allowed to evaporate for approximately 40 min until a thin solid crust of the sample remained on the surface of the silver coated slide. The slide was then placed in a Renishaw Raman microscope with 2.3 mW excitation power from the 514.5 nm Ar^+ laser delivered to the sample. The SERS spectra were collected with the diffraction grating centered at 1400 cm^{-1} and integration time of 2 sec. All SERS spectra processing was done using the GRAMS/32 based routine (Galactic Industries Corporation, Salem, NH) which was a built-in feature of the WiRE™ software (version 1.2) that controlled the Raman spectrometer.

Results and Discussion

Figure 4.3 shows the results of the extinction spectra of CR in phosphate buffer (A), CR with leucine (B), CR with IgG (C) and CR with Aβ (D). The extinction maximum of 6 μM CR in phosphate buffer is at 490 nm (A). This maximum remains practically unchanged when CR interacts with leucine (B). The situation however is quite different when CR interacts with IgG (C). Here we see a red shift in the extinction maximum from 490 nm to 496 nm. In addition we see an increase in the magnitude of the extinction maximum. This indicates that CR is binding with the IgG. A similar situation arises when CR reacts with Aβ (D). Here we see a further red shift of the extinction maximum to 505 nm along with the appearance of a shoulder at 543 nm. An increase in the magnitude of the extinction spectra also accompanies this red shift. This again indicates a binding event with the Aβ and agrees with the results of other groups that have studied CR interaction with amyloids.[145-146,148] It is believed that an expansion of the conjugated π-electron system of CR due to a conformational change in the CR as a result of the binding event may be responsible for the red shift.[146]

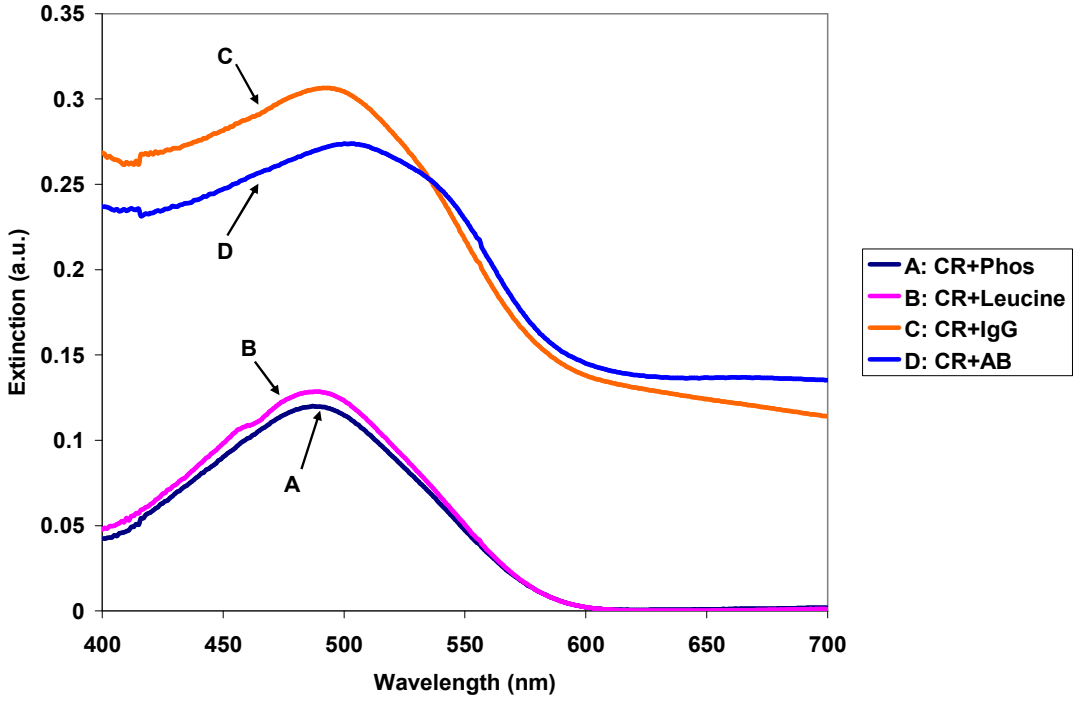

Figure 4.3: UV-Vis absorption spectra of CR in phosphate buffer (A), CR with leucine (B), CR with IgG (C) and CR with Aβ (D).

Figure 4.4 shows the results of SERS spectra taken from CR in buffer (A), CR with leucine (B), CR with IgG (C) and CR with Aβ (D) when a 5 µl drop of each was allowed to dry on a silver coated microscope glass slide. Since the laser used to excite the samples was at 514.5 nm, it resonantly excited the CR and hence the large CR signal drowned any signals from the rest of the analytes which were not resonantly excited. Hence at this particular excitation wavelength CR experienced SERRS (Surface Enhanced Resonance Raman Scattering). The major CR peaks that are observed in Figure 4.4 are the 1599 cm^{-1} peak of CR due to the C=C stretching vibrations of the naphthalene and benzene rings, the peaks between 1350 cm^{-1} and 1450 cm^{-1} which are

due to the N=N stretching modes (azo-mode frequencies) and the peak at 1155 cm^{-1} N-C stretch of the phenyl rings. [146, 148-149]

Although the SERS spectra themselves are heavily dominated by CR features, an interesting phenomena is revealed in the peaks centered around 1599 cm^{-1}. This is revealed in greater clarity when the 2nd derivative of the SERS spectra is analyzed in detail around 1599 cm^{-1}. The SERS peak locations appear as minima in the 2nd derivative spectra and hence makes it more conducive as a peak locating tool.[147] The 2nd derivative of the SERS spectra are shown in Figure 4.5(A). Figure 4.5(B) represents a blowup of the 2nd derivative spectra centered around 1599 cm^{-1} and clearly reveals that the 1599 cm^{-1} undergoes a 7 cm^{-1} blue shift when CR binds with both Rabbit IgG and Aβ (1599 cm^{-1} to 1592 cm^{-1}). This shift is not seen in the case of the interaction of CR with leucine. This blue shift again signifies a binding event that leads to a change in nature of the phenyl ring bands that are responsible for the 1599 cm^{-1} band.

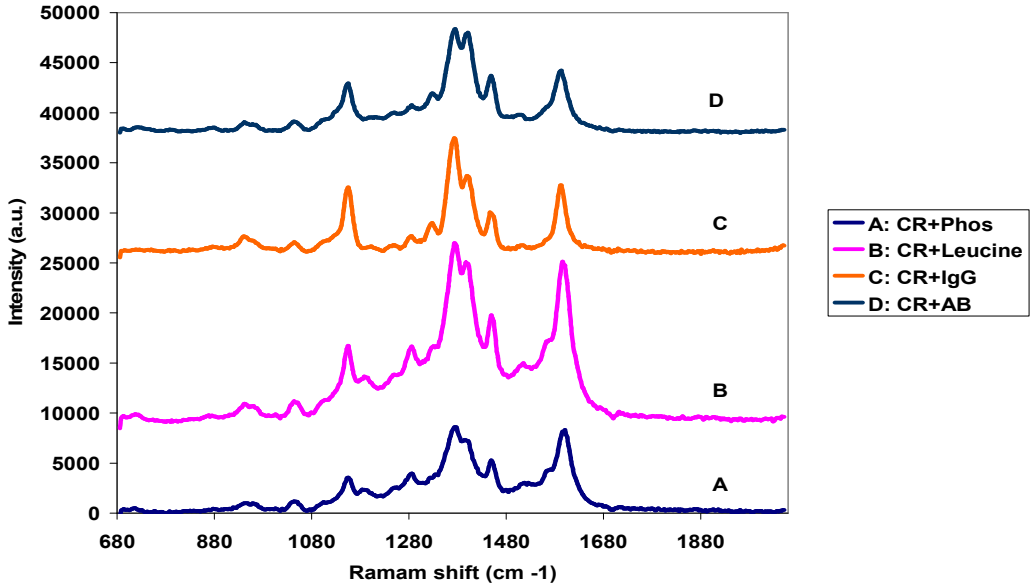

Figure 4.4: SERS spectra of a silver coated microscope slide with CR in phosphate buffer (A), CR with leucine (B), CR with IgG (C) and CR with Aβ (D).

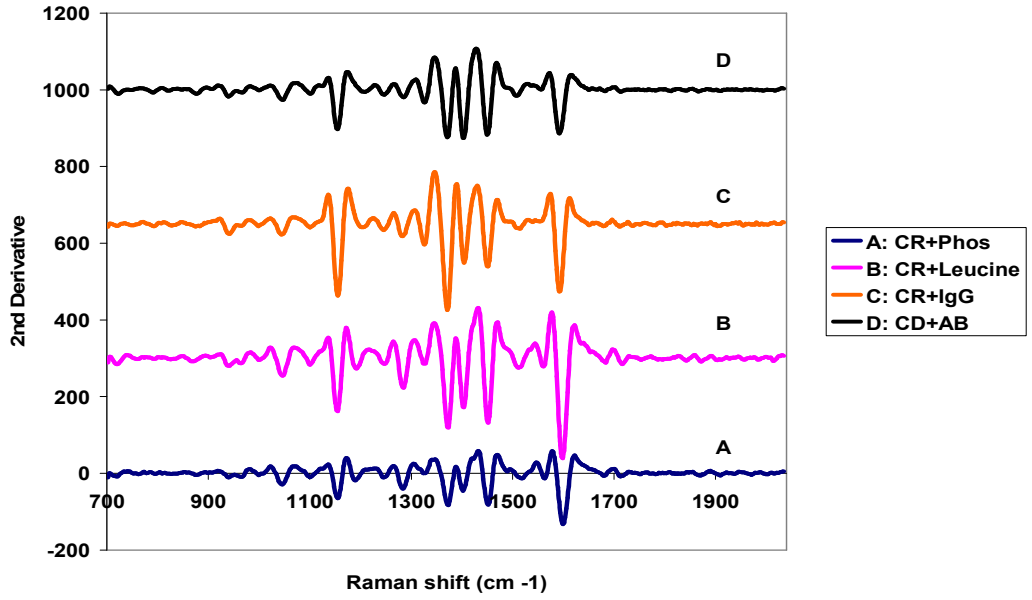

Figure 4.5(A): 2nd derivative of the SERS spectra of a silver coated microscope slide with CR in phosphate buffer (A), CR with leucine (B), CR with IgG (C) and CR with Aβ (D).

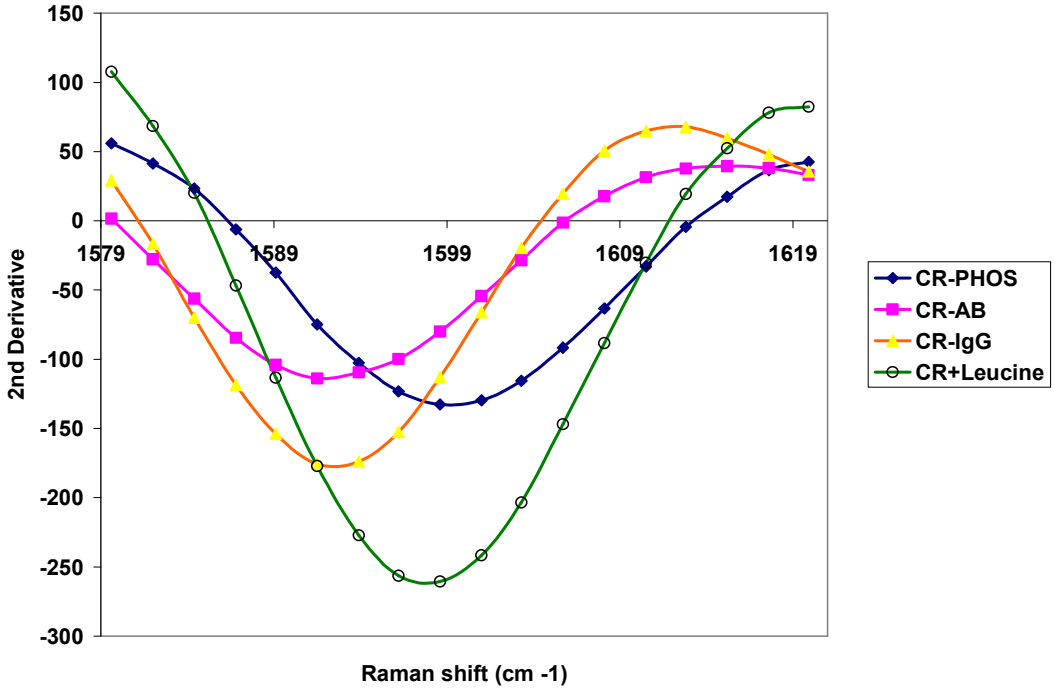

Figure 4.5(B): Blowup of the 2nd derivative of the SERS spectra around the 1599 cm^{-1} peak of a silver coated microscope slide with CR in phosphate buffer (A), CR with leucine (B), CR with IgG (C) and CR with Aβ (D).

The results of the extinction spectra along with the SERS spectra indicates that Congo Red indeed binds to both Rabbit IgG and Aβ. These results conclude that CR does not have exclusive binding selectivity to Aβ and is in agreement with conclusions reported by Khurana *et al.*[145] Hence it does not hold much promise to act as the biorecognition molecule in a biosensor for the detection of AD. Based on these results, the possibility of false positives due to CR binding to any number of proteins present in cerebrospinal fluid makes it an unattractive candidate for implementation in such a biosensor.

Feasibility Studies for Direct SERS Detection of β-amyloid Using Silver Enhanced Gold Nanoparticles

Introduction

The investigations on using Congo Red as the biorecognition molecule for Aβ were shown to be non-specific. Hence it was necessary to turn elsewhere for this research. There is currently active interest in developing a myriad of structure specific antibodies for detection of disease associated Aβ.[152-154] However, it may be possible to create other biorecognition molecules with antibody like affinity for Aβ which are of smaller molecular size, and hence may be more suited for the demands of a SERS based biosensing system. A variety of evidence indicates that β-amyloid may bind to cells via an interaction with surface glycolipids or glycoproteins, and that the affinity of this interaction increases when the gangliosides or sialic acid molecules on the cell surface are clustered.[154-158] Based on this evidence, it was decided to develop a novel biorecognition molecule for Aβ based on a sialic acid modified generation 4.0 PAMAM dendrimer that would attempt to reproduce the clustered sialic acid structure of the cell surface, with the aim of recreating the Aβ binding seen to occur on neuronal cell membranes. Before proceeding with this idea, it was imperative to design preliminary studies to determine two key issues. The first was whether Aβ would give an acceptable signal through SERS. The second was to determine if the signal from the recognition unit (dendrimer) would interfere with the signal from the Aβ.

Materials and Methods

Materials

The Aβ (1-40) was synthesized and purified by BioSource International (Camarillo, CA). The sequence is DAEFRHDSGYEVHHQKLVFFADVGSNKG-AIIGLMVGGVV. Molecular mass and purity were confirmed by mass spectroscopy and reverse phase HPLC (MW = 4356, >95 % purity). Bovine serum albumin (BSA) was purchased from Fisher Scientific (Fairlawn, NJ). The IODO-beads, G-5 desalting columns, 1-ethyl-3-[3-dimethylaminopropyl]carbodimide hydrochloride (EDC), and sulfosuccinimydyl-3-(4-hydroxyphenyl) propionate (sulfo-SHPP) were purchased from Pierce Biotechnology, Inc. (Rockford, IL). The G-25 Sephadex were purchased from Amersham Biosciences/GE HealthCare (Piscataway, NJ.). Disialyllacto-N-tetraose (DSLNT) was purchased from V-labs, Inc. (Covington, LA). Sulfo-N-Hydroxy-Succinimido-Nanogold (sulfo-NHS-nanogold) and silver enhancing reagent were purchased from Nanoprobes (Yaphank, NY). All other materials and chemicals were purchased from Sigma-Aldrich Corporation (St. Louis, MO).

Gold Labeling and Silver Enhancement of Generation 4.0 PAMAM Dendrimer

The procedures for the attachment of sulfo-NHS-nanogold to primary amines on the dendrimer were performed according to the peptide labeling procedure provided by Nanoprobes without modification.[159] The silver enhancement was performed according to the silver enhancement of nanogold for EM procedure from Nanoprobes without modification.[159] These set of experiments were performed by Dr. James Henry in the lab

of Dr. Theresa Good at the Chemical and Biochemical Engineering department of the University of Maryland, Baltimore County (UMBC).

UV-Vis Absorption Spectroscopy Studies

500 μl of each the samples (1 = Au-Ag-dendrimer, 2 = Au-Ag-dendrimer-Aβ) were pipetted into a quartz cuvette respectively and their absorbance spectra were obtained by a Beckman DU 640 spectrophotometer. The ranges of wavelengths monitored were from 250 nm to 800 nm.

Collection of SERS Spectra

30 μl of each of the samples (sample 1 = Au-Ag-dendrimer, sample 2 = Au-Ag-dendrimer-Aβ) were pipetted onto the surface of a microscope glass cover slip (22×22 mm, Fischer Scientific Co.) and the water was allowed to evaporate for 30-45 min, until a thin solid crust of the sample remained on the surface of the cover slip. The cover slip was then placed onto the stage of the Leica *DMLM* microscope that was coupled to a Renishaw System 1000 Raman spectrometer. The laser used for the SERS studies was the 514.5 nm line of an Ar^+ laser (Spectra Physics Model 263C) with approximately 5 mW of laser power delivered to the sample. The laser beam was incident on the sample via the 50X air objective (NA =0.75) of the microscope. The SERS spectra were collected with the diffraction grating centered at 900 cm^{-1} and integration time of 90 sec.

Results and Discussion

UV-Vis Absorption Spectroscopy Studies

The UV-Vis absorption spectra of the samples (A = Au-Ag-dendrimer, B = Au-Ag-dendrimer-Aβ) are shown below in Figure 4.6. As can be seen in the figure, both the samples have an appreciable absorbance value at 514 nm with the dendrimer-amyloid sample having a more pronounced shoulder at this particular wavelength. This allowed the successful use of the Ar^{+} laser to excite the surface plasmon resonance of the large silver enhanced gold clusters for the SERS studies.

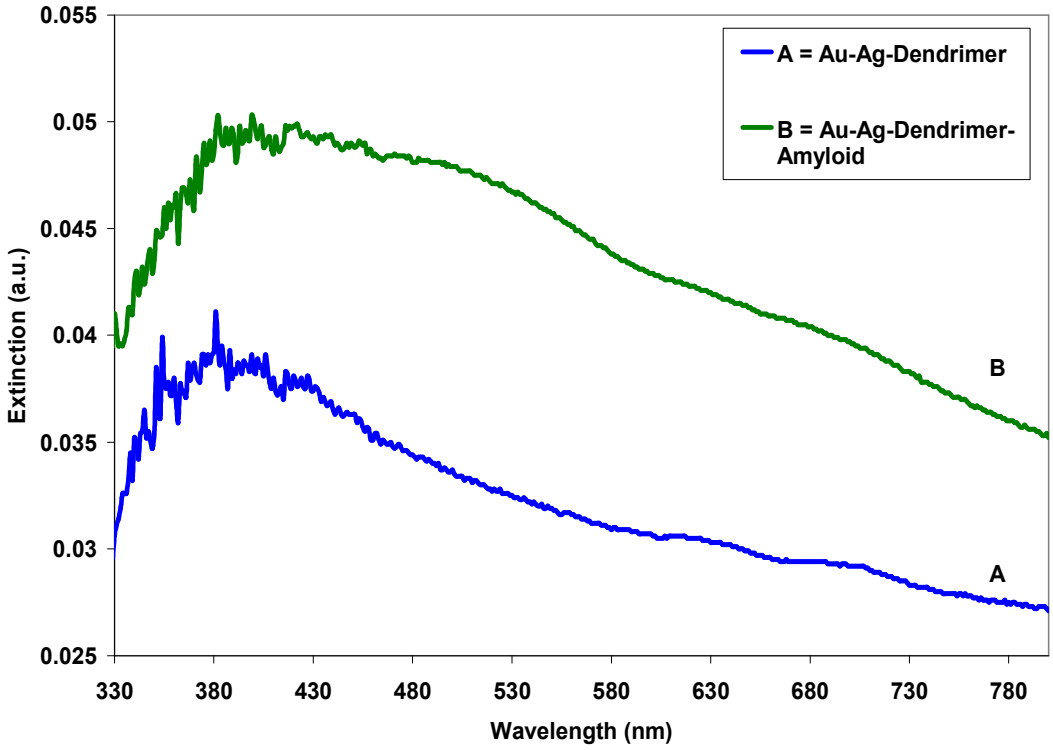

Figure 4.6: UV-Vis absorption spectra of Au-Ag-dendrimer (A) and Au-Ag-dendrimer –amyloid (B).

SERS Studies

The SERS spectra of the samples are provided below in Figure 4.7.

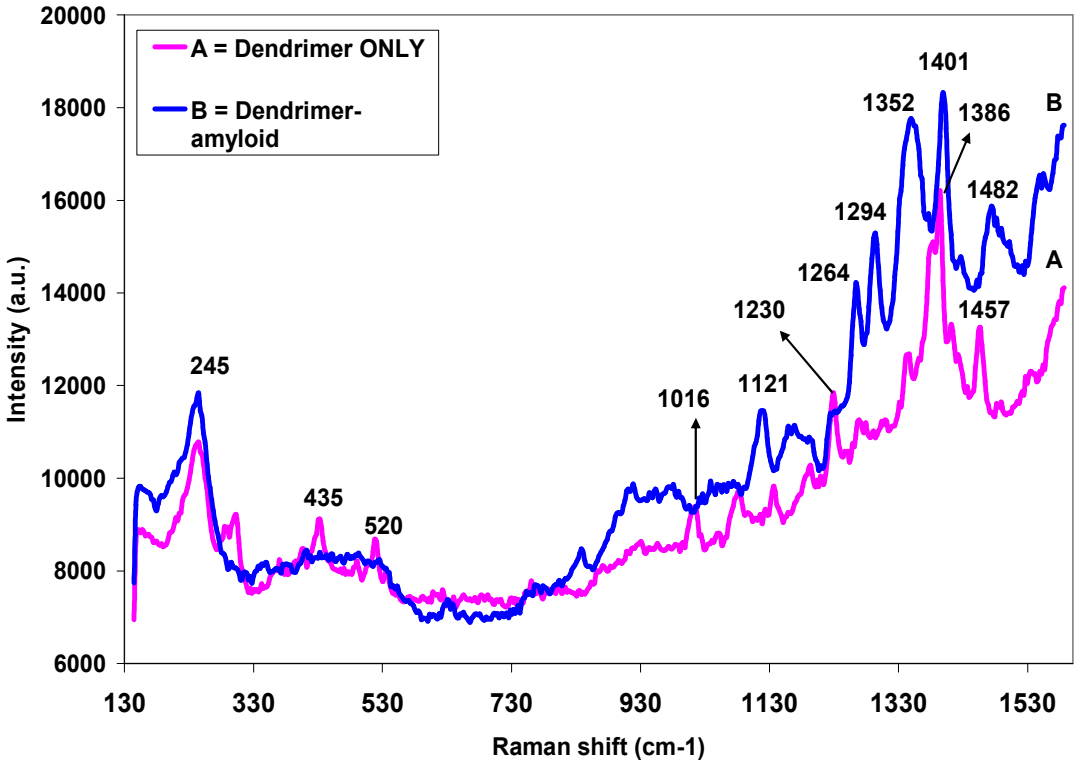

Figure 4.7: SERS spectra of Au-Ag-dendrimer only (A) and Au-Ag-dendrimer –amyloid (B).

A detailed search of the existing literature provided information that has been used to propose Raman band assignments to many of the peaks seen in the spectra in Figure 4.7. For the Au-Ag-dendrimer sample, the peak at 1230 cm^{-1} is indicative of the amide III band which consists of the C-N-H in plane bending and C-N stretching modes.[19] The peak at 1016 cm^{-1} is indicative of the C-C stretching band.[55] The peak 1457 cm^{-1} might indicate the CH_2 scissoring band and there is a slight possibility that the

peak at 1386 cm^{-1} might point to a CH_2 bending or twisting.[55] The source of the peaks at 435 cm^{-1} and 520 cm^{-1} are unknown.

The Au-Ag-dendrimer-Aβ sample shows some very distinctive protein SERS bands. The peak at 245 cm^{-1} is a result of the (Ag-N) interface vibration. This suggests that the sample attached to the Ag through the N atom (the same case also holds true for the peak at 245 cm^{-1} peak on the Au-Ag-dendrimer sample).[19] The peak at 1264 cm^{-1} is an amide III band that can represent either an α-helix or random coil structure.[18-19, 55] The peak at 1294 cm^{-1} is a distinctive amide III band from a β-turn and thus points to the presence of β-sheet structure in the sample.[18] The fact that this peak is large in magnitude indicates the presence of large amounts of β-sheet structures. The peak located at 1401 cm^{-1} results from the COO^- symmetric stretch of the acidic side chains (Asp and Glu).[160] The peak at 1121 cm^{-1} probably is a result of the C-N bond vibration of the backbone or from the side chains Val or Ile.[160] The 1352 cm^{-1} peak might arise form the C-H bend or C-C stretch and/or CH_2 twisting vibrations.[160] It is crucial to note here that the SERS spectra of the amyloid proteins only arises from the moieties that are in close contact with the Ag surface. It is well established that Aβ(1-42) fibrils have heavy β-sheet structures.[160] The presence of the amide III band at 1264 cm^{-1} that is in the range of either an α-helix or random coil structure only points to the fact that these structures were in close proximity to the Ag surface that is causing the SERS effect and does not indicate a predominance of that form in the Aβ(1-42) fibrils. These results indicate that the SERS spectra of Aβ-dendrimer is quite different from that of the spectra

of dendrimer. The presence of many extra peaks exclusive to Aβ indicates that dendrimers can indeed be used as biorecognition elements for the detection of Aβ using SERS.

Although this technique gave strong SERS spectra for both dendrimer and dendrimer-Aβ, it had one major limitation. This limitation was the lack of signal consistency obtained as the laser spot scanned though various areas of the thin film crust. There were only two spots (of 20 spots scanned) in the entire crust of approximately 7 mm diameter that showed strong SERS signals. It can be speculated that the two "good" spots were areas were the silver nanoparticles settled to form localized "hot spots" i.e. areas of strong plasmonic activity that lead to enhanced electromagnetc field enhancement. The formation of "hot spots" is a function of the shape and structure of the silver nanoparticle layer, the viscosity of the samples and control of experimental technique, parameters which are non trivial to control. This inconsistency of data although acceptable for qualitative proof of concept studies, would provide a major limitation for performing quantitative studies.

Development of a Gold Nanoshell Film Based SERS Sensor for β-amyloid Detection

Introduction

Based on the promising results of the feasibility studies of the last section, it was decided that the new biosensor using a sialic acid modified dendrimer as the biorecognition molecule would be implemented on a gold nanoshell film platform supplied by Nanospectra Biosciences Inc. (Houston, TX). It was thought that this would give the advantage of a robust SERS platform with well characterized optical properties and the added advantage of high optical tunability. The first step in developing such a biosensor involves the use of a Self-Assembled Monolayer (SAM) to attach the dendrimer to the gold surface. This is because gold alone does not bind well to the dendrimer and hence would compromise the robustness of the sensor. The monolayer used, had the following general form: HS-R-COOH, where R = $(CH_2)_2$, $(CH_2)_{11}$, or $(CH_2)_{16}$. It is the thiol group (-HS) that is critical for binding to the gold surface. The next step would be to attach the dendrimer to the SAM via EDC chemistry to form the final biorecognition element to capture the Aβ.

Materials and Methods

Materials

Most of the material used in this study were identical to those described previously except the gold nanoshell films which were supplied by Nanospectra Biosciences Inc. (Houston, TX).

Formation of Self-Assembled Monolayer (SAM)

The experiments involving the formation of the sensor chemistry were performed by Dr. Theresa Good and her student Dr. James Henry, at the Chemical and Biochemical Engineering department of the University of Maryland, Baltimore County (UMBC). All monolayers were formed using the same procedure. The monolayer material was dissolved in ethanol to form a 2mM solution. The slide was submerged in the monolayer (in ethanol) solution and allowed to react for 24 hours at room temperature. The slide was then removed from the solution and rinsed thoroughly with ethanol and dried under nitrogen. The monolayer materials used all had the following general form: HS-R-COOH, where R = $(CH_2)_2$, $(CH_2)_{11}$, or $(CH_2)_{16}$. Figure 4.8 depicts how the self-assembly occurs.[154] Fourier Transform Infrared Spectroscopy (FTIR) and SERS were used to confirm the assembly of the monolayer and the results are presented in the following section.

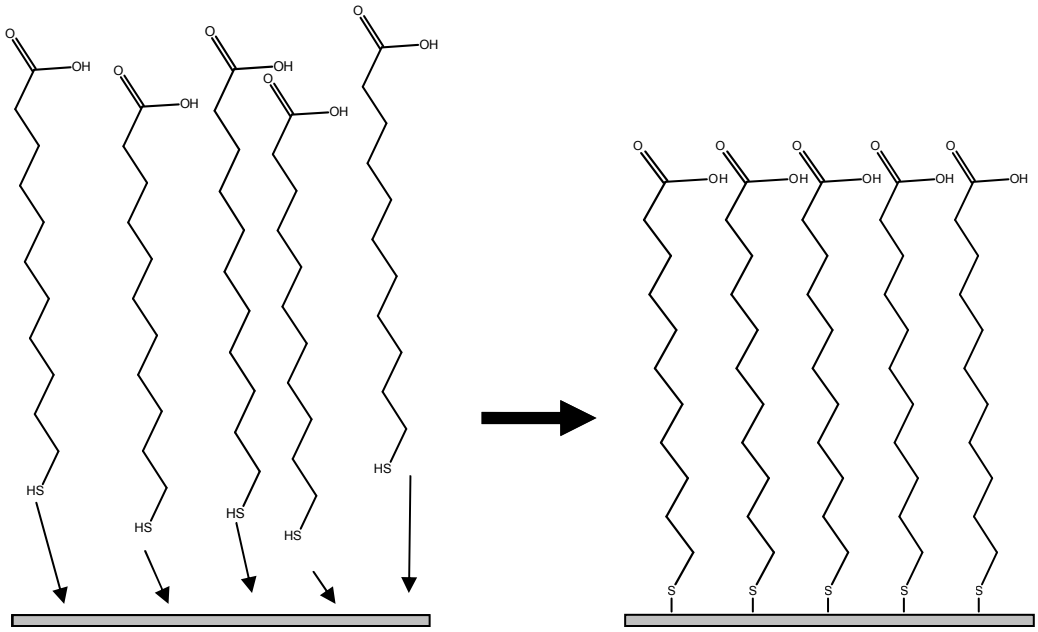

Figure 4.8: Schematic of the self-assembly process. The monolayer compound floats freely in solution until coming in contact with the metal surface (Ag, Au, or Ni usually). Upon contact, the thiol reacts with the surface, covalently binding the molecule to the surface. This layer is fluid in nature and will move around and continue to assemble until a tightly packed structure is formed. This creates the lowest energy state for the system and completes the self-assembly process.[154]

Stability of SAM Monolayer in Air Using a Fluorescein Marker

A fluorescein monolayer was developed by creating 11-MUDA monolayers as previously described on Au nanoshell surfaces. The fluorescein was attached using standard EDC chemistry. The basic technique of EDC chemistry will be described in greater detail in one of the later subsections as it is the same technique used to attach dendrimers on the SAM layer. Immediately after the fluorescein attachment, the slides were kept in nitrogen to prevent oxidation of the thiol group and detachment of the SAM layer. The samples were then tested using SERS immediately after removing the samples from nitrogen as well as in five consecutive days. The magnitude of 1186 cm^{-1} peak of

fluorescein was used to monitor the detachment of the SAM layer from the gold surface with time. The SERS spectra were collected between 1800 – 1000 cm^{-1} with a 60 sec integration time and using a 785 nm SDL High Powered Diode Laser delivering 1.60 mW power to the sample surface. The spectra were collected using the 50× air objective (NA = 0.75).

Effect of Distance from Surface on SERS Signal

The extent of the electromagnetic field (that is primarily responsible for the SERS phenomenon) from the surface of the Au is of critical importance in the design of the proposed biosensor. This was investigated by attaching aniline (a strong Raman active molecule) to the ends of three different monolayers of varying sizes (3-MPA, 11-MUDA, and 16-MHDA) using EDC chemistry and then using SERS to monitor the magnitude of the 1000 cm^{-1} aniline peak. The SERS spectra were collected using the 785 nm diode laser delivering approximately 2 mW at the sample. The spectra were collected between 1800 – 400 cm^{-1} with 60 sec integration time. The tests were performed with the 50× air objective (NA = 0.75).

Attachment of Dendrimer to Carboxy-Terminated Monolayer

The dendrimers were attached to the SAM terminated gold slide using EDC chemistry as described by Pierce Biotechnology [161] with minor modifications. These modifications were the concentrations used (since the surface concentration of monolayer could not be known). The 1-ethyl-3-[3-dimethylaminopropyl]carbodiimide hydrochloride (EDC) was added to the dendrimer solution (both having a concentration of 10 mg/mL) in a container containing the Au/SAM slide and the mixture was allowed

to react overnight. Upon completion, the slide was rinsed thoroughly with deionized water and dried under nitrogen for storage. Figure 4.9 shows the mechanism for EDC chemistry.[154] Figure 4.10 represents a cartoon of the gold surface that is expected with successful attachment of both the SAM layer and the dendrimer.[154] The results of the FTIR analysis used to ascertain the presence of the dendrimer on the surface of the SAM and gold nanoshell is shown in the next section.

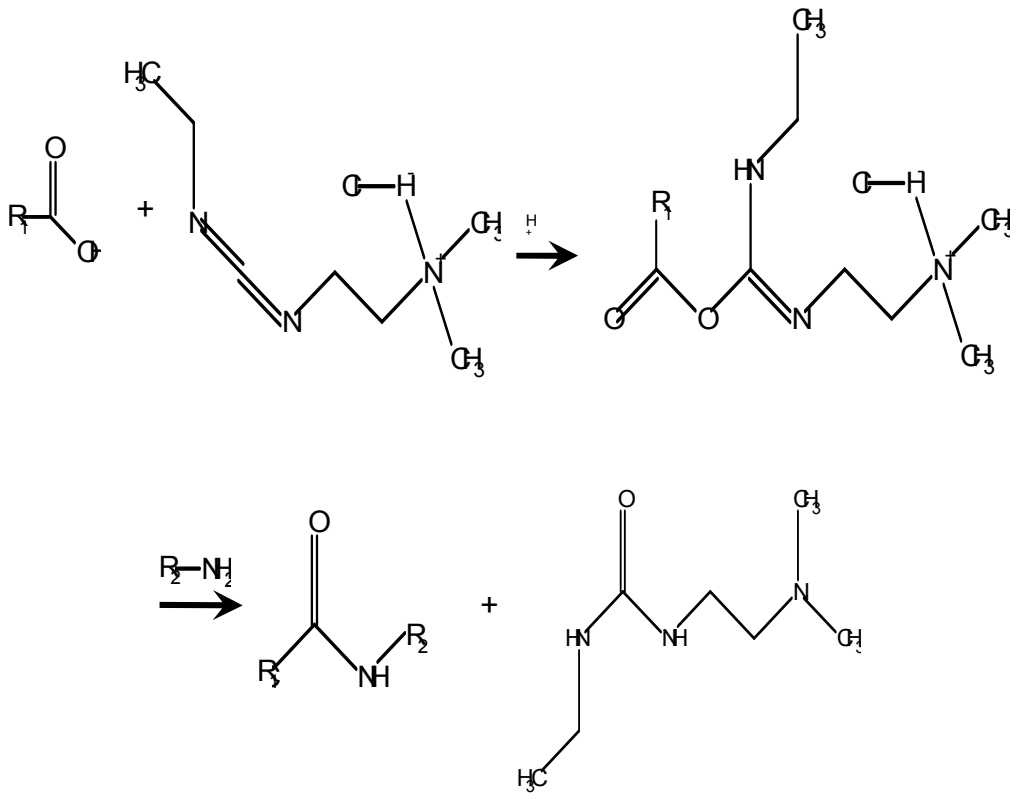

Figure 4.9: Schematic of EDC chemistry. The carboxylic acid-terminated compound reacts with EDC to form an amine-reactive intermediate. This intermediate then reacts with the amine-terminated compound to create an amide bond leaving only the spent EDC.[154]

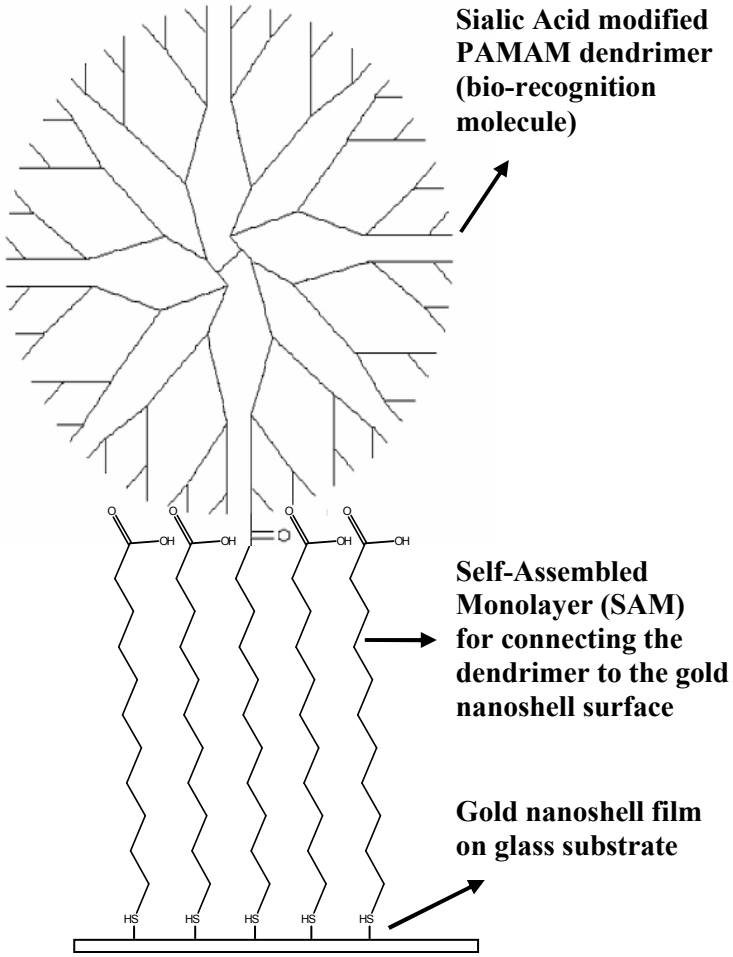

Figure 4.10: Schematic of the dendrimer surface. The figure depicts a generation 4.0 amine-terminated dendrimer attached to a carboxylic acid terminated surface (11-MUDA) via EDC chemistry. This leads to the formation of amide bonds.[154]

Results and Discussion

Formation of Self-Assembled Monolayer (SAM)

The FTIR spectrum shown in Figure 4.11(A) is the result of growth of the 11 carbon (11-MUDA) self-assembly onto the surface of the gold nanosehell layer.[154] The results show the characteristic 1700 cm^{-1} carboxylic acid peak (COOH) of 11-MUDA

along with the doublet at 2849 cm^{-1} 2917 cm^{-1} that are due to the CH_2 group of 11-MUDA. This spectrum proves successful assembly of 11-MUDA on the gold nanoshell surface. Figure 4.11(B) demonstrates the SERS spectrum of 11-MUDA on Au nanoshell film. The spectra shows a large peak at 1085 cm^{-1} which is representative of the C-C bonds present in 11-MUDA and the peak at 1177 cm^{-1} is representative of a C-H bending stretch.[162] These figures help conclude that the self-assembly process of 11-MUDA on gold nanoshell surface was indeed successful.

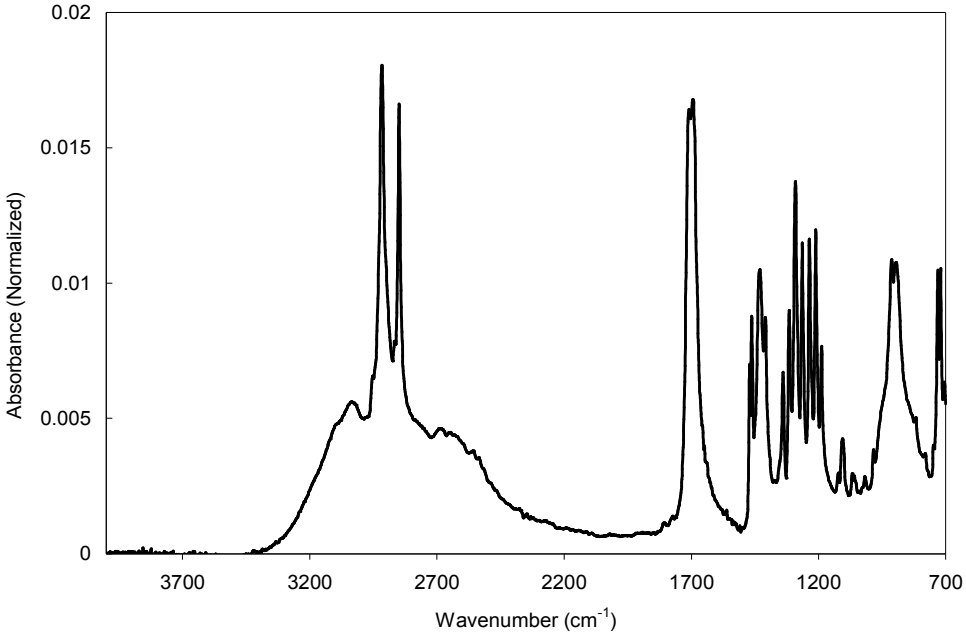

Figure 4.11(A): FTIR spectrum of 11-MUDA SAM on the Au nanoshell surface.[154]

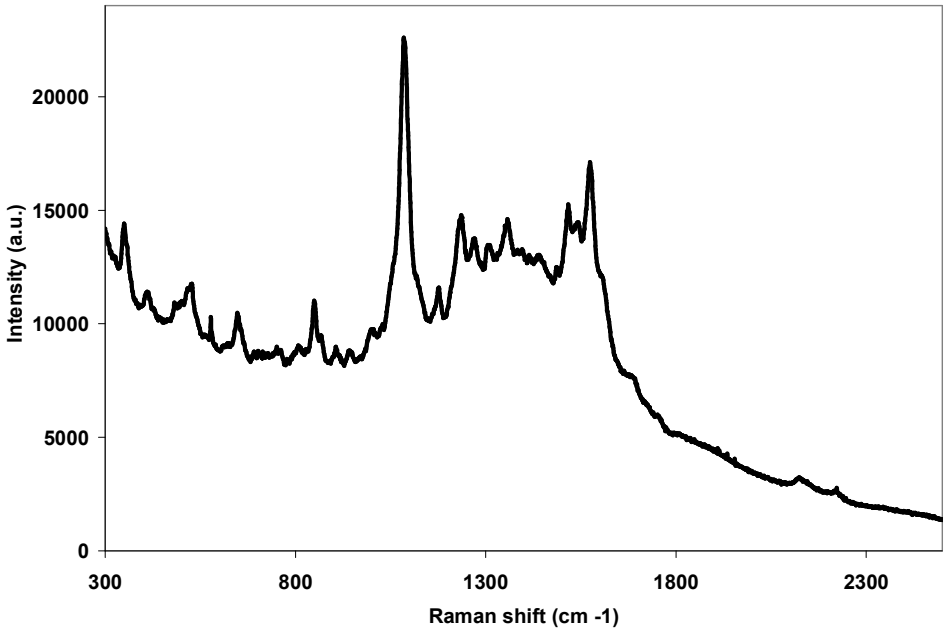

Figure 4.11(B): SERS spectrum of 11-MUDA SAM on the Au nanoshell surface.

Stability of SAM in Air Using a Fluorescein Marker

The results of SAM aging study was monitored using SERS and are presented in Figures 4.12(A) and 4.12(B). Figure 4.12(A) shows the SERS spectrum of fluorescein on 11-MUDA after subtraction of the 11-MUDA spectrum. The figure distinctly shows the strong 1185 cm^{-1} SERS peak of fluorescein which was used to monitor the stability of the SAM layer with increased exposure in air. Recent studies indicate that the monolayers used in these experiments are unstable in the presence of oxygen.[163] This is due to the reaction of oxygen with sulfur at the metal surface (the sulfur is part of the original thiol group on the SAM's). This causes the formation of sulfates thus breaking the bond holding the SAM to the gold surface.

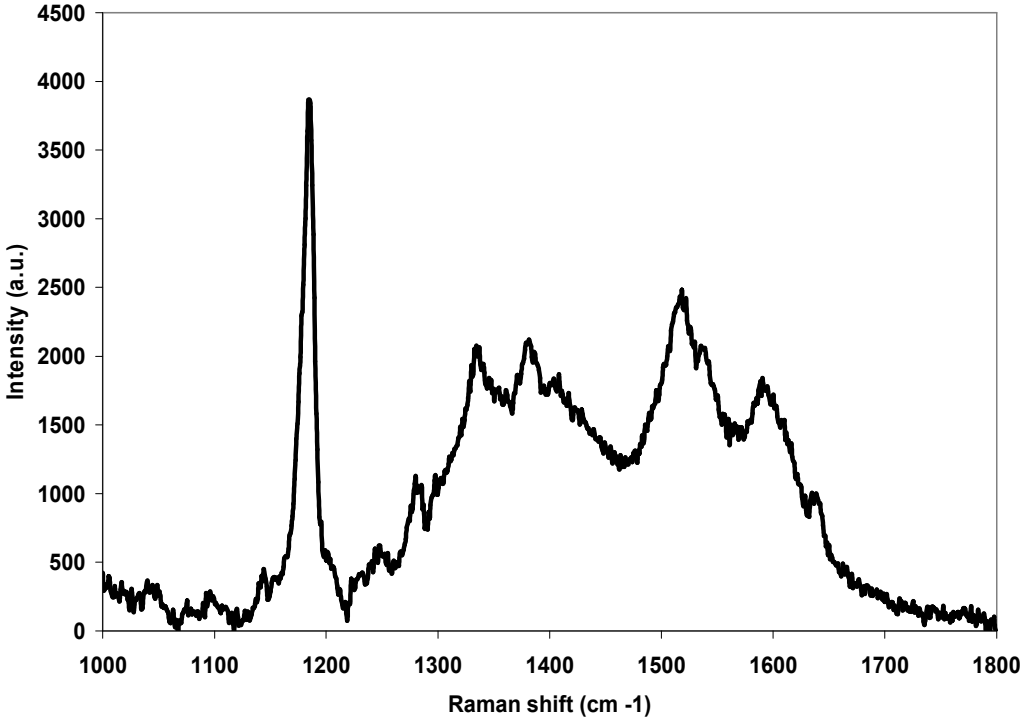

Figure 4.12(A): SERS spectrum of fluorescein on 11-MUDA on the Au nanoshell slide.

The aging study was carried out by exposing the sample in air for the required amount of time, rinsing off the sample surface with copious amount of deionized water in order to remove all the SAM molecules that had undergone oxidation and detached themselves from the gold surface, and then allowing it to dry before obtaining SERS spectra from its surface as described previously. Figure 4.12(B) shows the intensity of the 1185 cm^{-1} fluorescein SERS peak averaged for 32 different spots on the sample surface for each exposure event. The error bars represent the standard error in the data collected. The data clearly shows a decay in the fluorescein signal over time. The

maximum decrease in signal appears to occur somewhere between 24 to 48 hours after exposure to air after which this decay process appears to reach equilibrium.

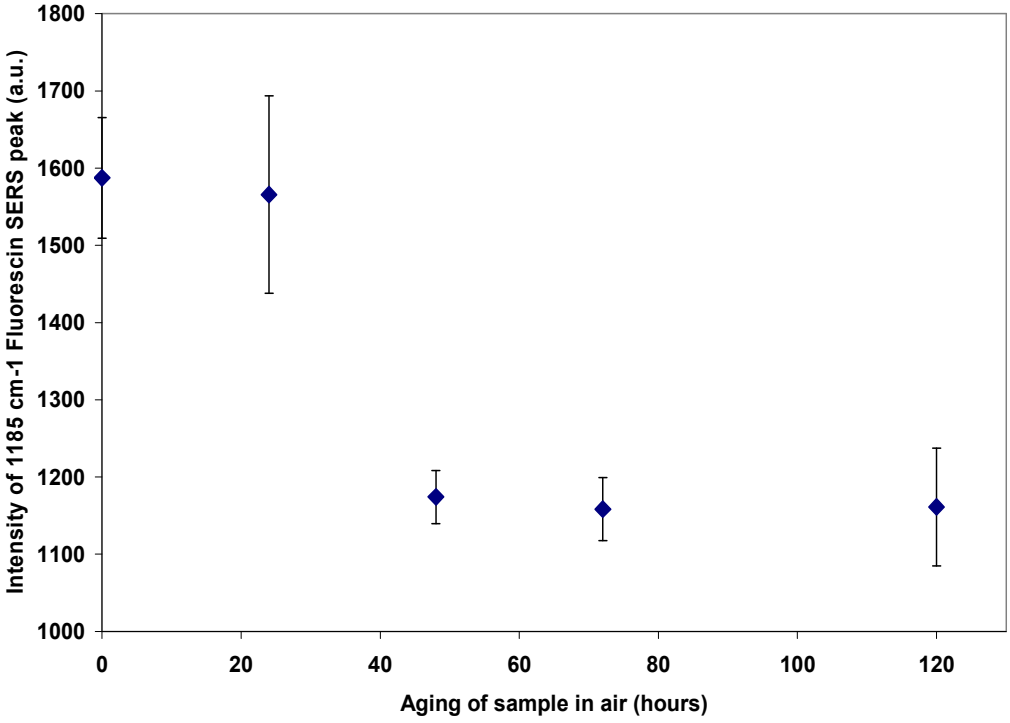

Figure 4.12(B): Intensity decay of the 1185 cm^{-1} fluorescein SERS peak with aging the sample in air.

Effect of Distance from Surface on SERS Signal

The extent of the electromagnetic field (that is primarily responsible for the SERS phenomenon) from the surface of the Au is of critical importance in the design of the proposed biosensor. The current design of the biosensor involves the SAM layer bound directly to the Au surface followed by the dendrimer layer. It is expected that any

Aβ captured by the sensor on the successful completion of an assay will end up in contact with the dendrimer layer. Therefore the distance between the captured Aβ and the Au surface which is responsible for generating the SERS signal is critical to the sensor sensitivity. This was investigated by attaching aniline (a strong Raman active molecule) to the ends of three different monolayers of varying sizes (3-MPA, 11-MUDA, and 16-MHDA) using EDC chemistry and then using SERS to monitor the magnitude of the 1000 cm^{-1} aniline peak. The results of the study is presented in Figure 4.13 where each point represents the average of five spots on each sample and the error bars represent the standard error in the data. The figure shows a monotonic decay in the magnitude of the 1000 cm^{-1} aniline peak with increasing chain length of the spacer layer. Figure 4.13 shows that the aniline still provides an appreciable signal when separated by a distance of approximately 2.1 nm from the gold surface. This distance is approximately in the range of the size of a Gen 2 PAMAM dendrimer (2.9 nm).[164] These tests show promising results that a Gen 2 PAMAM dendrimer when attached to the gold surface by a small SAM layer (such as 3-MPA) could provide the necessary sensitivity for detection of a captured Aβ using the current biosensor design.

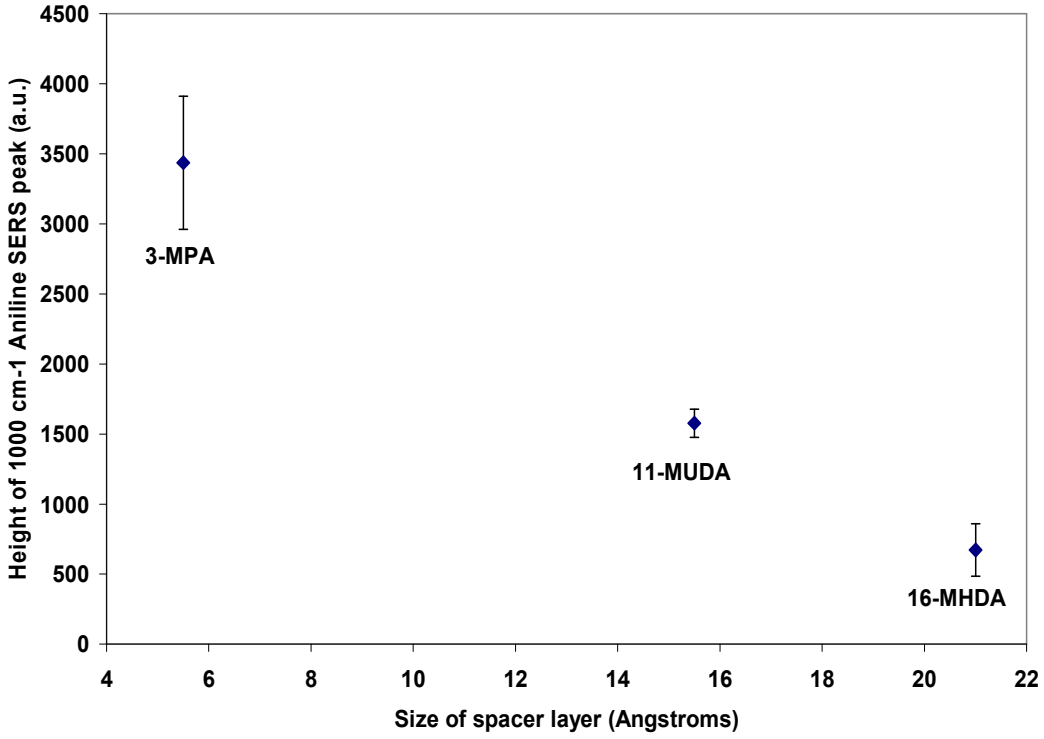

Figure 4.13: Variation in the intensity of the 1000 cm^{-1} SERS peak of aniline when attached via varied chain length alkanethiol SAM's to the Au nanoshell surface.

Attachment of Dendrimer to Carboxy-Terminated Monolayer

Figure 4.14 shows the results of FTIR analysis on a slide with 11-MUDA SAM layer before and after attachment of Gen 4 PAMAM dendrimer using EDC chemistry.[154] The thick solid line is the FTIR scan of 11-MUDA only and the thin dashed line is the FTIR scan obtained after dendrimer attachment to the 11-MUDA. It appears that the strong dendrimer spectrum obscures features that might result from the formation of an amide bond between the SAM layer and the dendrimer. This is because the dendrimer molecule itself has many secondary amide bonds within it. There is however a decay in the 1700 cm^{-1} carboxylic acid peak (COOH) in the spectra of dendrimer attached to 11-

MUDA indicating a loss of carboxylic acids groups. This can be attributed to the formation of amide linkages via the COOH group of 11-MUDA and the terminal NH_2 groups of the dendrimer.

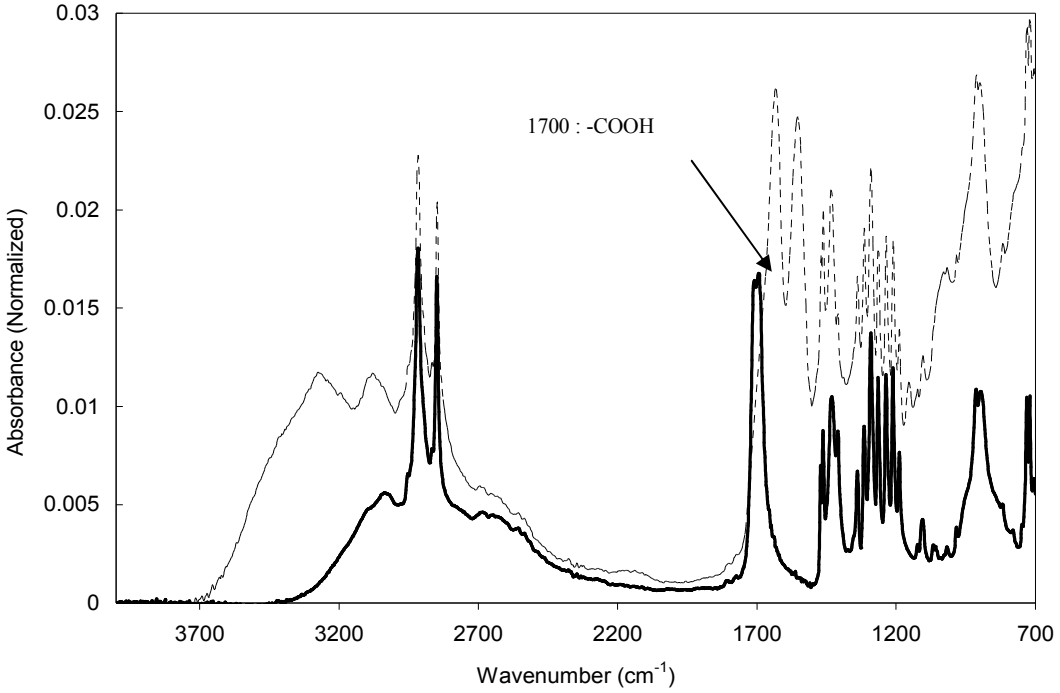

Figure 4.14: FTIR spectra of 11-MUDA (thick, solid line) and 11-MUDA/Den 4.0 (thin, dashed line) on the Au surface.[154]

CHAPTER V

SERS FOR THE DETECTION OF INTRACELLULAR CONSTITUENTS USING GOLD NANOSHELLS AND COLLOIDAL GOLD NANOPARTICLES

Introduction

Biological systems such as cells are extremely complex environments where a myriad of organelles and molecules are involved in a complex hierarchical ordered network of interactions in order to maintain viable living conditions. Thus a key to unraveling the mysteries of cellular functionality involves the chemical detection of both cellular components as well as the products of the various cellular biochemical processes. This understanding of cellular functionality would be critical for the development of more efficient medical care. Although current methods of cell component detection such as fluorescence based confocal and multiphoton microscopy allow the detection of many cell components, the need to label these components with exogenous fluorophores which can photobleach is a complication which limits the sensitivity of such methods. [165] Other Raman microscopy based methods used to study microbial cells resulted in weak Raman spectra of the cells and required the use of complex multivariate statistical analytical techniques such as principal component analysis (PCA), discriminate functional analysis (DFA), hierarchical cluster analysis (HCA), constrained principal factor analysis and other peak fitting algorithms to analyze the complex spectra.[162, 166-167] Another disadvantage of using regular Raman spectroscopic methods for analyzing cells

is the need of high incident laser power delivered to the sample (typically in the range of hundreds of milliwatts) which leads to the problems of sample composition change or complete sample damage due to local heating effects.[162,166,168] This is because Raman scattering is an inefficient process.[1] Surface Enhanced Raman spectroscopy (SERS) is a technique developed more recently which has been used successfully to enhance the Raman signal of a molecule by factors of 10^6 or more.[2-7] Hence the signal enhancement properties of SERS can potentially be exploited in cellular biosensing. SERS studies have previously been carried out using cells, but these have either used thin films of noble metals or noble metal nanoparticles.[32-34] The studies of Abrahamson *et al*. and Feld *et al* successfully demonstrated that gold nanoparticles can be introduced into lymphocytes and endothelial cells respectively without detrimental toxicological effects and that some of the nanoparticles can form *in situ* aggregates which have plasmonic activity suitable for collecting SERS spectra. Since this aggregation is an uncontrolled process, not all nanoparticles in a cell form Raman active aggregates and the surface plasmon resonance wavelength at which these aggregates are excited, is not tunable. Another major disadvantage in using a colloidal aggregation based SERS surface is the lack of reproducibility in the data.[32-34] This is because the colloidal aggregation takes place inside the cells due to high salt and other analyte concentration. This aggregation process is inherently uncontrollable and hence compromises the robustness of such a detection technique.

This study aims to overcome the disadvantages of colloidal aggregation based SERS detection of intracellular constituents via the use of novel gold nanoshells.

Nanoshells are a unique class of metal nanostructures that consist of a dielectric core surrounded by a thin noble metal shell. Typically the core consists of silica and gold and silver have been used to form the outer shell layer.[112-113,115-116] Nanoshells are unique as their plasmon resonance wavelength is tunable from the visible though the near-infrared region of the electromagnetic spectrum and the strength of the electromagnetic field on the metal nanoshell surface is also controllable. This is achieved by varying the ratio of the dielectric core to the thickness of the outer metallic shell layer.[112-113,115-116,118] This tunability of their plasmon resonance makes nanoshells extremely useful for use as SERS substrates for intracellular component detection. This is because they can be tuned to match the wavelength of any incident laser (as long as it lies in the visible through the infrared region of the spectrum). This has two advantages namely, maximizing the electromagnetic SERS enhancement by tuning the nanoshells to the incident laser wavelength and overcoming the aggregation problem since each individual nanoshell is tuned to the laser wavelength thus negating the need for any aggregation of these particles. Nanoshells have previously been used to achieve SERS enhancements of up to 10^{12} when measuring spectra from organic molecules.[123,128] Since they do not require aggregation in order to form SERS active particles (in contrast to metal colloids) they serve as attractive agents to probe the local chemical environment within a cell. Although gold nanoshells have been targeted for use in thermal therapy to kill tumor cells, no attempt was made to place the nanoshells inside the cells. Instead the nanoshells reached the tumor through its vasculature, and cell-surface interactions along with local heating effects created by the incident laser was used to kill the tumor.[169]

This study reports the successful introduction of gold nanoshells into mouse fibroblast cells through fluid phase uptake (pinocytosis) without inducing cell death during a 24 hour incubation period. The results obtained demonstrate that nanoshells can act as a suitable SERS substrate with which to detect intracellular components throughout a cell. Without nanoshells, no Raman scattering was observed in the experimental conditions. By traversing the laser spot through a cell, a variety of SERS signals were obtained which can be ascribed to different cellular components. Finally this study also performs a second set of identical experiments with classical colloidal gold nanoparticles and compares the two sets of results to demonstrate that gold nanoshells can provide comparable sensitivity to colloidal gold nanoparticles for the detection of intracellular cellular constituents while having the advantage of having highly tunable plasmonic properties thus circumventing the need for aggregation.

Materials and Methods

Materials

The gold nanoshells used were fabricated by Nanospectra Biosciences, Inc. (Houston, TX) and had a 125 nm silica core and a 11 – 14 nm gold shell thickness. The nanoshells were optimized to have an extinction peak at approximately 810 nm in water. The gold nanoshells had an initial concentration of approximately 4×10^9 particles per ml. 60 nm colloidal gold particles were obtained from Polysciences Inc. (Warrington, PA). Adenine powder was purchased from Sigma-Aldrich (St. Louis, MO). All culture

flasks, centrifuge tubes, serological pipettes and transfer pipettes used for cell culture were purchased from VWR International (West Chester, PA).

Cell Culture

Mouse NIH/3T3 (ATCC, Manassas, VA) cells were incubated at 37 $^{\circ}$C in 5% CO_2 and 95% humidified air in Dulbecco's Modified Eagle's Medium (DMEM, Gibco, St. Louis, MO) supplemented with 4 mM L-glutamine, 4.5 g/L glucose, 1.5 g/L sodium bicarbonate, 10% bovine calf serum (BCS, Gibco), and 100 U/ml penicillin, 100 mg/ml streptomycin (Sigma, St. Louis, MO). For SERS studies, cells were grown to confluence in a T25 tissue culture flask. The cells were detached by addition of 0.25% (w/v) trypsin/0.13% (w/v) EDTA (Sigma, St. Louis, MO) solution followed by incubation at 37°C for 3 minutes. The flask was agitated to dislodge all cells and the suspension pipetted to a centrifuge tube, a further 3 ml of growth medium was then added to the tube in order to quench the trypsin activity. The cells were spun at 1600 rpm for 6 minutes, the supernatant removed and then resuspended in 5 ml of growth medium. The suspension was pipetted onto two cover slips (38 x 26 mm^2) in the bottom of separate petri dishes (2.5 ml each). These cells were incubated at 37°C for 2.5 hours and their adhesion to the cover slip checked using phase contrast microscopy. A suspension of gold nanoshells in growth medium was then added (2.5 ml) at a concentration of 3000 nanoshells per cell. The control sample received only 2.5 ml of growth medium. The cells were incubated for 20 hours in order to allow uptake of nanoshells and the cover slips checked intermittently for cell adhesion and general cell health using phase contrast

microscopy. The medium was then removed from the petri-dishes, the monolayers washed twice with phosphate buffered saline (PBS) and buffered formalin added for 15 minutes to fix the cells. Fixation in buffered formalin was used since this method has previously been found to maintain Raman features as well as cell morphology. The cells were then washed a further four times in deionized water to remove excess fixative and allowed to dry before being used. These steps were then repeated for a second set of experiments using colloidal gold nanoparticles.

SERS Microscopy

All SERS Raman spectra were collected using a Renishaw System 1000 Raman Spectrometer coupled to a Leica DMLM microscope. The laser used was a 785 nm (SDL-8530 Wavelength Stabilized) High Power Laser delivering approximately 2.0 mW to the sample. A 50 × air objective (NA = 0.75) was used to focus the laser on discrete areas within the cell. The SERS spectra presented were collected between 500 cm^{-1} and 1800 cm^{-1} (relative to laser wavelength) with a 120 sec integration time. The final spectra presented in the following section are SERS spectra of the Au nanoshell and Au colloid incubated cells with the silica fluorescent background subtracted, upon which a baseline correction routine was performed. The baseline correction routine used was a GRAMS/32 based routine (ThermoGalactic) which was a built-in feature of the WiRE™ software (version 1.2) that controlled the Raman spectrometer. Raman spectra from fibroblasts which had not been incubated with either nanoshells or colloidal gold were collected in an identical manner and none of these spectra showed any Raman features.

Transmission Electron Microscopy (TEM)

Cell cultures treated with gold nanoshells were fixed for 1 hr in 2.5% (vol/vol) glutaraldehyde in DMEM at 37° C. The cultures were then washed three times with DMEM, followed by post fixation overnight at 4° C with 1% (wt/vol) osmium tetroxide in DMEM. The cultures were washed with DMEM, then dehydrated with methanol (20% steps: 20-100%) and infiltrated and embedded in epoxy resin.

Ultra thin sections were taken parallel to the bottom of the culture dish using a diamond knife. The sections were placed on grids and post stained with 2% aqueous uranyl acetate followed by Reynolds lead citrate.[170] The grids were examined and photographed at an accelerating voltage of 100kV in a JEOL 1200EX transmission electron microscope at the Microscopy and Imaging Center at Texas A&M University.

Results and Discussion

Nanoshells were introduced into the fibroblast cells by "cellular drinking" (pinocytosis). Pinocytosis is a process by which cells uptake nutrients through the formation of an invagination at the plasma membrane.[171] Pinocytosis is generally limited to particles less than 150 nm in diameter and so should allow cellular uptake of single individual nanoshells. It is believed that aggregated nanoshell complexes would be too large in size to enter cells via pinocytosis. Figure 5.1 shows the extinction spectra of gold nanoshells in deionized water (A), DMEM in deionized water (B) and gold nanoshells in DMEM (C) in conditions that were identical to those when incubating the cells. This is presented to ascertain the aggregation state of the gold nanoshells during

incubation of the cells. As observed from the figure, there is only a slight 12 nm red shift of the plasmon resonance peak of the Au nanoshells from water to DMEM (λ_{max}(water) = 814 nm; λ_{max}(DMEM) = 826 nm). This level of red shift of the plasmon resonance peak along with a slight decrease in its magnitude is in agreement with previously documented behavior of the surface plasmon waves of noble-metal nanoparticles in complex biological media of higher refractive index than water and does not indicate aggregation of the nanoshells in DMEM growth medium.[172] As mentioned in the materials section of the paper, DMEM growth medium has a high salt content, and contains antibiotics, glutamine, phenol red (pH indicator) and calf serum and thus has a higher refractive index than water.

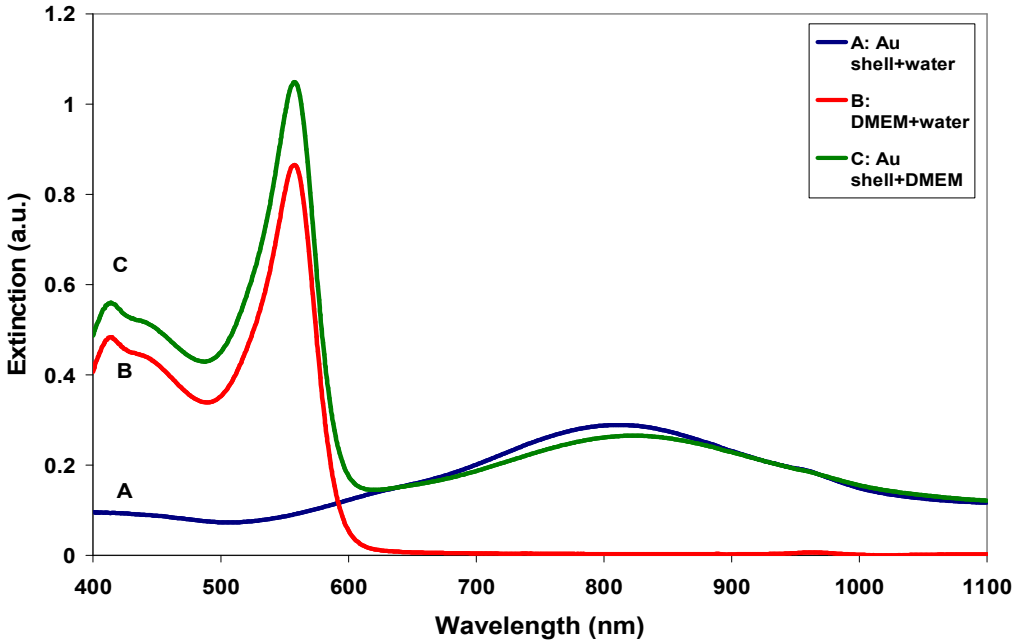

Figure 5.1: Extinction spectra of Au nanoshells in water (A), DMEM in water (B) and Au nanoshells in DMEM (C).

TEM analysis was done on a second set of fibroblast cells which were treated under the same conditions as those used for the SERS studies in order to ascertain that the nanoshells actually entered the cells and were not just attached only to the cells surface. The results of the TEM study are presented in Figure 5.2. The top right image in Figure 5.2 shows three fibroblasts containing a number of Au nanoshells. The nanoshells can be seen in a variety of locations: adjacent to the nucleus, mitochondria and also in vesicles merging with the cell cytoplasm. In some of these locations, the nanoshells have formed small aggregates. This is the result of the complex biological conditions within the cell and the nature of cells to group together particles that enter it via endocytotic vesicles. Hence a certain degree of aggregation is unavoidable. However, there are several instances where single nanoshells can be seen. It is believed that these aggregates formed only after cellular ingress of individual nanoshells *via* pinocytosis since the collective diameter of any aggregated nanoshell complex would be over 200 nm. This size would not be conducive to pinocytosis and so any aggregated complexes would be unable to enter cells. The top left image in Figure 5.2 shows two small groups of nanoshells in a vesicle adjacent to the cell nucleus (seen in the left of the image). The bottom right image in Figure 5.2 shows a group of four nanoshells emerging from a vesicle adjacent to a mitochondrion. The bottom left image in Figure 5.2 shows a small group of three nanoshells along with two single ones in a vesicle adjacent to a mitochondrion. The contrast of this image has been adjusted so that the core/shell structure of the nanoshells can be clearly seen. The silica dielectric core being less

electron dense than the gold shell layer appears lighter in the TEM image when compared to the outer gold shell layer.

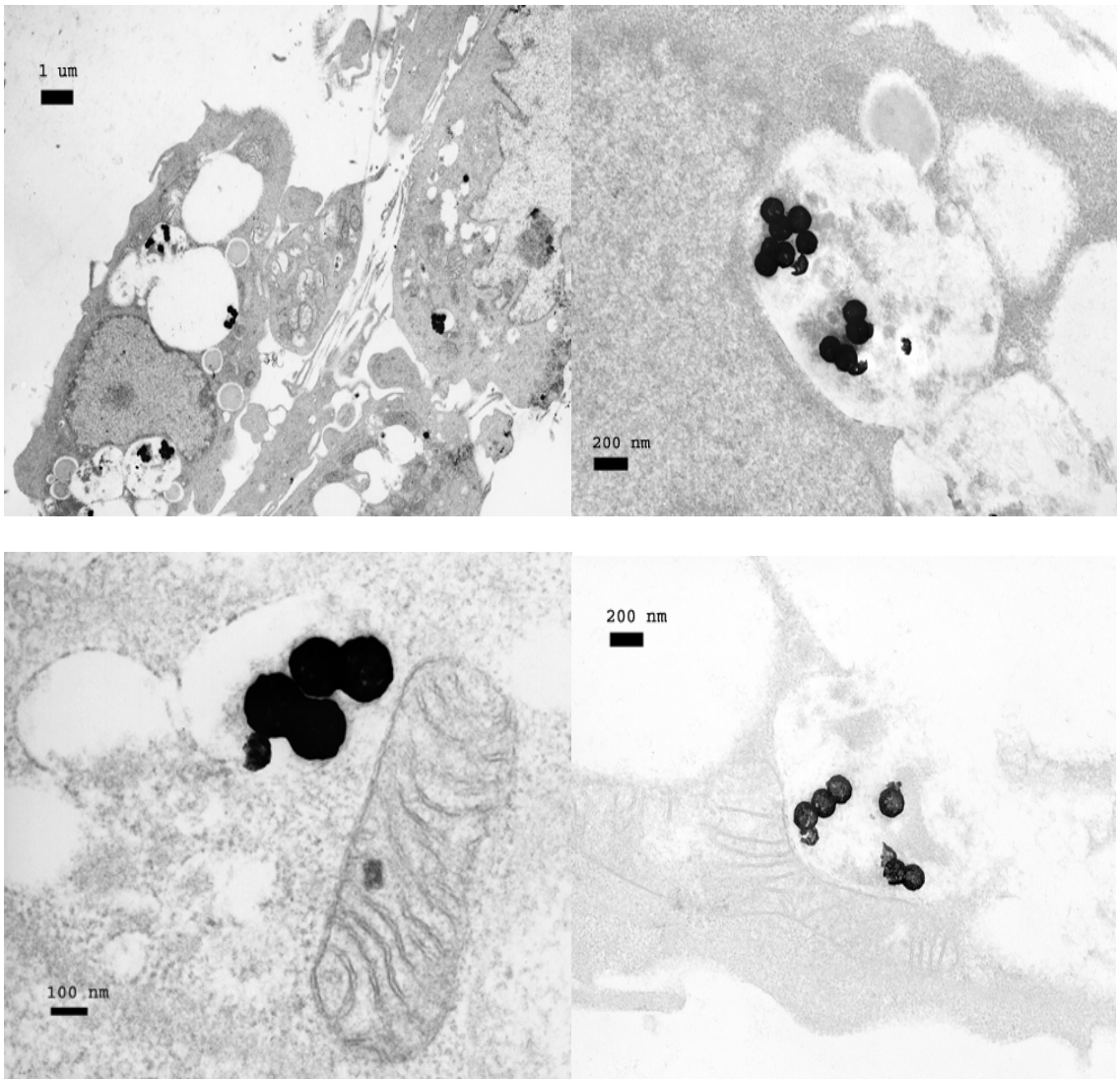

Figure 5.2: TEM images of fibroblast cells incubated with Au nanoshells.

The successful introduction of gold nanoshells into the fibroblast cells allowed their use in probing the complex intracellular environment using SERS. Figure 5.3(A) shows spatially resolved SERS spectra (spectra *a* – *d*) obtained at various locations within a fibroblast cell. The approximate locations in the fibroblast where the SERS spectra were collected are depicted in the corresponding brightfield image in Figure 5.3(B). In Figure 5.3(A), the 673 cm^{-1} peak is the major peak in spectrum *a* and can originate from the in plane ring vibration of the nucleic acid constituents thymine and/or guanine.[167] This might imply that location *a* might be inside or around the nucleus or in proximity to ribosomes. Spectrum *b* on the other hand has several major SERS peaks. The peak located at 880 cm^{-1} can either originate from a C-C-N^+ symmetric stretch or a C-O-C ring vibration.[173-174] The 1000 cm^{-1} peak lies in the typical region of a symmetric ring breathing mode of phenylalanine.[167,174] The 1117 cm^{-1} can originate from a DNA/RNA O-P-O stretch.[173] The large 1254 cm^{-1} peak lies in the classic protein amide III stretching region.[18,162,167,174] The wide peak between 1300 – 1500 cm^{-1} probably results from the sum of several closely located peaks. Although specific individual peaks are not recognizable without the application of complex peak fitting algorithms, this region is typical of CH deformation bands, CH_3 deformation and DNA/RNA in plane ring vibrations.[162,167,174] Thus the presence of such protein and nucleic acid SERS bands in spectra *b* implies that this location would be expected to be in or near a nucleus of the cell or possibly even the endoplasmic reticulum. The spectrum from location *c* was collected with the laser spot focused approximately 2 μm to the right of location *b*. Spectrum *c* has several peaks in similar locations to that of spectrum *b* such as 1286 cm^{-1}

(amide III), 1105 cm^{-1} (PO2 stretch), 1002 cm^{-1} (phenylalanine), 877 cm^{-1}(C-C-CN+ or C-O-C).[18,162,167,173-174] In addition, spectrum *c* has several major peaks which are different from spectrum *b* such as the 1588 cm^{-1} adenine/guanine vibration band, the 1388 cm^{-1} DNA in plane ring vibration band, the 1338 cm^{-1} pyrole ring vibration band, and the 831 cm^{-1} DNA backbone O-P-O stretching band which also overlaps with a tyrosine in plane ring vibration band.[18,162,167,174] The SERS peaks in spectrum *c* suggests a mixture of nucleic acids and proteins and thus indicates that the gold nanoshells responsible for generating this spectra were either inside or in close proximity to a nucleus. This also indicates that there are different groups of nanoshells present in various areas inside the cell which are probing a wide variety of molecules. The TEM images in Figure 5.2 also corroborate this. Spectrum *d* from Figure 5.3(A) was obtained by moving the laser spot approximately 3 μm directly in front of location *c* and shows several interesting SERS peaks. The small peak at 654 cm^{-1} probably originates from C-C twist of tyrosine, the strong 850 cm^{-1} SERS peak is possibly a tyrosine ring breathing peak, the 890 cm^{-1} peak is a possible DNA backbone stretch, the peak at 988 cm^{-1} possibly originates from C=H bends of lipids and the 1556 cm^{-1} probably is a C=C stretch from lipids. [162,167,173,174] This mixture of SERS peaks from proteins, nucleic acids and lipids indicate that location *d* might lie in very close proximity to the nuclear membrane.

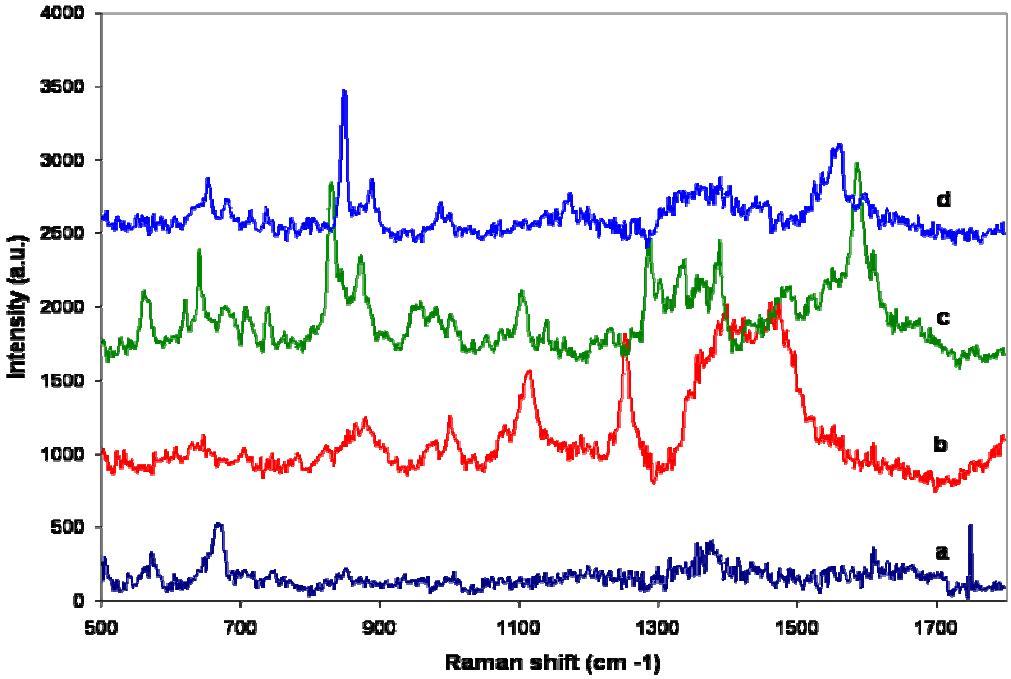

Figure 5.3(A): SERS spectra of fibroblast cell 1 incubated with Au nanoshells.

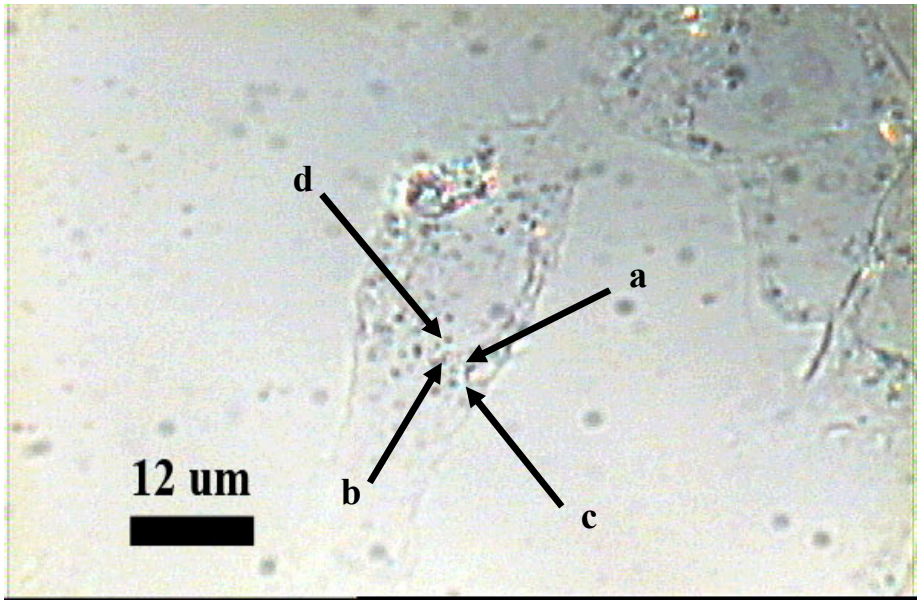

Figure 5.3(B): Brightfield image of fibroblast cell 1 incubated with Au nanoshells showing approximate locations where SERS spectra were collected.

A new set of SERS spectra collected from a second fibroblast cell incubated with gold nanoshells is shown in Figure 5.4(A). Similar to Figure 5.3, the approximate locations in the fibroblast cell where the SERS spectra were collected are depicted in the corresponding brightfield image in Figure 5.4(B). Spectra form locations *a* – *c* show major SERS peaks in regions typical for proteins (the 626 cm^{-1} C-C twist of phenylalanine, 1089 cm^{-1} C-N protein backbone stretching band, 1261 cm^{-1} amide III stretching band, 1366 cm^{-1} porphyrin vibration band, 1415 cm^{-1} COOH vibration band, 1448 cm^{-1} CH deformation band, 1523 cm^{-1} amide II stretching band and the 1596 cm^{-1} aromatic amino acid band) [18-19,162,167, 173-175] and nucleic acids (832 cm^{-1} O-P-O stretch band, the 1089 cm^{-1} phosphodioxy group PO_2 vibration, and the 1484 cm^{-1} guanine/adenine in plane ring vibration band).[18-19,162,167, 173-175] The peaks present suggest that the location of these spectra contain a metalloprotein such as a cytochrome. This indicates that the laser spot might be around mitochondria. The split and movement of the 1366 cm^{-1} peak to 1378 cm^{-1} (from spectra *a* to *c*) suggest that over the course of three scans in close proximity two different oxidation states of the protein were being imaged.[176,177] Traversing the laser through the cell, location *d* reveals an interesting combination of major SERS peaks. They are the 1006 cm^{-1} phenylalanine ring vibration, 1129 cm^{-1} C-N protein backbone stretch/C-C lipid stretch, 1240 cm^{-1} amide III protein

band, 1376 cm^{-1} porphyrin vibration, and the 1549 cm^{-1} lipid band.[18-19,162,167,173-175] These peaks indicate that the gold nanoshells that lie within the laser focal volume at location *d* reside near mitochondria. The spectra from location *e* - *h* show marked differences from that of spectra from locations *a* – *d*. The spectra from location *e* – *h* contain a mixture of protein bands (the 609 cm^{-1} phenylalanine band, the 934/945 cm^{-1} C-C protein backbone stretch, 1292 cm^{-1} amide III stretch and the 1630 cm^{-1} and 1598 cm^{-1} aromatic amino acid ring breathing modes) and nucleic acid bands (676 cm^{-1} thymine/guanine ring breathing mode, the 796 cm^{-1} O-P-O stretch and the 1485 cm^{-1} guanine/adenine ring breathing mode).[18-19,162,167,173-175] This mixture of protein and nucleic acids again suggests that the gold nanoshell in the laser focal volume in the regions *e* – *h* lie either within or in very close proximity of the nucleus. In Table 5.1, the major SERS peaks in the spectra of fibroblast cells incubated with gold nanoshells are tentatively assigned in a concise manner to the biological macromolecules responsible for such peaks and where possible even the particular bonds involved have also been included. It is worth noting that many of the SERS peaks can have several different overlapping biochemical contributions and this is quite common in the complex biological environment inside cells.

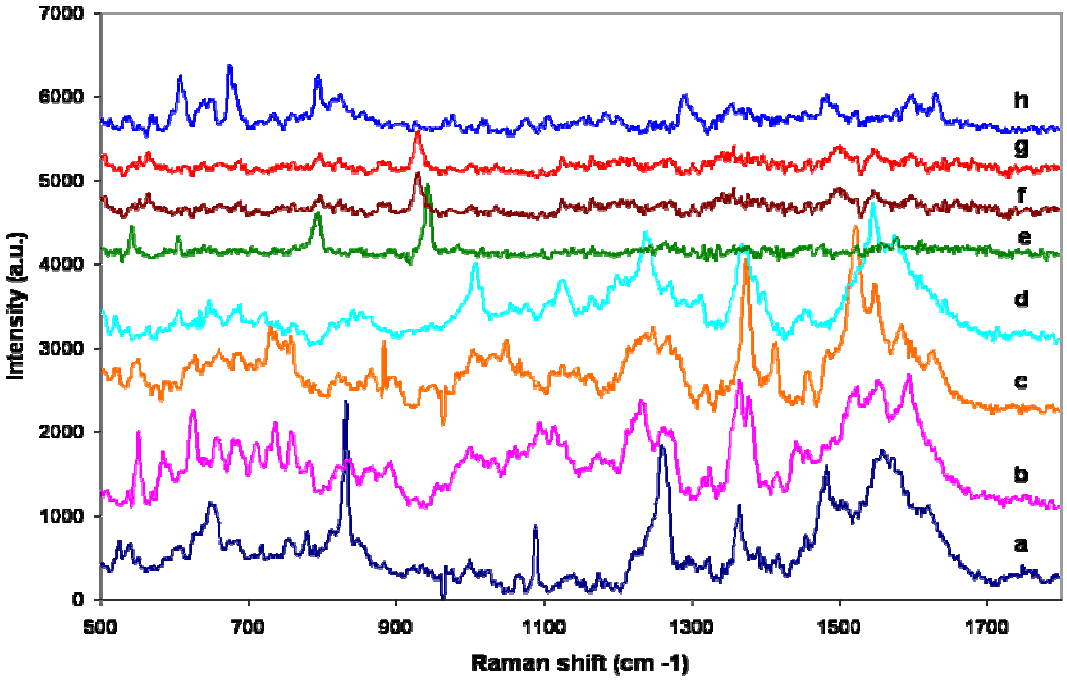

Figure 5.4(A): SERS spectra of fibroblast cell 2 incubated with Au nanoshells.

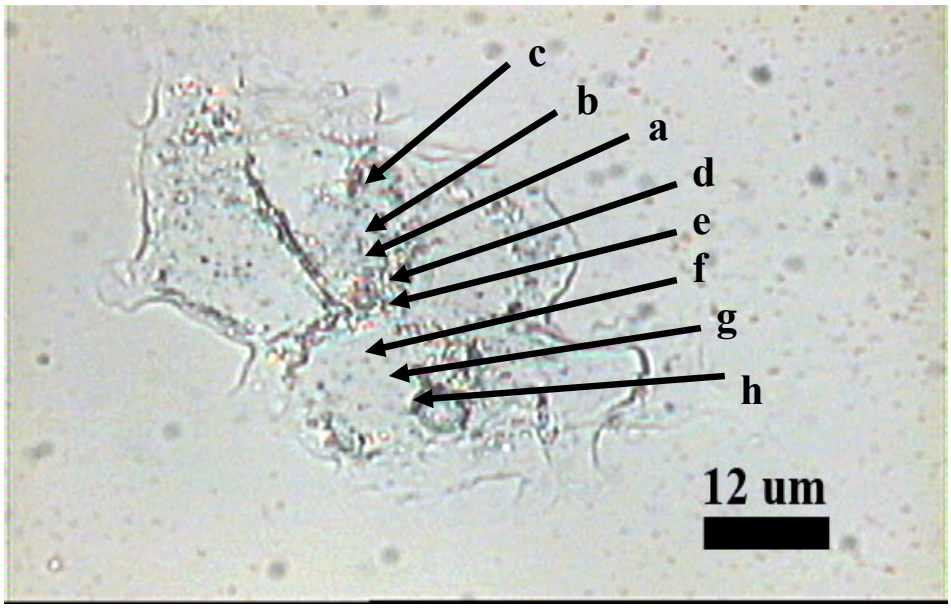

Figure 5.4(B): Brightfield image of fibroblast cell 2 incubated with Au nanoshells showing approximate locations where SERS spectra were collected.

Table 5.1: Tentative band assignments for major SERS peaks in spectra of mouse fibroblast cells incubated with gold nanoshells.

SERS peak frequency (cm^{-1})	**Biological macromolecule responsible for peak along with actual vibrational bonds**
562	(S-S) – **(Protein)**
621	C-C twist of Phe **(Protein)**
641	C-C twist of Tyr **(Protein)**
676	A, T, G **(DNA/RNA)**
796	O-P-O str **(DNA/RNA)**
832	O-P-O asymmetric str **(DNA/RNA)** ; Tyr ring br. **(Protein)**
850	Tyr ring br. **(Protein)**
874	C-C-N^+ sym. Str. **(Lipid)** ; C-O-C ring **(Carbohydrate)**
934	C-C str. α-helix **(Protein)** ; C-O-C glycos. bond **(Carbohydrate)**
988	C-C head groups **(Lipid)**
1002	Sym. Ring br. of Phe **(Protein)**
1089	PO_2^- **(DNA/RNA)**; C-N backbone **(Protein)** ; Chain C-C **(Lipid)** ; C-O & C-C str **(Carbohydrate)**
1129	C-N backbone **(Protein)** ; C-C **(Lipid)**
1240	Amide III β-sheet **(Protein)**
1254	Amide III β-sheet **(Protein)** ; T, A in plane **(DNA/RNA)**
1261	Amide III β-sheet **(Protein)** ; CH def. **(Lipid)**
1291	Amide III α-helix **(Protein)** ; CH def. **(Lipid)**
1303	CH_2 twist **(Lipid)**
1338	A, G in plane ring **(DNA/RNA)** ; CH def. & pyrrole **(Protein)**
1364	CH_3 sym. str. **(Lipid)** ; Porphyrin **(Protein)**
1376	Porphyrin oxidized **(Protein)**
1388	in plane ring vib. **(DNA/RNA)**
1415	COOH **(Protein)**
1485	G, A, CH def. **(DNA/RNA)** ; CH def. **(Protein)**; CH def. **(Lipid)**
1523	Amide II **(Protein)**
1549	C=C **(Lipid)**
1564	C=C **(Lipid)**; (N-C-C-C) **(Protein)**
1588	G, A in plan ring vib. **(DNA/RNA)**
1598	Trp, Tyr **(Protein)**

Gold nanoshells are thus shown to remain as a stable suspension without significant aggregation in DMEM growth medium and were effectively introduced into mammalian cells by pinocytosis. Over the 24 hour timescale required for cellular uptake, the gold nanoshells did not induce cell-death and were used to measure SERS spectra at discrete cellular locations. With a gold nanoshell of diameter 138 nm, and assuming that the local electromagnetic field enhancement on the surface of the gold nanoshell that is responsible for the generation of SERS spectra extends to within 10 nm of the surface of each nanoshell, a probing a volume of 3.27×10^{-19} L can be estimated. Estimating the mean volume of a cell to be 1 pL, average protein content of 7.5×10^{-11} grams of protein/cell [175] and an average weight of a protein molecule as 60 kDa it can be estimated that 240 protein molecules lie in the SERS volume of the nanoshell. The laser spot size used in the experiments is 3 μm at the focal point, hence it can be concluded that multiple nanoshells may lie in the focal volume of the laser during any given scan.

The TEM images of Figures 5.2 revealed that each fibroblast cell can uptake several gold nanoshells. From the myriad of molecular SERS signatures observed, it is shown that gold nanoshells from multiple cellular locations in a wide variety of complex environments can give rise to SERS signals with good signal to noise ratio (SNR). This coupled with the fact the laser spot size at the focal point is 3 μm leads credence to the conclusion that the SERS spectra collected on moving the laser to different locations within a cell are generated by multiple nanoshells.

The study thus demonstrates the ability of gold nanoshells to spectroscopically characterize biomolecules in various cellular locations. The sensitivity of the approach

allows the observation of the oxidation of a metalloprotein such as cytochrome-c within the cell. Cytochromes are found mainly in mitochondria and are responsible for energy processing in the cell. To collect spectra of cytochromes, a nanoshell must be in very close contact with a mitochondrion, as shown in Figures 5.2. It is possible that the heme oxidation in this case is the result of laser excitation. Photo-induced local generation of H_2O_2 in fibroblasts has been previously reported using a low power 647 nm laser,[177] and the mechanism for oxidation of cytochromes by H_2O_2 is well established.[178]

A second set of identical experiments were performed using commercially purchased 60 nm colloidal gold nanoparticles. Figure 5.5 shows the extinction spectra of colloidal gold in water (a), DMEM growth medium in water (b) and colloidal gold in DMEM (c) in conditions that were identical to those when incubating the cells. In these three spectra the blank used to calibrate the spectrophotometer was deionized water. The colloidal gold nanoparticles have an extinction peak located at 533 nm. Since the DMEM growth medium itself has a high absorbance peak at 560 nm (due to the presence of the pH indicator dye phenol red), this drowns the absorbance signal from the colloidal gold when it is added to DMEM growth medium. An extinction spectrum of colloidal gold in DMEM growth medium was obtained by using DMEM as the blank to calibrate the spectrophotometer instead of deionized water (spectrum d). This spectrum reveals the familiar extinction profile of colloidal gold with a slight red shift in its extinction maximum (λ_{max}(water) = 533 nm; λ_{max}(DMEM) = 540 nm). Similar to the case of the gold nanoshells, this level of red-shift of the plasmon resonance peak is in agreement with previously documented behaviour of the surface plasmon waves of noble-metal

nanoparticles in complex biological media of higher refractive index than water and does not indicate aggregation of the nanoshells in DMEM growth medium.[172] Thus it is seen that there is no aggregation of the colloidal gold nanoparticles when added to DMEM growth medium. As a result it can be concluded that the 60 nm colloidal gold nanoparticles being in their natural unaggregated state in DMEM growth medium, will be conducive to pinocytosis by cells on incubation.

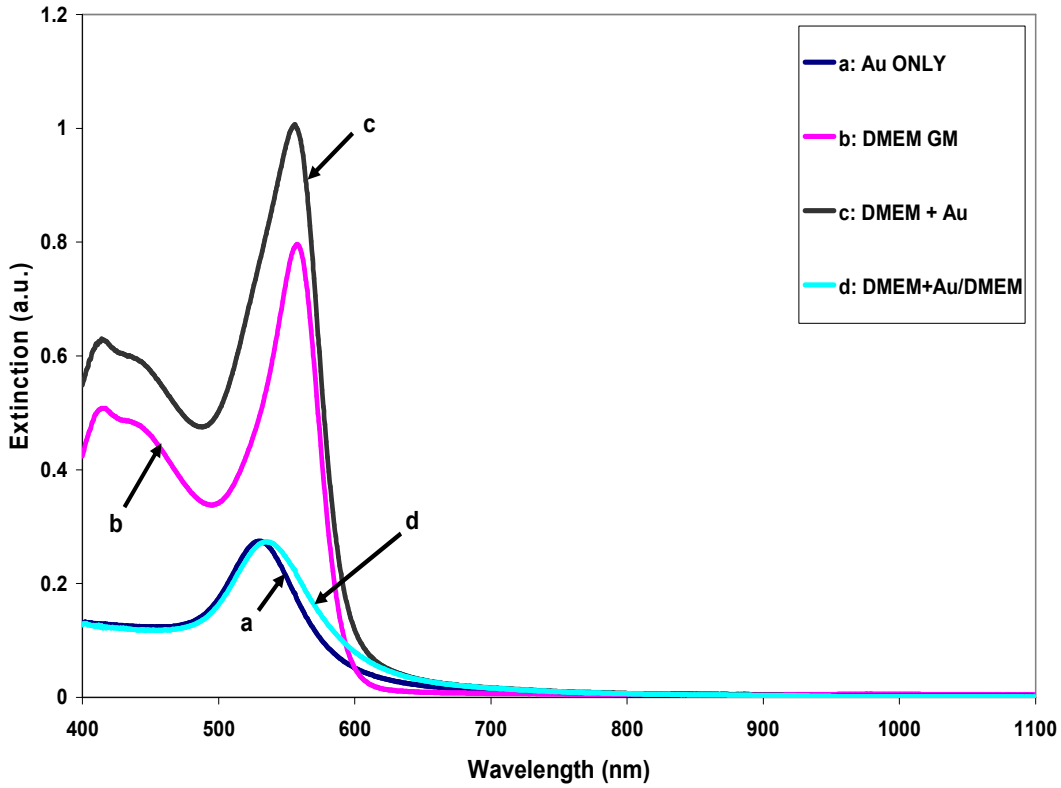

Figure 5.5: Extinction spectra of colloidal Au nanoparticles in water (a), DMEM GM in water (c) and colloidal Au nanoparticles in DMEM (c). These spectra were collected with deionized water as the blank sample for calibrating the spectrophotometer. Spectrum (d) is of colloidal Au nanoparticles in DMEM using DMEM as the blank for calibrating the spectrophotometer.

Figure 5.6(A) shows the SERS spectra taken at four different locations in a fibroblast cell that was incubated with the 60 nm colloidal gold nanoparticles. The approximate locations in the fibroblast where the SERS spectra were collected are depicted in the corresponding brightfield image in Figure 5.6(B). Spectrum *a* in figure 5.6(A) consists of major peaks at 631 cm^{-1} and 648 cm^{-1} which originate from the C-C twist of phenylalanine and tyrosine respectively, 676 cm^{-1} due to thymine/guanine in plane ring vibration, 713 cm^{-1} due to C-C-N^{+} symmetric stretch of lipids, 780 cm^{-1} due to either uracil, cytosine or thymine ring breathing, 826 cm^{-1} due to either an O-P-O stretch of the DNA overlapped with an out of plane ring breathing mode of tyrosine.[162,167,174] This mixture of SERS signal from proteins and nucleic acids suggest that the colloidal gold nanoparticles in the laser focal volume at location *a* reside in close proximity to a nucleus. Spectrum *b* in Figure 5.6(A) was obtained by focusing the laser spot in the cell within 3 μm of location *a*. In addition to the peaks that are similar to those in location *a*, location *b* gives rise to a number of other major peaks at: 1017 cm^{-1} due to C-O stretching mode in nucleic acids, 1076 cm^{-1} due to C-N stretching band of proteins with a possible overlap C-C stretch from lipids, 1095 cm^{-1} due to PO_2^- nucleic acid stretch overlapped with a C-N stretch of a protein backbone, 1128 cm^{-1} due to C-N protein backbone stretch with a possible overlap C-C stretch from lipids, 1177 cm^{-1} due to C-H in plane bend of tyrosine, 1231 cm^{-1} due to amide III stretch of proteins, 1363 cm^{-1} due to CH_3 symmetric stretch of lipids, 1420 cm^{-1} due to a protein pyrole ring vibration overlapped with a DNA/RNA in plane ring vibration, 1456 cm^{-1} due to C-H deformation from either proteins, nucleic acids or lipids, 1543 cm^{-1} due to lipids, 1606 cm^{-1} due to

C=C vibration from either phenylalanine or tyrosine, 1633 cm^{-1} also from the aromatic amino acids and 1653 cm^{-1} from the amide I stretch of proteins with a possible C=C stretch from lipids.[18-19,162,167,173] This mixture of SERS signal from proteins, nucleic acids and in particular lipids suggest that the colloidal gold nanoparticles in the laser focal volume at location *b* reside either in close proximity to a nuclear membrane or are in close proximity to the rough endoplasmic reticulum. Spectra from location *c* and *d* show major differences from that of locations *a* and *b*. They consist of major SERS peaks located at 658 cm^{-1}, 676 cm^{-1}, 716 cm^{-1}, and 1080 cm^{-1} which are similar to those at locations *a* and *b*. They also contain peaks at different locations such as those at: 878 cm^{-1} due to C-C-N^{+} symmetric stretch of lipids overlapped with an carbohydrate C-O-C ring stretch, 1109 cm^{-1} due to a C-N protein stretch and 1624 cm^{-1} due to C=C bands from aromatic amino acids.[162,167,173] The vibrational energy of the bonds responsible for the SERS peaks at location *c* and *d* might indicate that the colloidal gold nanoparticles in the laser focal volume was in the proximity of glycoproteins and phospholipids and thus might suggest the presence of golgi complex. In Table 5.2, the major SERS peaks in the spectra the fibroblast cells incubated with colloidal gold nanoparticles are tentatively assigned in a concise manner to the biological macromolecules responsible for such peaks and where possible even the particular bonds involved have also been included.

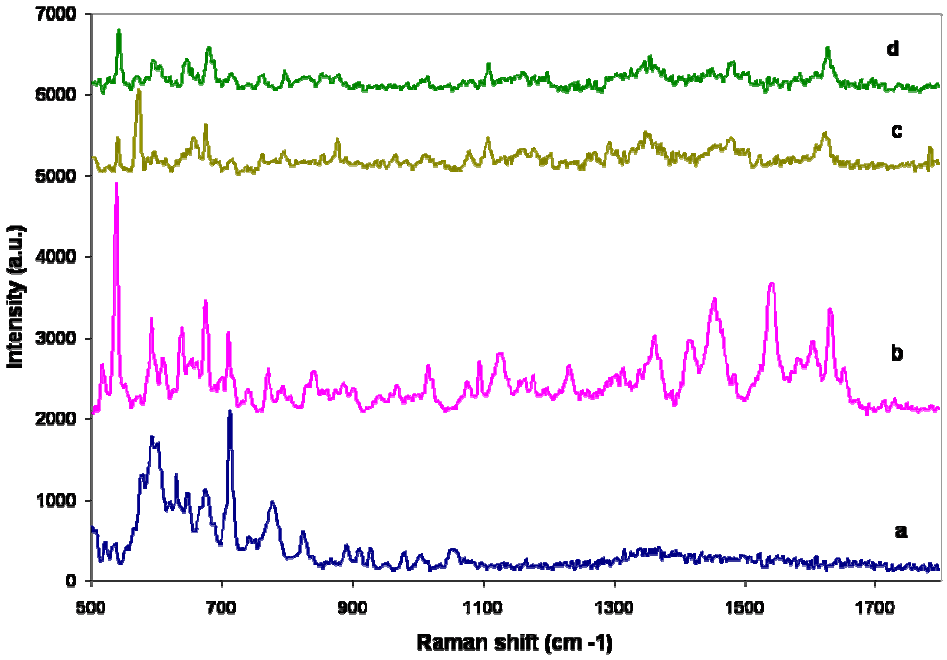

Figure 5.6(A): SERS spectra of fibroblast cell incubated with colloidal Au nanoparticles.

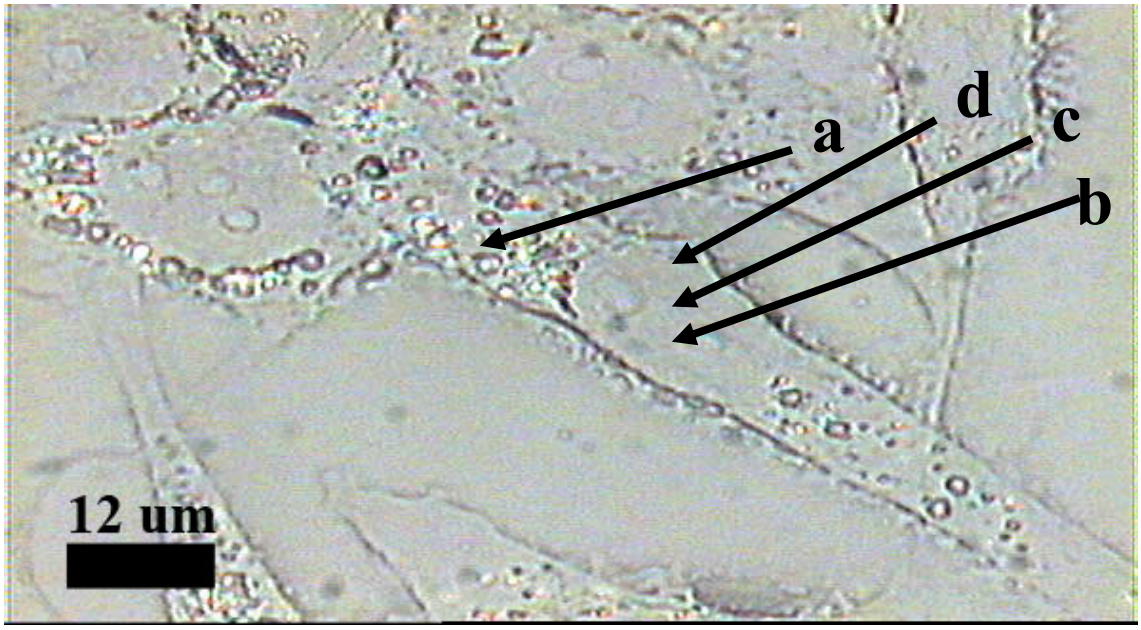

Figure 5.6(B): Brightfield image of fibroblast cell incubated with colloidal gold nanoparticles showing approximate locations where SERS spectra were collected.

Table 5.2: Tentative band assignments for major SERS peaks in spectra of mouse fibroblast cells incubated with colloidal gold nanoparticles.

SERS peak frequency (cm^{-1})	**Biological macromolecule responsible for peak along with actual vibrational bond**
610	Phe **(Protein)**
648	C-C twist of Tyr **(Protein)**
676	A, T, G in plane ring vbr. **(DNA/RNA)**
713	$CN^{+}(CH_3)_3$ sym. str. **(Lipid)**
780	U, C, T ring br. **(DNA/RNA)**
826	O-P-O str. **(DNA/RNA)** ; out of plane ring br. of Tyr **(Protein)**
878	C-C-N^{+} sym. str. **(Lipid)** ; C-O-C ring **(Carbohydrate)**
1017	C-O **(DNA)**
1076	C-N str. **(Protein)** ; Chain C-C str. **(Lipid)** ; C-O str. **(Carbohydrate)**
1095	PO_2^{-} str. **(DNA/RNA)**
1109	C-N str. **(Protein)**
1128	C-N str. (Protein) ; Chain C-C str. **(Lipid)** ; C-O str. **(Carbohydrate)**
1177	C-H in plane bend of Tyr **(Protein)**
1231	Amide III random coil **(Protein)**
1363	CH_3 sym. str. **(Lipid)** ; backbone **(Protein)** ; in plane ring vbr. **(DNA/RNA)**
1420	Pyrrole ring vbr. (Protein) ; in plane ring vbr. **(DNA/RNA)**
1456	G, A, CH def. **(DNA/RNA)** ; CH def. **(Protein)**; CH def. **(Lipid)** ; CH def. **(Carbohydrate)**
1543	**(Lipid)** ; **(DNA/RNA)**
1606	C=C of Phe, Tyr **(Protein)**
1624	C=C of Tyr, Trp **(Protein)**
1633	Trp, Tyr, Phe **(Protein)**

Since colloidal gold has generally been the traditional SERS substrates used to incubate cells and detect intracellular constituents, a direct comparison with gold nanoshells provides insight on the efficacy of this new method of gold nanoshell based intracellular component detection. A comparison of the data provided in Figures 5.3, 5.4 and 5.6 and the ensuing analysis reveals that gold nanoshells provide comparable signal strength and spatial resolution to that of the colloidal gold nanoparticles. Thus it is

shown gold nanoshells do not compromise sensitivity when used to probe cells intracellularly. The gold nanoshells also showed good signal variability from one location of the cell to the other and thus allowed drawing conclusions on the nature of the various cellular constituents/organelles that it was probing. This demonstration of the utility of gold nanoshells in SERS imaging is important since it can potentially allude to an advantage over the use of gold colloid as SERS contrast agents. It has been shown that colloidal gold nanoparticles have poor intrinsic SERS qualities when they are spatially isolated.[179,180] The SERS enhancement factor that for gold colloidal nanoparticles under near infrared excitation can increase by as much as eleven orders of magnitude when colloidal gold clusters are formed by aggregation of the colloids. [180] Hence they serve as useful SERS substrates when aggregated. [32,179-180] This phenomenon can be seen in Figures 5.7(A) and 5.7(B). Figure 5.7(A) shows the extinction spectra of single isolated colloidal gold nanoparticles (in water) and aggregated gold colloid at varying times after commencement of aggregation by the addition of sodium chloride. It can be seen the isolated gold colloid has very low extinction value at 785 nm. It is only after aggregation that colloidal gold attains a high extinction value at 785 nm. Figure 5.7(B) shows SERS spectra taken of 154 μM adenine with both isolated colloidal gold (in water) and with aggregated colloid by addition of salt. Here the sharp 738 cm^{-1} peak of adenine only occurs when the gold colloid is aggregated thus lending credibility to the belief that colloidal gold nanoparticles show appreciable SERS enhancement at 785 nm only upon aggregation. Hence like in water, the SERS enhancement that gold colloid provide inside cells can also be influenced by the kinetics of the aggregation process and

the plasmonic properties of the aggregated clusters formed, which is a function of cluster shape and size in addition to conditions inside the cell. In contrast, the use of metal nanoshells where each individual nanoshell can be individually tuned to provide optimal plasmonic activity in the wavelength of the laser used to probe cells can prove to be a more efficient process for SERS based intracellular biomolecule detection. This can potentially give optimal signal enhancements and reproducibility.

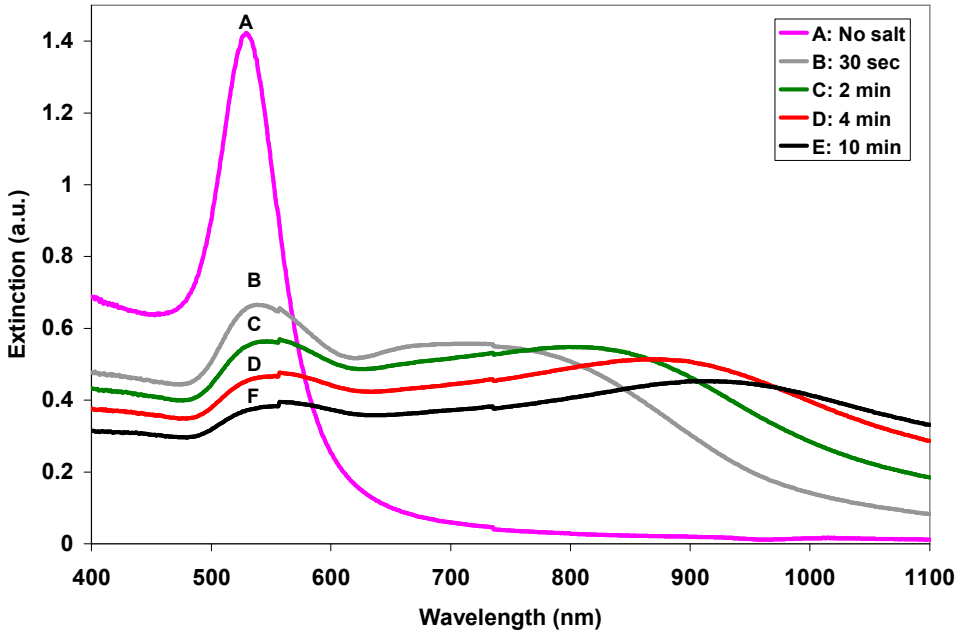

Figure 5.7(A): Extinction spectra of 60 nm colloidal gold nanoparticles in water before aggregation (A) and at various times after aggregation through the addition of salt (B-E).

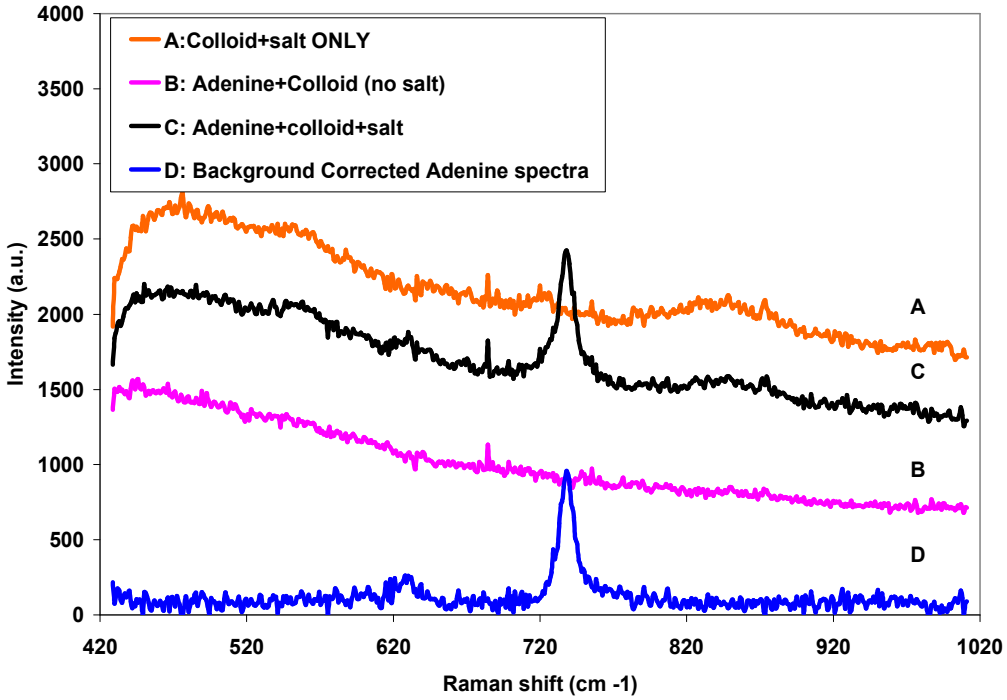

Figure 5.7(B): SERS spectra of aggregated colloidal gold (A), 154 μM adenine with unaggregated colloidal gold (B) and 154 μM adenine with aggregated colloidal gold (C). Also shown is the background corrected adenine SERS spectrum (D). All tests were carried out in water.

CHAPTER VI

CONCLUSIONS AND FUTURE WORK

This dissertation deals with the various aspect of using metal nanoparticles as SERS substrates in biomedical applications. It initially deals with the use of colloidal silver nanoparticles for the detection of human integrins, bovine serum albumin and calf thymus DNA. The results of these initial round of experiments indicate that while colloidal nanoparticles are capable of generating significant SERS enhancement of Raman signals from bioanalytes, the need to induce aggregation for providing the required plasmonic conditions for optimal SERS enhancements compromises the robustness of these nanoparticles for producing reproducible SERS signals. This makes them undesirable options for implementation in any SERS based biosensor.

The need to circumvent the aggregation problem lead to the search for fabricating and/or obtaining robust SERS substrates with plasmonic properties that are not based on aggregation. One such substrate fabricated and characterized was via thermal vapor deposition of silver onto ultra clean microscope glass slides under high vacuum conditions. Although careful control of parameters such as the rigorousness of the microscope slide cleaning process, silver deposition rate, deposition geometry, temperature during silver deposition and quality of glass substrate helped the reproducibility of substrate preparation, these substrates were always plagued with an inherent problem that ultimately compromised their robustness as well. This was the inability to control the shape, size and interparticle distance of the silver island films that

forms on the glass surface as a result of the vapor deposition of silver. It is imperative that the silver films be in the form of discontinuous islands to provide the necessary nanometer scale roughness to get optimal SERS enhancement. Since the substrate preparation process did not include the presence of any lithographic masks that could control the morphology of the deposited silver (and thus also the optical properties), there was no definite way to ensure control of the shape and size of the silver island films. This lead to areas in the film with different packing density and size distributions of the silver islands. In addition AFM studies revealed that there were also regions in the film where large microscopic (as opposed to sub-microscopic) silver clusters formed. This could be the result of imperfections in the microscope glass slides or drift in the current used in heating silver powder in tungsten wells in the vacuum chambers which leads to sudden bursts of large amounts of the silver vapor. This kind of drift is quite common when depositing metals in a vacuum chamber. Again the absence of a deposition masks allowed the formation of such microscopic silver clusters.

The lack of control of surface morphology in vapor deposited silver island films lead to the need to fabricate lithographically based SERS substrates with the presence of deposition masks which would govern the shape, size and distribution of the silver nanoparticles on the surface of the supporting substrate. As a result the technique of Nanosphere Lithography (NSL) was employed to create silver periodic particle arrays arranged in a close hexagonally packed formation. This technique employed the use of carboxyl functionalized latex polystyrene beads which self-assembled on the glass surface to form a uniform monolayer which served as the deposition mask. Here the

shape, size and distribution of the silver nanoparticles were governed by the size of the individual polystyrene mask used to create the mask. These nanoparticle parameters in addition to the depth of the silver deposition governs the optical properties of the substrates in terms of both the location and magnitude of the surface plasmon resonance as well as its full-width at half maximum (FWHM). This will govern the efficiency of SERS enhancement that the substrate can induce on a Raman active analyte in contact with it. The results of the substrate fabricated and characterized indicate that the technique can successfully create ordered silver particles in a hexagonally close packed pattern. The AFM images obtained from the samples indicate that there are several lattice defects that are created within at least every 5μm. The most common lattice defects are slip dislocations, grain boundaries and point defects. In addition, the brightfield images indicate that the latex bead mask formed a uniform monolayer only in certain areas of the substrates. Large patches of the substrate have continuous layers of bulk silver which were deposited directly on the glass as there was no mask there. It is important to locate a "good" area before performing any SERS analysis. The results of both the UV-Vis absorption and SERS characterization of the substrates with 20, 40 and 80 nm Ag deposition reveal that the 40 nm Ag height substrate had the largest area of uniform silver periodic particles arrays which is revealed by the sharp plasmon resonance peak of the substrate. The strongest SERS enhancement BPE on the 40 nm sample is the result of uniform sample morphology and the closet proximity of its plasmon resonance wavelength (835 nm) to that of the incident laser wavelength (785 nm). The sample with 80 nm Ag deposition has an extremely broad plasmon resonance

peak with high magnitude. This broad plasmon resonance peak can result from contributions of multipole resonances (in addition to the dipole resonance) as 80 nm (in the axis of deposition) is well out of the Rayleigh size limit and also from large areas of lattice defects. The high extinction value indicates high scattering from large silver clumps that were formed in areas with insufficient nanosphere mask packing. The low strength of the SERS signal from BPE generated from the 80 nm sample is because its plasmon resonance at 710 nm is farthest away from the incident laser wavelength (785 nm) and can also be due to poor lattice quality. Future work needs to focus on optimizing the technique for nanosphere mask deposition so that fewer lattice defects occur. Currently mask deposition is done by drop coating the nanosphere colloidal suspension on the glass substrate. This can be improved by applying the process of convective self-assembly to deposit the nanosphere mask. [77] This technique involves using a thin Teflon sheet connected to a microscope cover slip as a spreader which is placed at a distance *h* above the glass substrate. The glass substrate itself is placed on top of a programmable X-Y translation stage. By placing a drop of the nanosphere mask solution at the edge of the substrate and moving the stage (and hence the substrate) at a constant rate (around 0.035 mm/sec or so) the spreader can help create a more uniform layer of the colloidal mask in a two dimensional array with fewer lattice defects. The height of the spreader from the glass substrate along with the rate of movement of the translational stage are parameters that can be optimized to produce the best quality of the mask. The reproducibility of the nanosphere mask quality from batch to batch can also

be increased by creating masks in environments with controlled temperature and humidity.

Another SERS substrate with controllable optical properties that was used in this dissertation is the gold nanoshell films on glass. Although the UV-Vis and SERS characterization of these substrates revealed no major problems with morphological structure, the AFM analysis showed that there is obvious room for improvement in the formation of the nanoshell films. Future work should focus on creating gold nanoshell films of higher packing density by increasing the amount of time the PVP coated glass slide is soaked in the gold nanoshell solution and also through the addition sodium chloride midway through the gold deposition step to neutralize the nanoshell surface charge and increase nanoshell packing density.

Early work on the development of a gold nanoshell based SERS sensor for β-amyloid detection shows promise that SERS might be successfully employed as a detection modality for β-amyloid. The distance dependence studies performed using aniline bound to various chain length carbon molecules as spacers from the gold nanoshell surface provides encouraging results that the electromagnetic field around the gold nanoshells that is responsible for the SERS effect extends far enough for PAMAM dendrimers to be employed as the bio-recognition molecule for β-amyloid. . It appears that by labeling the dendrimer with sialic acid,[154] it is possible to produce a molecule that is both highly selective for Aβ ($K_{A\beta} > 1 \times 10^7$ M) and closely mimics the cell surface structures (gangliosides). Future work needs to focus on continuing research on minimizing dendrimer size without compromising its specificity for β-amyloid. Hence

the efficiency of the final sensor is going to be heavily dependant upon the exact size, selectivity, and binding capacity of the final recognition molecule employed. As far as the SERS aspect of the sensor platform is concerned, future work needs to be heavily invested in improving quality control issues in the fabrication of the nanoshell films. Currently the nanoshell films alone have a large SERS background in the 500 – 1800 cm^{-1} range which is a critical region for most biological Raman bands. Future work needs to focus on diagnosing the chemical origins behind these bands and modifying the film preparation technique to reduce or eliminate the use of any chemicals that might cause the appearance of such unnecessary bands. Once the fabrication technique for the gold nanoshell films have been optimized, the sensor will need to be implemented in an assay to detect synthetic β-amyloid in buffer (which is relatively easy to make) in order to study whether it has the required SERS sensitivity to detect β-amyloid in biologically relevant concentrations. If no SERS signal is obtained from the β-amyloid or if signal strength obtained is too weak, modifications have to be made to the sensor chemistry to further reduce its size so that the captured β-amyloid is closer to the gold nanoshell surface. Another modification to the sensor that might be employed is to have the β-amyloid capture chemistry on a regular glass slide instead of one coated with a nanoshell film. Once the capture process is completed, a microscope cover slip coated with a gold nanoshell film can be inverted on top of the captured β-amyloid on the glass slide. That way the gold nanoshell film will be in direct contact with the β-amyloid which might enhance its SERS signal. Once the detection mechanism in buffer is optimized, future work will then need to focus on performing and optimizing assays with cerebrospinal

fluid and brain extracts of patients with Alzheimer's disease along with age matched normal control patients.

This dissertation includes ongoing studies which show that gold nanoshells can be successfully introduced into living fibroblast cells without inducing cell death in a 24 hour incubation period and that they can be used to identify different biomolecules within cells using SERS. The technique also has the required sensitivity to differentiate between proteins, nucleic acids, lipids and other complex biomolecules that are present within a cell. The ability of tunable gold nanoshells to generate strong intracellular SERS signals has immense scientific potential. Future work needs to focus on functionalizing the Au nanoshells and then implanting them in specific locations within cells in order to use it for detecting specific cell organelles and/or monitoring specific biochemical products. Another avenue that needs attention in future research is testing the robustness and biocompatibility of such implanted Au nanoshells to investigate how long cells can withstand the functionalized nanoshells without adverse effects. A full toxicological analysis might require the use of RNA profiling to investigate whether the cell recognizes the nanoshells as "foreign". Efforts might then need to be made to improve biocompatibility of such implanted biosensors. These results represent the first steps in the development of a robust metal nanoshell based SERS biosensor that can be engineered to probe specific cell organelles and/or intracellular biochemicals with the goal of ultimately improving the ability to monitor biological processes in real time. This opens new avenues for designing systems for early diagnosis of diseases by exploiting any biochemical changes such diseases might force upon a healthy cell. The use of gold

nanoshells to provide spatially-resolved Raman contrast obviates the need for fluorescent labeling and can therefore avoid problems such as photobleaching. Another useful aspect of SERS obtained by the nanoshells is that in comparison with fluorescence signals, SERS signals are much sharper and hence are more advantageous for multiplexing. Additionally, since most of the biochemical molecules that are responsible for SERS enhancement are in contact or in very close proximity to the gold nanoshell surface, any autofluorescence by such molecules will be quenched as a result of the metal surface. This can help to improve signal to noise ratio. The ability to place sensors in cells and to differentiate cellular components has potential to be a valuable tool for systems biology. The molecular information gained by using such a nanoshell based SERS biosensor can be highly complementary to the high content, but spatially unresolved data gained through microarray experiments and thus improve the ability to monitor biological processes in real time. Hence future work will need to focus attention on developing innovative techniques to integrate the SERS signal obtained from Au nanoshell biosensor with other modalities used for cell monitoring to get a complete picture of biochemical processes within cells.

REFERENCES

1. C. L. Stevenson and T. Vo-Dinh, "Signal expressions in Raman spectroscopy," in *Modern Techniques in Raman Spectroscopy*, Ed. J. J. Laserna, John Wiley and Sons Publishers, West Sussex, England, 1-39 (1996).
2. A. Rupérez and J.J. Laserna, "Surface-enhanced Raman spectroscopy," in *Modern Techniques in Raman Spectroscopy*, Ed. J. J. Laserna, John Wiley and Sons Publishers, West Sussex, England, 227-264 (1996).
3. K. Kneipp, H. Kneipp, I. Itzkan, R.R. Dasari, and M.S. Feld, "Surface-enhanced Raman scattering and biophysics," *J. Phys. Condens. Matter* **14**, R597-R624 (2002).
4. C. A. Murray, "Molecule-silver separation distance," in *Surface Enhanced Raman Scattering*, Ed. Chang R.K, and Furtak T.E., Plenum Press, New York, NY, 203-221 (1982).
5. M. Moskovits, "Surface-enhanced spectroscopy," *Reviews of Modern Physics* **57**(3), 783-826 (1985).
6. F. J. Garcia-Vidal and J. B. Pendry, "Collective theory for surface enhanced Raman scattering," *Physical Review Letters* **77**(6), 1163-1166 (1996).
7. K. Kneipp , H. Kneipp, I. Itzkan, R. R. Dasari, and M. S. Feld, "Ultrasensitive chemical analysis by Raman spectroscopy," *Chem. Rev*. **99**, 2957-2975 (1999).
8. M. Kerker, D.-S. Wang, and H. Chew, "Surface enhanced Raman scattering (SERS) by molecules adsorbed at spherical particles: Errata," *Applied Optics* **19**(24), 4159-4174 (1980).

9. D.A. Weitz, S.Garoff, J.I. Gersten, and A. Nitzan, "The enhancement of Raman scattering, resonance Raman scattering, and fluorescence from molecules adsorbed on a rough silver surface," *J. Chem. Phys.* **78**(9), 5324-5338 (1983).

10. J.A. Creighton, C.G. Blatchford and M.G. Albrecht, "Plasma resonance enhancement of Raman scattering by pyridine adsorbed on silver and gold sol particles of size comparable to the excitation wavelength," *J. Chem. Soc, Faraday Trans. II* **75**, 790-798 (1979).

11. C.G. Blatchford, J.R. Campbell, and J.A. Creighton, "Plasma resonance – enhanced Raman scattering by adsorbates on gold colloids: the effects of aggregation," *Surface Science* **120**, 435-455 (1982).

12. P.C. Lee and D. Miesel, "Adsorption and surface-enhanced Raman of dyes on silver and gold sols," *J. Phys. Chem*. **86**, 3391-3395 (1982).

13. G.D. Chumanov, R.G. Efremov, and I.R. Nabiev, "Surface-enhanced Raman spectroscopy of biomolecules," *J. Raman Spectroscopy* **21**, 43 - 48 (1990).

14. S. K. Kim, M. S. Kim and S. W. Suh, "Surface-enhanced Raman scattering (SERS) of aromatic amino acids and their glycyl dipeptides in silver sol," *J. Raman Spectroscopy* **18**, 171- 175 (1987).

15. I.R. Nabiev, V.A. Savchenko, and E.S. Efremov, "Surface-enhanced Raman spectra of aromatic amino acids and proteins by silver hydrosols," *J. of Raman Spectroscopy* **14(6)**, 375-379 (1983).

16. X. Dou, Y.M. Jung, H.Yamamoto, S. Doi, and Y. Ozaki, "Near-infrared excited surface-enhanced Raman scattering of biological molecules on gold colloid I:

Effects of pH of the solutions of amino acids and their polymerization," *Appl. Spectrosc.* **53**(2), 133-138 (1999).

17. X. Dou, Y.M. Jung, Z.-Q. Cao, and Y. Ozaki, "Surface-enhanced Raman scattering of biological molecules on metal colloid II: Effects of aggregation of gold colloid and comparison of effects of pH of glycine solutions between gold and silver colloids," *Appl. Spectrosc.* **53**(11), 1440-1447 (1999).
18. H. Deng, Q. He, Z. Xu, X. Wang, and R. Sheng, "The study of Turnip Mosaic virus coat protein by surface enhanced Raman spectroscopy," *Spectrochimica Acta Part A* **49**(12), 1709-1714 (1993).
19. J. Hu, R.S. Sheng, Z.S. Xu, and Y. Zeng, "Surface enhanced Raman spectroscopy of lysozyme," *Spectrochimica Acta Part A* **51**(6), 1087-1096 (1995).
20. S.C.-Pînzaru, S. Cavalu, N. Leopold, R. Petry, and W, Keifer, "Raman and surface-enhanced Raman spectroscopy of tempyo spin labeled ovalbumin," *Journal of Molecular Structure* **565-566**, 225-229 (2001).
21. P. Miškovský, D. Jancura, S.S.-Cortés, E. Kočišová, and L. Chinsky, "Antiretrovirally active drug hypericin binds the IIA subdomain of human serum albumin: Resonance Raman and surface-enhanced Raman spectroscopy study," *J. Am. Chem. Soc.* **120**, 6374-6279 (1998).
22. P. Miskovsky, J. Hritz, S.S.-Cortes, G. Fabriciova, J. Ulicny, and L. Chinsky, "Interaction of hypericin with serum albumins: Surface enhanced Raman spectroscopy and molecular modeling study," *Photochemistry and Photobiology* **74**(2), 172-183 (2001).

23. N.H. Jang, "The coordination chemistry of DNA nucleosides on gold nanoparticles as a probe by SERS," *Bull. Korean Chem. Soc.* **23**(12), 1790-1800 (2002).

24. K. Kneipp and J. Flemming, "Surface enhanced Raman scattering (SERS) of nucleic acids adsorbed on colloidal silver particles," *Journal of Molecular Structure* **145**, 173-179 (1986).

25. K. Kneipp, W. Pohle and H. Fabian, "Surface enhanced Raman spectroscopy of nucleic acids and related compounds adsorbed on colloidal silver particles," *Journal of Molecular Structure* **244**, 183-192 (1991).

26. J. Thorton and R.K. Force, "Surface-enhanced Raman spectroscopy of nucleic acid compounds and their mixtures," *Appl. Spectrosc.* **45**(9), 1522-1526, (1991).

27. S.K. Kim, T.H. Joo, S.W. Suh, and M.S. Kim, "Surface-enhanced Raman scattering (SERS) of nucleic acid components in silver sol: Adenine series," *Journal of Raman Spectroscopy* **17**, 381-386 (1986).

28. D. Graham, W.E. Smith, A.M.T. Linacre, C.H. Munro, N.D. Watson, and P.C. White, "Selective detection of deoxyribonucleic acid at ultralow concentrations by SERRS," *Anal. Chem.* **69**, 4703-4707 (1997).

29. K. Kneipp, H. Kneipp, V.B. Kartha, R. Manoharan, G. Deinum, I. Itzkan, R.R. Dasari, and M.S. Feld, "Detection and identification of a single DNA base molecule using surface-enhanced Raman scattering (SERS)," *Phys. Rev. E* **57**(6), R6281-R6284 (1998).

30. K. Kneipp, H. Kneipp, I. Itzkan, R.R. Dasari, and M.S. Feld, "Near-infrared surface-enhanced Raman spectroscopy of biomedically relevant single molecules on colloidal silver and gold clusters," *Proceedings of SPIE* **3922**, 49-55 (2000).

31. L.A. Gearheart, H.J. Ploehn, and C.J. Murphy, "Oligonucleotide adsorption to gold nanoparticles: A surface-enhanced Raman spectroscopy study of intrinsically bent DNA," *J. Phys. Chem. B* **105**, 12609-12615 (2001).

32. K. Kneipp, A.S. Haka, H. Kneipp, K. Badizadegan, N. Yoshizawa, C. Boone, K.E. Shafer-Peltier, J.T. Motz, R.R. Dasari, and M.S. Feld, "Surface enhanced Raman spectroscopy in single living cells using gold nanoparticles," *Applied Spectroscopy* **56**(2), 150-154 (2002).

33. C. Eliasson, A. Lorén, J. Engelbrektsson, M. Josefson, J. Abrahamsson, and K. Abrahamsson, "Surface-enhanced Raman scattering imaging of single living lymphocytes with multivariate evaluation," *Spectrochimica Acta A* **61**, 755-760 (2005).

34. W.R. Premasiri, D.T. Moir, M.S. Klempner, N. Krieger, G. Jones II, and L.D. Ziegler, "Characterization of the surface enhanced Raman scattering (SERS) of bacteria," *J. Phys. Chem. B* **109**, 312-320 (2005).

35. L.R. Allain and T. Vo-Dinh, "Surface-enhanced Raman scattering detection of the breast cancer susceptibility gene *BRCA1* using silver-coated microarray platform," *Analytica Chimica Acta* **469**, 149-154 (2002).

36. T. Vo-Dinh, L.R. Allain, and D.L. Stokes, "Cancer gene detection using surface-enhanced Raman scattering (SERS)," *J. Raman Spectroscopy* **33**, 511-516 (2002).

37. T. Vo-Dinh, D.L. Stokes, G.D. Griffin, M. Volkan, U.J. Kim, and M.I. Simon, "Surface-enhanced Raman scattering (SERS) method and instrumentation for genomics and biomedical analysis," *J. Raman Spectroscopy* **30**, 785-793 (1999).

38. X. Dou, T. Takama, Y. Yamaguchi, and H. Yamamoto, "Enzyme immunoassay utilizing surface-enhanced Raman scattering of the enzyme reaction product," *Anal. Chem.* **69**, 1492-1495 (1997).

39. S.R. Hawi, S. Rochanakij, F. Adar, W.B. Campbell, and K. Nithipatikom, "Detection of membrane-bound enzymes in cells using immunoassay and Raman microspectroscopy," *Analytical Biochemistry* **259**, 212-217 (1998).

40. Y.W.C. Cao, R.C. Jin, and C.A. Mirkin, "Nanoparticles with Raman spectroscopic fingerprints for DNA and RNA detection," *Science* **297**, 1536-1540 (2002).

41. Y.C. Cao, R.C. Jin, J.M. Nam, C.S. Thaxton, and C.A. Mirkin, "Raman dye-labeled nanoparticle probes for proteins," *J. Am. Chem. Soc.* **125**, 14676-14677 (2003).

42. D.A. Stuart, A.J. Haes, A.D. McFarland, S. Nie, and R.P. Van Duyne, "Refractive index sensitive, plasmon resonant scattering, and surface enhanced Raman scattering nanoparticles and arrays as biological sensing platforms," *Proc. SPIE, Int. Soc. Opt. Eng.* **5327**, 60-73 (2004).

43. S.P. Mulvaney, M.D. Musick, C.D. Keating, and M.J. Natan, "Glass coated, analyte tagged nanoparticles: A new tagging based on detection with surface-enhanced Raman scattering," *Langmuir* **19**, 4784-4790 (2003).

44. W.E. Doering, and S. Nie, "Single-molecule and single nanoparticle SERS: Examining the roles of surface active sites and chemical enhancement," *J. Phys. Chem. B* **106**, 311-317 (2002).

45. B.K. Nunnally, "It's a mad, mad, mad, mad cow: A review of analytical methodology for detecting BSE/TSE," *Trends in Anal. Chem*. **21**, 82-88 (2002).

46. A.F. Horwitz, "Integrins and health," *Scientific American,* 68-75 (May 1997).

47. R.O. Hynes, "Integrins: Bidirectional, allosteric signaling machines," *Cell* **110**, 673-687 (2002).

48. R.O. Hynes, "Integrins: Versatality, modulation and signaling," *Cell* **69**(1), 11-25 (1992).

49. L. A. Martinez-Lemus, Z. Sun, A. Trache, J. P. Trzciakowski, and G. A. Meininger, "Integrins and regulation of the microcirculation: From arterioles to molecular studies using atomic force microscopy," *Microcirculation* **12**, 1-14 (2005).

50. L.A. Martinez-Lemus, X. Wu, E. Wilson, M.A. Hill, G.E. Davis, M.J. Davis, G.A. Meininger, "Integrins as unique receptors for vascular control," *J. Vasc. Res.* **40**, 211-233 (2003).

51. J.E. Mogford, G.E. Davis, S.H. Platts, and G.A. Meininger, "Vascular smooth muscle alpha v beta 3 integrin mediates arteriolar vasodilation in response to RGD peptides," *Circ Res.* **79**, 821–826 (1996).

52. J.E. Mogford, G.E. Davis, and G.A. Meininger, "RGDN peptide interaction with endothelial α5ß1 integrin causes sustained endothelin-dependent vasoconstriction of rat skeletal muscle arterioles," *J. Clin. Invest.* **100**, 1647–1653 (1997).

53. C.H. Munro, W. E. Smith, M. Garner, J. Clarkson and P.C. White, "Characterization of the surface of a citrate-reduced colloid optimized for use as a substrate for surface-enhanced resonance Raman scattering", *Langmuir* **11**, 3712-3720 (1995).

54. G. Mie, "Beitrage zur optik truber medien, speziell kolloidaler metallosungen", *Ann. Physik* **25**, 377-445 (1908).

55. S. Stewart and P.M. Fredericks, "Surface enhanced Raman spectroscopy of peptides and proteins adsorbed on an electrochemically prepared silver surface", *Spectrochimica Acta Part A* **55**, 1615-1640 (1999).

56. T.J. Yu, J.L. Lippert, and W.L. Peticolas, "Laser Raman studies of conformational variations of poly-L-lysine," *Biopolymers* **12**, 2161-2176 (1973).

57. S. C. Erfurth and W. I. Peticolas, "Melting and premelting phenomenon in DNA by laser Raman scattering," *Biopolymers* **14**, 247-264 (1975).

58. L. Stryer, *Biochemistry* 4th Ed., W.H. Freeman and Company, New York, NY (1995).

59. Z. Q. Wen, S. A. Overman, P. Bondre and G. J. Thomas Jr., "Structure and organization of bacteriophage Pf3 probed by Raman and ultraviolet resonance Raman spectroscopy," *Biochemistry* **40**, 449-458 (2001).

60. D.J. Semin and K.L. Rowlen, "Influence of vapor deposition parameters on SERS active Ag film morphology and optical properties," *Anal. Chem.* **66**, 4324-4331 (1994).

61. S.E. Roark and K.L. Rowlen, "Thin Ag films: Influence of substrate and postdeposition treatment on morphology and optical properties," *Anal. Chem.* **66**, 261-270 (1994).

62. V.L. Schlegel and T.M. Cotton, "Silver-island films as substrates for enhanced Raman scattering: Effect of deposition rate on intensity," *Anal. Chem.* **63**, 241-247 (1991).

63. R.P. Van Duyne, J.C. Hulteen and D.A. Treichel, "Atomic force microscopy and surface-enhanced Raman spectroscopy. I. Ag island films and Ag film over polymer nanosphere surfaces supported on glass," *J. Chem. Phys.* **99(3)**, 2101-2115, (1993).

64. S.E. Roark, D.J. Semin, A. Lo, R.T. Skodje, and K.L. Rowlen, "Solvent-induced morphology changes in thin silver films," *Analytica Chimica Acta* **307**, 341-353, (1995).

65. A. Kikuchi, S. Baba and A. Kinbara, "Measurement of the adhesion of silver films to glass substrates," *Thin Solid Films* **124**, 343-349 (1985).

66. R.L. Birke, C. Shi, W. Zhang, and J.R. Lombardi, "A time-resolved SERS study of the adsorption and electrochemical reduction of 4-pyridinecarboxaldehyde and 4-(hydroxymethyl)pyridine," *J. Phys. Chem. B* **102**, 7983-7996 (1998).

67. W. Gotschy, K. Vonmetz, A. Leitner, F.R. Aussenegg, "Thin films by regular patterns of metal nanoparticles: Tailoring the optical properties by nanodesign," *Appl. Phys. B.* **63**, 381-384, (1996).

68. W. Gotschy, K. Vonmetz, A. Leitner, and F.R. Aussenegg, "Optical dichroism of lithographically designed silver nanoparticle films," *Optics Letters*, **21**(15), 1099-1101 (1994).

69. M. Salerno, N. Felidj, J.R. Krenn, A. Leitner, and F.R. Aussenegg, "Near-field optical response of a two dimensional grating of gold nanoparticles," *Phys. Rev. B* **63**, 165422-1 – 165422-6 (2001).

70. N. Félidj, J. Aubard, G. Lévi, J.R. Krenn, M. Salerno, G. Schider, B. Lamprecht, A. Leitner, and F.R. Aussenegg, "Controlling the optical response of regular arrays of gold particles for surface-enhanced Raman scattering," *Phys. Rev. B* **65**, 075419-1 – 075419-9 (2002).

71. R.F.W. Pease, "Nanolithography and its prospects as a manufacturing technology," *J. Vac. Sci. Technol. B* **10**(1), 278-285 (1992).

72. H.I. Smith and M.L. Schattenburg, "X-ray lithography, from 500 nm to 30 nm: X-ray nanolithography," *IBM J. Res. Develop.* **37**(3), 319-329 (1993).

73. A.D. Wilson, "X-ray lithography at IBM, 1980-1992, the development years," *IBM J. Res. Develop.* **37**(3), 299-318 (1993).

74. E. Spiller, "Early history of X-ray lithography at IBM," *IBM J. Res. Develop.* **37**(3), 291-297 (1993).

75. J.C. Hulteen and R.P. Van Duyne, "Nanosphere lithography: A materials general fabrication process for periodic particle array surfaces," *J. Vac. Sci. Technol. A,* **13**(3), 1553-1558 (1995).

76. C.L. Haynes and R.P. Van Duyne, "Nanosphere lithography: A versatile nanofabrication tool for studies of size-dependent nanoparticle optics," *J. Phys. Chem. B* **105**, 5599-5611 (2001).

77. A.D. Ormonde, E.C.M. Hicks, J. Castillo, and R.P. Van Duyne, "Nanosphere lithography: Fabrication of large area Ag nanoparticle arrays by convective self-assembly and their characterization by scanning UV-Vis extinction spectroscopy," *Langmuir* **20**, 6927-6931 (2004).

78. M.D. Malinsky, L. Kelly, G.C. Schatz, and R. P. Van Duyne, "Nanosphere lithography: Effect of the substrate on the localized surface plasmon resonance spectrum of silver nanoparticles," *J. Phys. Chem. B* **105**, 2343-2350 (2001).

79. J.C. Hulteen, D.A. Treichel, M.T. Smith, M.L. Duval, T. R. Jensen, and R. P. Van Duyne, "Nanosphere lithography: Size-tunable silver nanoparticle and surface cluster arrays," *J. Phys. Chem. B* **103**, 3854-3863 (1999).

80. T.R. Jensen, M.D. Malinsky, C.L. Haynes, and R.P. Van Duyne, "Nanosphere lithography: Tunable localized surface plasmon resonance spectra of silver nanoparticles," *J. Phys. Chem. B* **104**, 10549-10556 (2000).

81. C.L. Haynes, A.D. McFarland, M.T. Smith, J.C. Hulteen, and R.P. Van Duyne, "Angle-resolved nanosphere lithography: Manipulation of nanoparticle size, shape, and interparticle spacing," *J. Phys. Chem. B*. **106**, 1898-1902 (2002).

82. M.D. Malinsky, L. Kelly, G.C. Schatz, and R.P. Van Duyne, "Chain length dependence and sensing capabilities of the localized surface plasmon resonance of silver nanoparticles chemically modified with alkanethiol self-assembled monolayers," *J. Am. Chem. Soc.* **123**, 1471-1482 (2001).

83. A.J. Haes, S. Zou, G.C. Schatz, and R.P. Van Duyne, "A nanoscale optical biosensor: The long range distance dependence of the localized surface plasmon resonance of noble metal nanoparticles," *J. Phys. Chem. B*. **108**, 109-116 (2004).

84. A.J. Haes, S. Zou, G.C. Schatz, and R.P. Van Duyne, "A nanoscale optical biosensor: The short range distance dependence of the localized surface plasmon resonance of silver and gold nanoparticles," *J. Phys. Chem. B* **108**, 6961-6968 (2004).

85. D.A. Stuart, A.J. Haes, C R. Yonzon, E.M. Hicks, and R.P. Van Duyne, "Biological applications of localized surface plasmon resonance phenomenae," *IEEE Proc. Nanobiotechnol.* **152**, 13-32 (2005).

86. P.Markiewicz and M.C. Goh, "Atomic force microscopy probe tip visualization and improvement of images using a simple deconvolution procedure," *Langmuir* **10**, 5-7 (1994).

87. J.L. Hutter and J. Bechhoefer, "Calibration of atomic-force microscope tips," *Rev. Sci. Instrum*. **64**(7), 1868-1873 (1993).

88. Y. Li and S.M. Lindsay, "Polystyrene latex particles as size calibration for the atomic force microscope," *Rev. Sci. Instrum*. **62**(1), 2630-2633 (1991).

89. C. Bustamante, J. Vesenka, C.L. Tang, W. Rees, M. Guthold, and R. Keller, "Circular DNA molecules imaged in air by scanning force microscopy," *Biochemistry* **31**, 22-26 (1992).

90. S. Link, M.B. Mohamed, and M.A. El-Sayed, "Simulation of optical absorption spectra of gold nanorods as a function of their aspect ratio and the effect of the medium dielectric constant," *J. Phys. Chem. B* **103**, 3073-3077 (1999).

91. S. Link and M.A. El-Sayed, "Spectral properties and relaxation dynamics of surface plasmon electronic oscillations in gold and silver nanorods and nanodots," *J. Phys. Chem. B* **103**, 8410-8426 (1999).

92. B.T. Draine, and P.J. Flatau, "Discrete dipole approximation for scattering calculations," *J. Opt. Soc. Am. A* **11**(4), 1491-1499 (1994).

93. B.T. Draine, "The discrete dipole approximation for light scattering by irregular targets," in *Light Scattering by Nonspherical Particles: Theory, Measurements, and Geophysical Applications*, Ed. M. I. Mishchenko, J. W. Hovenier, & L. D. Travis, Academic Press, New York, NY,131-145 (2000).

94. E.M. Purcell and C.R. Pennypacker, "Scattering and absorption of light by nonspherical dielectric grains," *Astrophysical J.* **186**, 705-714 (1973).

95. N. Félidj, J. Aubard and G. Lévi, "Discrete dipole approximation for ultraviolet-visible extinction spectra simulation of silver and gold colloids," *J. Chem. Phys*., **111**(3), 1195-1208 (1999).

96. C.F. Bohren and D.R. Huffman, *Absorption and Scattering of Light by Small Particles,* Wiley-Interscience Publishers, New York, NY (1983).

97. W.-H. yang, G.C. Schatz and R.P. Van Duyne, "Discrete dipole approximation for calculating extinction and Raman intensities for small particles with arbitrary shapes," *J. Chem. Phys.* **103**(3), 869-875 (1995).

98. *Program DDSCAT.6.0* by B.T. Draine, Princeton University Observatory, Princeton NJ, and P.J. Flatau, University of California, San Diego, Scripps Institute of Oceanography, La Jolla, CA.

99. B.T. Draine and P.J. Flatau, *User Guide for the Discrete Dipole Approximation Code DDSCAT.6.0*, http://arxiv.org/abs/astro-ph/0309069 (2003).

100. E.D. Palik, *Handbook of Optical Constants of Solids*, Academic Press, New York, NY (1985).

101. U. Kreibig and M. Vollmer, *Optical Properties of Metal Clusters*, Springer-Verlag, New York, NY (1995).

102. K.L. Kelly, E. Coronado, L.L. Zhao and G.C. Schatz, "The optical properties of metal nanoparticles: The influence of size, shape and dielectric environment," *J. Phys. Chem. B*, **107**, 668-677 (2003).

103. M. Brust, M. Walker, D. Bethell, D. J. Schiffrin, and R.Whyman, ''Synthesis of thiol-derivatised gold nanoparticles in a two-phase liquid–liquid system,'' *J. Chem. Soc. Chem. Commun.* **23**, 801–802(1994).

104. R. G. Freeman, K. C. Grabar, K. J. Allison, R. M. Bright, J.A. Davis, A. P. Guthrie, M. B. Hommer, M. A. Jackson, P.C. Smith, D. G. Walter, and M. J. Natan, "Self-assembled metal colloid monolayers: An approach to SERS substrates," *Science* **267**, 1629–1632 (1995).

105. U. Kreibig, M. Gartz, and A. Hilger, "Mie resonances: Sensors for physical and chemical cluster interface properties," *Ber. Bunsenges. Phys. Chem.* **101**, 1593-1604 (1997).

106. A.J. Haes, W.P. Hall, L. Chang, W. L. Klein, and R. P. Van Duyne, "A localized surface plasmon resonance biosensor: First steps toward an assay for Alzheimer's disease," *Nano Lett.*, **4**, 1029-1034 (2004).

107. A.J. Haes, L. Chang, W.L. Klein, and R.P. Van Duyne, "Detection of a biomarker for Alzheimer's disease from synthetic and clinical samples using a nanoscale optical biosensor," *J. Am. Chem. Soc.* **127**, 2264-2271 (2005).

108. G.C. Schatz and R.P. Van Duyne "Electromagnetic mechanism of surface-enhanced spectroscopy," in *Handbook of Vibrational Spectroscopy*, Ed. J.M. Chalmers and P.R. Griffiths, John Wiley & Sons Ltd, Chichester, England (2002).

109. K.L. Kelly, E. Coronado, L.L. Ahao and G.C. Schatz, "The optical properties of metal nanoparticles: The influence of size, shape and dielectric environment," *J. Phys. Chem. B* **107**, 668-677 (2003).

110. M. Kerker, *The Scattering of Light and Other Electromagnetic Radiation*, Academic, New York, NY (1969).

111. T.S. Ahmadi, Z.L. Wang, T.C. Green, A. Henglein and M.A. El Sayed, "Shape controlled synthesis of colloidal platinum nanoparticles," *Science* **272**, 1924-1926 (1996).

112. S. Oldenburg, R. D. Averitt, S. Westcott, and N. J. Halas, "Nanoengineering of optical resonances," *Chem. Phys. Lett.* **288**, 243-247 (1998).

113. S. L. Westcott, S. J. Oldenburg, T. R. Lee and N. J. Halas, "Construction of simple gold nanoparticle aggregates with controlled plasmon-plasmon interactions," *Chem. Phys. Lett.* **300**, 651-655 (1999).

114. S. J. Oldenburg, G. D. Hale, J. B. Jackson, and N. J. Halas, "Light scattering from dipole and quadrupole nanoshell antennas," *Appl. Phys. Lett.* **75**, 1063-1065 (1999).

115. R. D. Averitt, S. L. Westcott, and N. J. Halas, "The linear optical properties of gold nanoshells," *J. Opt. Soc. Am. B* **16**(10), 1824-1832 (1999).

116. S. J. Oldenburg, J. B. Jackson, S. L. Westcott, and N. J. Halas, "Infrared extinction properties of gold nanoshells," *Appl. Phys. Lett.* **75**, 2897-2899 (1999).

117. R. D. Averitt, S. L. Westcott, and N. J. Halas, "The ultrafast optical properties of gold nanoshells," *J. Opt. Soc. Am.* **16**, 1814-1819 (1999).

118. S. J. Oldenburg, S. L. Westcott, R. D. Averitt, and N. J. Halas, "Surface enhanced Raman scattering in the near infrared using metal nanoshell substrates," *J. Chem. Phys.* **111**, 4729-4735 (1999).

119. J. B. Jackson and N. J. Halas, "Silver nanoshells: Variations in morphologies and optical properties," *J. Phys. Chem. B* **105**, 2743-2746 (2001).

120. N. Halas, "The Optical Properties of Nanoshells," *Optics and Photonics News*, 26-30 (Aug 2002).

121. S. L. Westcott, J. B. Jackson, C. Radloff, and N. J. Halas, "Relative contributions to the plasmon lineshape of metal nanoshells," *Phys. Rev. B*. **66**, 155431-1554315 (2002).

122. E. Prodan, P. Nordlander, and N. J. Halas, "Effects of dielectric screening on the optical properties of metallic nanoshells," *Chemical Physics Letters* **368**, 94-101 (2003).

123. J. B. Jackson, S. L. Westcott, L. R. Hirsch, J. L. West, and N. J. Halas "Controlling the surface enhanced Raman effect via the nanoshell geometry," *Appl. Phys. Lett*., **82**, 257-260 (2003).

124. E. Prodan, P. Nordlander, and N. J. Halas, "Electronic structure and optical properties of gold nanoshells," *Nano Letters* **3**, 1411-1415 (2003).

125. F. Tam, C. Moran, and N.J. Halas "Geometrical parameters controlling sensitivity of nanoshell plasmon resonances to changes in dielectric environment," *J. Phys. Chem. B* **108**, 17290-17294 (2004).

126. N.K. Grady, N.J. Halas, and P. Nordlander, "Influence of dielectric function properties on the optical response of plasmon resonant metallic nanoparticles," *Chem. Phys. Lett.* **399**, 167-171 (2004).

127. Colleen L. Nehl, Nathaniel K. Grady, Glenn P. Goodrich, Felicia Tam, Naomi J. Halas, and Jason H. Hafner, "Scattering spectra of single gold nanoshells," *Nano Letters* **4**, 2355-2359 (2004).

128. J. B. Jackson and N. J. Halas, "Surface-enhanced Raman scattering on tunable plasmonic nanoparticle substrates," *Proc. Natl. Acad. Sci. USA* **101**, 17930-17935 (2004).

129. A.L. Aden and M. Kerker, "Scattering of electromagnetic waves from two concentric spheres," *J. Appl. Phys*. **22**, 1242-1246 (1951).

130. A.E. Nieves and M.H. Brinboim, "Composite structures for the enhancement of non-linear optical susceptibility," *J. Opt. Soc. Am. B* **6**, 787-796 (1989).

131. D.G. Georganopoulou, L. Chang, J.-M. Nam, C.S. Thaxton, E.J. Mufson, W.L. Klein, and C.A. Mirkin, "Nanoparticle-based detection in cerebrospinal fluid of a soluble pathogenic biomarker for Alzheimer's disease," *Proc. Natl. Acad. Sci. USA* **102**(7), 2273-2276 (2005).

132. C.D. Keating, "Nanoscience enables ultrasensitive detection of Alzheimer's biomarker," *Proc. Natl. Acad. Sci. USA* **102**(7), 2263-2264 (2005).

133. B.W. Ahn, D.U. Song, Y.D. Jung, K.O. Chay, M.A. Chung, S.Y. Yang, and B.A. Shin, "Detection of β-amyloid peptide aggregation using DNA electrophoresis," *Analytical Biochemisty* **284**, 401-405 (2000).

134. W.L. Klein, G.A. Krafft, and C.E. Finch, "Targeting small Aβ oligomers: The solution to an Alzheimer's disease conundrum," *Trends in Neuroscience*s **24**(4), 219-224 (2001).

135. A. Lomakin, D.S. Chung, G.B. Benedek, D.A. Kirschner, and D.B. Teplow, "On the nucleation and growth of amyloid β-protein fibrils: Detection of nuclei and quantitation of rate constants," *Proc. Natl. Acad. Sci. USA*, **93**, 1125-1129 (1996).

136. J.A. Hardy and G.A. Higgins, "Alzheimer's disease: The amyloid cascade hypothesis," *Science* **256**, 184-185 (1992).

137. M.B. Podlisny, B.L. Ostaszewski, S.L. Squazzo, E.H. Koo, R.E. Rydell, D.B. Teplow, and D.S. Selkoe, "Aggregation of secreted amyloid β-protein into

sodium dodecyl sulfate-stable oligomers in cell culture," *J. Biol. Chem.* **270**(16), 9564-9570 (1995).

138. S. Prussiner, R. Rosenberg, S. Di Mauro, and R. Barche, Eds, *The Molecular and Genetic Basis of Neurological Disease*, 2nd Ed., Butterworth-Heinemann, Boston, MA, (1997).

139. S.Y. Bookheimer, M.H. Strojwas, M.S. Cohen, A.M. Saunders, M.A. Pericak-Vance, J.C. Mazziotta, and G.W. Small, "Patterns of brain activation in people at risk for Alzheimer's disease," *N. Engl. J. Med.* **343**(7), 450-456 (2000).

140. J. Golomb, A. Kluger, M.J. de Leon, S.H. Ferris, M. Mittelman, J. Cohen, and A.E. George, **"**Hippocampal formation size predicts declining memory performance in normal aging," *Neurology* **47**, 810-813 (1996).

141. E.M. Reiman, R.J. Caselli, L.S. Yun, K. Chen, D. Bandy, S. Minoshima, S.N. Thibodeau, and D. Osborne, "Preclinical evidence of Alzheimer's disease in persons homozygous for the ε4 allele for apolipoprotein E," *N. Engl. J. Med.*, **334**(12), 752-758 (1996).

142. M. Pitschke, R. Prior, M. Haupt, and D. Riesner, "Detection of single amyloid β-protein aggregates in the cerebrospinal fluid of Alzheimer's patients by fluorescence correlation spectroscopy," *Nature Medicine* **4**(7), 832-834 (1998).

143. J.-M. Nam, C.S. Thaxton, and C.A. Mirkin, "Nanoparticle based bio-barcodes for the ultrasensitive detection of proteins," *Science* **301**, 1884-1886 (2003).

144. J.-M. Nam, S.I. Stoeva, and C.A. Mirkin, "Bio-barcode based DNA detection with PCR like sensitivity," *J. Am. Chem. Soc.* **126**, 5932-5933 (2004).

145. R. Khurana, V.N. Uversky, L. Nielsen, and A.L. Fink, "Is Congo Red an amyloid-specific dye ?" *J. Biol. Chem.* **276**(25), 22715-22721 (2001).

146. T. Miura, C. Yamamiya, M. Sasaki, K. Suzuki, and H. Takeuchi, "Binding mode of Congo Red to Alzheimer's amyloid β-peptide studied by UV Raman spectroscopy," *J. Raman Spectrosc*. **33**, 530-535 (2002).

147. V.A. Iconomidou, G.D. Chryssikos, V. Gionis, A. Hoenger, and S.I. Hamodrakas, "FT-Raman spectroscopy as diagnostic tool of Congo Red binding to amyloids," *Biopolymers (Biospectroscopy)* **72**, 185-192 (2003).

148. J. Sajid, A. Elhaddaoui, and S. Turrell, "Investigation of the binding of Congo Red to amyloid in Alzheimer's diseased tissue," *Journal of Molecular Structure* **408/409**, 181-184 (1997).

149. A. Elhaddaoui, J.C. Merlin, A. Delacourte, and S. Turrell, "Spectroscopic studies of the effect of pH on the interaction between Congo Red and amyloid-type proteins," *Journal of Molecular Structure*, **267**, 113-116 (1992).

150. A. Elhaddaoui, A. Delacourte, and S. Turrell, "Spectroscopic study of Congo Red and thioflavin binding to amyloid-like proteins," *Journal of Molecular Structure* **294**, 115-118 (1993).

151. A. Lorenzo and B.A. Yankner, "β-amyloid neurotoxicity requires fibril formation and is inhibited by Congo Red," *Proc. Natl. Acad. Sci. USA* **91**, 12243-12247 (1994).

152. C.D. Hock, U. Konietzko, A. Papassotiropoulos, A. Wollmer, J. Streffer, R.C. von Rotz, G. Davey, E. Moritz, and R.M. Nitsch, "Generation of antibodies

specific for β-amyloid by vaccination of patients with Alzheimer disease," *Nat. Med.* **8**, 1270-1275 (2002).

153. T. Town, J. Tan, N. Sansone, D. Obregon, T. Klein, and M. Mullan, "Characterization of murin immunoglobulin G antibodies against human amyloid-β_{1-42} ,"*Neurosci. Lett.*, **307**, 101-104 (2001).

154. J.E. Henry, "Development of nano-scale and biomimetic surfaces for biomedical applications," Chemical Engineering, Dissertation, Texas A&M University (2005).

155. T. Ariga, K. Kobayashi, A. Hasegawa, M. Kiso, H. Ishida, and T. Miyatake, "Characterization of high affinity binding between gangliosides and amyloid β-protein," *Arch. Biochem. Biophys.* **388**, 225-230, (2001).

156. S. Wang, D. Rymer, and T. Good, "Reduction in cholesterol and sialic acid content protects cells from toxic effects of β-amyloid peptides," *J. Biol. Chem.* **276**, 42027-42034 (2001).

157. L. Choo-Smith, W. Garzon-Rodriguez, C.G. Glabe and W.K. Surewicz, "Acceleration of amyloid fibril formation by specific binding of Aβ(1-40) peptide of ganglioside containing vesicles," *J. Biol. Chem.* **272**, 22987-22990 (1997).

158. K. Matsuzaki and C. Horikiri, "Interactions of amyloid β-peptide (1-40) with ganglioside containing membranes," *Biochem.* **38**, 4137-4142 (1999).

159. Product information for sulfo-N-hydroxy-succinimido-nanogold labeling reagent, Rev. 1.4, Nanoprobes Incorporated, Yaphank, NY (March 2000), http://www.nanoprobes.com/Inf2025.html.

160. J. Dong, C.S. Atwood, V.E. Anderson, S.L. Siedlak, M.A. Smith, G. Perry, and P.R. Carey, "Metal binding and oxidation of amyloid-β within isolated senile plaque cores: Raman microscopic evidence," *Biochemistry* **42**, 2768-2773 (2003).

161. Product instruction for 1-ethyl-3-[3-dimethylaminopropyl]carbodiimide hydrochloride (EDC) attachment to proteins, Pierce Biotechnology Inc., Rockford, IL (May 2002), http://www.piercenet.com/Objects/View.cfm?type.

162. K. M. Omberg, J. C. Osborn, S. L. Zhang, J. P. Freyer, J. R. Mourant and J. R. Schoover, "Raman spectroscopy and factor analysis of tumerogenic and non-tumerogenic cells," *Applied Spectroscopy* **56**(7), 813-819 (2002).

163. T.M. Willey, A.L. Vance, T. van Buuren, C. Bostedt, L.J. Terminello, and C.S. Fadley, "Rapid degradation of alkanethiol-based-self-assembled monolayers on gold in ambient laboratory conditions," *Surf. Sci.* **576**, 188-196 (2005).

164. J. Swarbrick, Ed. *Encyclopedia of Pharmaceutical Technology*, 2nd Ed., Mercel Dekker Publishers, New York, NY (2004).

165. J.-X Cheng, Y. K. Jia, G. Zheng, and X.S. Xie, "Laser scanning coherent anti-Stokes Raman scattering microscopy and applications to cell biology," *Biophys. J.* **83**, 502-509 (2002).

166. W. E. Huang, R. I. Griffiths, I. P. Thompson, M. J. Mailey and A. S. Whiteley, "Raman microscopic analysis of single microbial cells," *Anal. Chem*.**76**, 4452-4458 (2004**).**

167. I. Notingher, S. Verrier, S. Haque, J. M. Polak and L. L. Hench, "Spectroscopic study of human lung epithelial cells (A549) in culture: Living cells versus dead cells," *Biopolymers (Biospectroscopy)* **72**, 230-240 (2003)**.**

168. S. Verrier, I. Notingher, J. M. Polak and L. L. Hench, "*In situ* monitoring of cell death using Raman microspectroscopy," *Biopolymers* **74**, 157-162 (2004)**.**

169. L. R. Hirsch, R. J. Stafford, J. A. Bankson, S. R. Sershen, B. Rivera, R. E. Price, J. D. Hazle, N. J. Halas and J. L. West "Nanoshell-mediated near-infrared thermal therapy of tumors under magnetic resonance guidance," *Proc. Natl. Acad. Sci. USA* **23**, 13549-13554 (2003).

170. E. S. Reynolds, "The use of lead citrate at high pH as an electron-opaque stain in electron microscopy," *J. Cell Biol.* **17**, 208-212 (1963).

171. B. Alberts, D. Bray, J. Lewis, M. Raff, K. Roberts, and J.D. Watson, *Molecular Biology of the Cell*, 3rd Ed., Garland Publishing, New York , NY (1994).

172. K. Sokolov, M. Follen, J. Aaron, A. Pavlova, A. Malpica, R. Lotan, and R. Richards-Kortum, "Real-time vital optical imaging of precancer using anti-epidermal growth factor receptor antibodies conjugated to gold nanoparticles," *Cancer Res.* **63**, 1999-2003 (2003).

173. K.W Short, S. Carpenter, J.P. Freyer, and J.R. Mourant, "Raman spectroscopy detects biochemical changes due to proliferation in mammalian cell culture," *Biophys. J.*, preprint (2005).

174. I. Notingher, J. Selvakumaran and L. Hench, "New detection system for toxic agents based on continuous spectroscopic monitoring of living cells," *Biosensors and Bioelectronics* **20**, 780-789 (2004).

175. N.M Sijtsema, C. Otto, G.M.J. Segers-Nolten, A.J. Verhoeven, and J. Greve, "Resonance Raman microspectroscopy of myeloperoxidase and cytochrome b_{558} in human neutrophilic granulocytes," *Biophys. J.* **74**, 3250 – 3255 (1998),

176. J. Roskam and L. Rogers, Ed., *Lab Reference*, Cold Spring Harbor Laboratory Press, New York, NY (2002)**.**

177. E. Alexandratou, D. Yova, P. Handris, D. Kletsas, and S. Loukas, "Human fibroblast alterations induced by low power laser irradiation at the single cell level using confocal microscopy," *Photochem. Photobiol. Sci.* **1**, 547-552 (2002).

178. C. Estavillo, Z. Lu, I. Jansson, J.B. Schenkman, and J.F. Rusling, "Epoxidation of styrene by human cyt P450 1A2 by thin film electrolysis and peroxide activation compared to solution reactions," *Biophysical Chemistry* **104**, 291-296 (2003).

179. K. Keipp, R.R. Dasari and Y. Wang, "Near-infrared surface-enhanced Raman scattering (NIR SERS) of colloidal silver and gold," *Appl. Spectrosc.* **48**(8), 951-955 (1994).

180. K. Kneipp, H. Kneipp, R. Manoharan, E.B. Hanlon, I. Itzkan, R.R. Dasari and M.S. Feld, "Extremely large enhancement factors in surface-enhanced Raman scattering for molecules on colloidal gold clusters," *Appl. Spectrosc.* **52**(12), 1493-1497 (1998).

181. D.A. Skoog, F.J. Holler, and T.A. Nieman, *Principles of Instrumental Analysis,* Saunders College Publishing, Orlando, FL (1998).

182. M. Kerker, O. Siman, L.A. Bumm, and D.-S. Wang, "Surface enhanced Raman scattering (SERS) of citrate ion adsorbed on colloidal silver," *Appl. Opt*. **19**, 3253-3255 (1980).

183. H. Xu, J. Aizpurua, M. Käll and P. Apell, "Electromagnetic contributions to single-molecule sensitivity in surface-enhanced Raman scattering," *Phys. Rev. E*, **62**, 4318-4324 (2000).

APPENDIX A

INTRODUCTION TO RAMAN SCATTERING

When light is incident on matter (such as a biological cell or tissue), it can interact with atoms and molecules in several different ways. The photons of the incident light can be either absorbed directly or scattered by the target. Absorption of light occurs when the incident radiation either causes excitation of vibrational modes in the target molecule (IR-absorption) or causes excitation of the electronic transitions in the target (UV-Visible Absorption). Sometimes electronic state excitation events are followed by radiative emission of light by the target at longer wavelengths. This phenomenon is called fluoresence and is exploited widely in biomedical research.

When light is scattered from a molecule, most photons are elastically scattered at the same wavelength as the incident light. However, a small fraction of light is scattered at optical frequencies different from the frequency of the incident radiation. This inelastic scattering of photons is called Raman scattering. An energy transfer occurs as a result of the coupling between the incident radiation and target molecule which can be described by the following set of equations:

When a beam of radiation having a frequency ν_{ex} is incident upon a target molecule, the electric field E of this radiation can be expressed by the following equation:[181]

$$E = E_0 \cos(2\pi\nu_{ex}t) \qquad \text{Eq. A.1}$$

where E_0 is the amplitude of the wave. When the electric field of the radiation interacts with an electron cloud of an analyte bond, it induces a dipole moment m in the bond that is expressed as:[181]

$$m = \alpha E = \alpha E_0 \cos(2\pi\nu_{ex}t) \qquad \text{Eq. A.2}$$

where α is a proportionality constant called the polarizability of the bond, and is a measure of the deformability of the bond in a electric field. In order to be Raman active, the polarizability α of a bond must vary as a function of the distance between nuclei according to the equation:[181]

$$\alpha = \alpha_0 + (r - r_{eq})\left(\frac{\partial \alpha}{\partial r}\right) \qquad \text{Eq. A.3}$$

where α_0 is the polarizability of the bond at the equilibrium internuclear distance r_{eq} and r is the internuclear separation at any instant. The change in internuclear separation varies with the frequency of vibration ν_v as given by:[181]

$$r - r_{eq} = r_m \cos(2\pi \nu_v t) \qquad \text{Eq. A.4}$$

where r_m is the maximum inter-nuclear separation relative to the position. Substituting Eq. A.4 into Eq. A.3 then gives:[181]

$$\alpha = \alpha_0 + \left(\frac{\partial \alpha}{\partial r}\right) r_m \cos(2\pi \nu_v t) \qquad \text{Eq. A.5}$$

By substituting Eq.A.5 into Eq.A.2 along with the judicious use of elementary trigonometric identities, a final expression for the induced dipole moment *m* can be obtained:[181]

$$m = \alpha_0 E_0 \cos(2\pi \nu_{ex} t) + \frac{E_0}{2} r_m \left(\frac{\partial \alpha}{\partial r}\right) \cos[2\pi(\nu_{ex} - \nu_v)t] +$$
$$\frac{E_0}{2} r_m \left(\frac{\partial \alpha}{\partial r}\right) \cos[2\pi(\nu_{ex} + \nu_v)t] \qquad \text{Eq. A.6}$$

The first term in the above equation represents Rayleigh scattering which occurs at the excitation frequency ν_{ex}. The second and third terms in Eq. A.6 correspond to the Stokes

and Anti-Stokes frequencies of ν_{ex} - ΔE and ν_{ex} + ν_{v} respectively. Thus it is seen that the excitation frequency is modulated by the vibrational frequency of the bond. Eq. A.6 also displays another important point i.e. Raman scattering requires that the polarizability of the bond varies as a function of distance i.e. $\partial\alpha/\partial r$ has to be greater than zero for Raman lines to appear. It is important to note that the magnitude of the of the Raman shifts (dependent only on ν_{v}) is independent of the wavelength of the incident radiation.

Generally Rayleigh scattering has a much higher probability of occurring than Raman scattering because the most probable event is the energy transfer to molecules in the ground state and re-emission by the return of these molecules to the ground state (typical Rayleigh scattering cross sections of molecules are in the range of $\sigma = 10^{-26}$ cm^2 and typical Raman scattering cross sections are in the range of $\sigma = 10^{-29}$ cm^2).[1,181] A pictorial representation of Raman and Rayleigh scattering is as follows:[181]

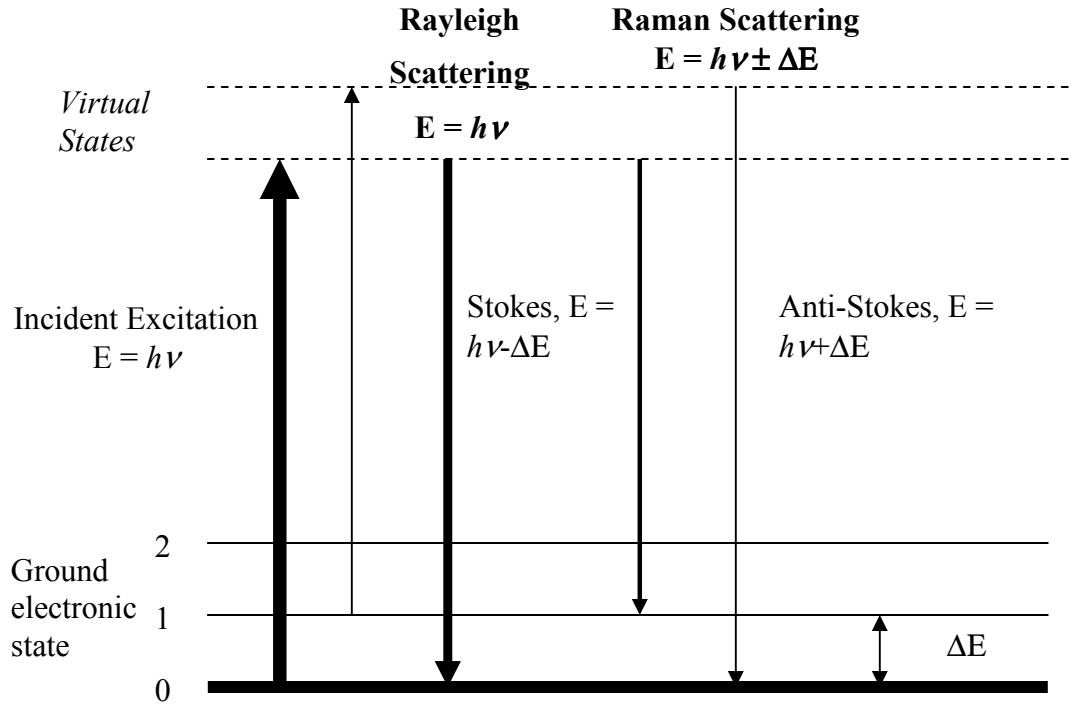

Figure A.1: Pictorial description of Rayleigh and Raman Scattering. Diagram adapted from Skoog *et al*. [181]

The heavy arrow on the far left in Figure A.1 depicts the energy change in a molecule when it interacts with an incident photon from the source. The increase in energy is equal to the energy of the photon hν, where h is the Planck constant of 6.62608 $\times 10^{-34}$ J s. This process is however not quantized and so depending on the frequency of radiation of the source, the energy of the molecule can assume any of an infinite number of values or *virtual states* between the ground state and first electronic state.[1,181] The second upward arrow on the left depicts the situation that occurs when the molecule encountered by the incident photon is already in the first vibrational level of the ground state (for example at high temperatures). Generally at room temperature, this is quite a rare event as most molecules at room temperature are in their lowest vibrational state.

Hence the thin width of the arrow depicting this event shows its low probability of occurrence. The set of arrows in the middle shows the changes occurring in the target molecule that causes Rayleigh scattering. Here too the width of the arrows shows the probability of the occurrence of the event. It is important to note that there is no loss of energy during Rayleigh scattering events. As a result the collisions between the incident photons and target molecule are termed *elastic* in nature. The changes in the molecule that produces Stokes and Anti-Stokes Raman scattering are depicted by the two arrows on the right of Figure A1. The two differ from the Rayleigh scattered radiation by energies of $\pm \Delta E$, which is the energy of the first vibrational level of the ground state. [181] Generally at room temperature the intensity of the Stokes shifted Raman bands are higher than the Anti-Stokes band. This ratio of intensities begins to change in favor the Anti-Stokes band with increasing temperature as a larger fraction of a target molecule are expected to be in the first vibrationally excited states under such circumstance.[181]

An interesting point to note is that for a Raman active bond which is also infrared active, the energy of the IR absorption would also be ΔE. Hence the Raman frequency shift and the infrared absorption peak frequency of such a bond would be identical. [181] Although the Raman signature and the IR signature of a molecule are dependent upon the same vibrational modes, they arise from processes that are mechanistically different. IR absorption requires that a vibrational mode of a molecule have a change in dipole moment or charge distribution associated with it. Only in such an event can radiation of the same frequency interact with the molecule and promote it to an excited vibrational state. [181] Raman scattering on the other hand, involves a momentary distortion of the

electrons distributed around a bond in a molecule, which is then followed by reemission of the radiation as the bond returns to its normal state. In its distorted form the molecule is temporarily polarized – i.e. it develops a momentarily induced dipole that disappears upon relaxation. As a result of the mechanistic differences thus described, the Raman activity of a given vibrational mode may differ markedly from its infrared activity. [181] This difference is clearly illustrated in the case of homonuclear molecules such as nitrogen or chlorine (N_2 or Cl_2), which do not have dipole moments either in its equilibrium position or when a stretching vibration causes a change in the inter-nuclear distance. Thus the case for absorption of radiation does not exist and hence the bonds are not infrared active. However, the polarizability of the bond between the atoms in such a molecule varies periodically in phase with the stretching vibrations, reaching a maximum at the greatest separation and a minimum at the closest approach of the two nuclei. Hence these bonds are Raman active.[181] A similar situation occurs in the case of the linear molecule carbon dioxide (O-C-O) where the symmetric stretches are Raman active but infrared *in*active because there is no change in dipole moment in symmetric stretching but a change in polarizability when both the oxygen atoms either move toward (decrease in polarizability) or away form the central carbon atom (increase in polarizability). The asymmetric stretches in the molecule however are Raman *in*active and infrared active because when one of the oxygen atoms move toward the carbon and other away from it, a change in dipole moment occurs as there is a net change in charge distribution but no change in polarizability occurs because as the polarizability of one of

the bonds increases as it lengthens, the polarizability of the other decreases as it shortens.[181]

APPENDIX B

INTRODUCTION TO SURFACE ENHANCED RAMAN SCATTERING (SERS)

The relatively low efficiency of Raman scattering by molecules has always been a major obstacle that compromised the widespread use of Raman spectroscopy in scientific applications (typical Rayleigh scattering cross sections of molecules are in the range of $\sigma = 10^{-26}$ cm^2 and typical Raman scattering cross sections are in the range of $\sigma = 10^{-29}$ cm^2).[1] One of the techniques that has been used to increase the Raman signal from a molecule is Surface Enhanced Raman Spectroscopy (SERS).[2-7] SERS is a relatively recent technique which has been used quite successfully to enhance the Raman cross section of a molecule by factors of 10^6 or more.[2-7] The enhancement is generally achieved by using low to medium powered lasers to excite vibrational transitions in molecules adsorbed on or in close proximity to a rough metallic surface. The metallic surface can be in the form of a thin layer of the metallic film on an electrode or glass slide, or in the form of aqueous colloidal nanoparticles or more recently metal nanoshells. Typical metals used for SERS are gold, silver and copper. The exact nature of the enhancement of Raman signals through SERS is not fully understood but appears to be caused by two contributing mechanisms of enhancement, namely the Electromagnetic Mechanism and the Chemical Mechanism.

The Electromagnetic Mechanism (EM) which is the dominant of the two contributing mechanisms explains the enhancement process primarily due to localized surface plasmon resonance, which is the excitation of the collective oscillation of the conduction band electrons localized on a metal particle by the incident electromagnetic radiation.[2-7] The surface plasmon resonance effect causes the creation of a high energy field at the metal particle surface which decays rapidly away from it. Therefore the

incident electromagnetic field acting on an analyte molecule adsorbed onto the surface of the metal particle is increased through the addition of this high energy field from the metal particle.[2-7] Thus the analyte in close proximity to the metal nanoparticle will experience an increase in field intensity when compared to a molecule in free space (or not in proximity to the metal surface). This increase in the field intensity experienced by the analyte will lead to an increase in its Raman scattered signal. Figure B.1 shows a simple schematic illustration the concept of the electromagnetic SERS enhancement:[3]

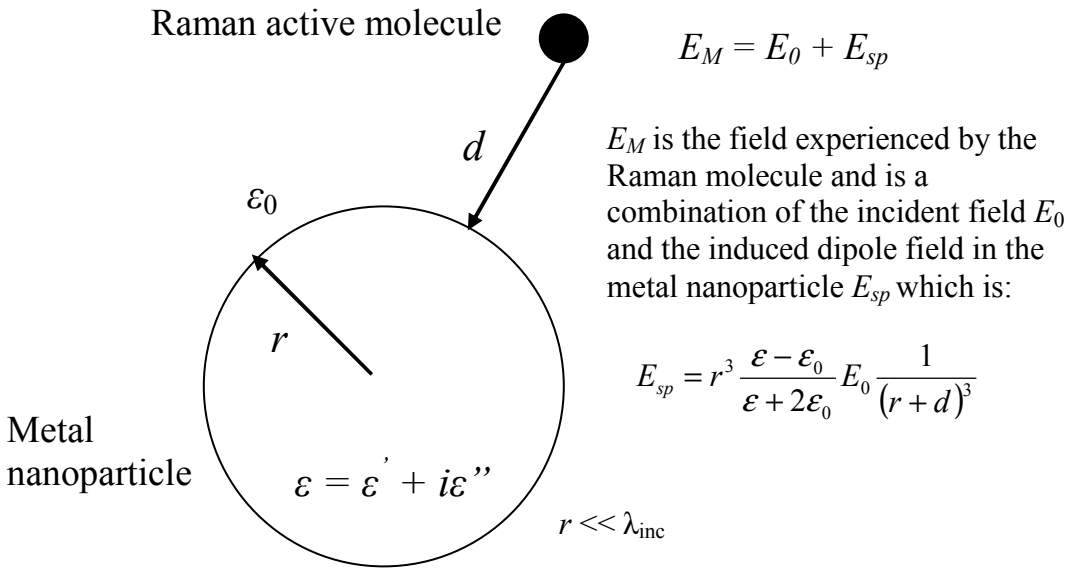

Figure B.1: Simple schematic illustrating the principles of the electromagnetic mechanism behind SERS. Adapted from Kneipp *et al.* [3]

In the above schematic the SERS substrate is represented by a small metallic sphere with radius *r* having a complex frequency dependent dielectric constant $\varepsilon(\nu) = \varepsilon' + i\varepsilon''$ where ν is the frequency and ε' and ε'' are the real and imaginary portion of the metal dielectric constant. The dielectric constant of the surrounding medium is represented as ε_0. The derivation of the expression in the simplest case assumes that the diameter of the metal nanosphere is much smaller than the wavelength of light ($2r << \lambda$) (quasistatic or Rayleigh limit). A Raman active molecule placed at a distance *d* away from the surface of the metal nanoparticle is irradiated with an incident electromagnetic wave with a field E_0. This incident electromagnetic field will induce a dipole moment in the metal nanoparticle with a field of E_{sp}. Hence the Raman active molecule will experience a field E_M which is the superposition of the incident field and the field of the dipole induced in the metal particle. This enhancement in the field experienced by the Raman active molecule by virtue of its proximity to the metal nanoparticle surface is represented by the field enhancement factor $A(\nu)$ which is defined as the ratio of the field at position of the Raman active molecule to the incoming incident field: [3]

$$A(\nu) = \frac{E_M(\nu)}{E_0(\nu)} \approx \frac{\varepsilon - \varepsilon_0}{\varepsilon + 2\varepsilon_0}\left(\frac{r}{r+d}\right)^3 \qquad \text{Eq. B.1}$$

Equation B.1 shows that the enhancement $A(\nu)$ is the strongest when the real part of $\varepsilon(\nu)$ equals $-2\varepsilon_0$. In addition the imaginary part of $\varepsilon(\nu)$ also needs to be small (i.e. metal has to be a non-absorber or poor absorber) for maximum enhancement. This condition occurs during the resonant excitation of the surface plasmons of the metal nanoparticle. The derivation assumes that the embedding medium does not have an

imaginary portion to its dielectric constant (i.e. the metal nanoparticle is embedded in a non absorbing medium).

It is not only the laser field that is enhanced by the metal nanoparticle. The Raman scattered Stokes (or Anti-Stokes) field is also enhanced in a similar manner if it is in resonance with the surface plasmons of the metal nanoparticle. Thus the metal surface acts as an amplification "antenna" which both amplifies the incident field that the Raman active molecule experiences as well as the Raman scattered field radiating off it. Hence taking into account both these enhancement steps, the total electromagnetic enhancement factor for the Raman signal intensity of a Raman band at frequency v_s can be defined as $G_{em}(v_s)$:[3]

$$G_{em}(\nu_s) = |A(\nu_L)|^2 |A(\nu_s)|^2 \approx \left| \frac{\varepsilon(\nu_L) - \varepsilon_0}{\varepsilon(\nu_L) + 2\varepsilon_0} \right|^2 \left| \frac{\varepsilon(\nu_s) - \varepsilon_0}{\varepsilon(\nu_s) + 2\varepsilon_0} \right|^2 \left(\frac{r}{r+d} \right)^{12} \qquad \text{Eq. B.2}$$

where $|A(\nu_L)|^2$ and $|A(\nu_S)|^2$ express the enhancement factors for the laser at the incident frequency (ν_L) and Raman scattered frequency (ν_s) respectively. Thus the total intensity enhancement formula shows that the enhancement scales to the fourth power of the local field of the metallic nanoparticle and it is strongest when both the excitation as well as the Raman scattered fields are in resonance with the surface plasmons of the metal nanoparticle. This occurs most efficiently for the low frequency Raman modes (lower wavenumber shift and hence closer to the surface plasmon resonance of the nanoparticle) and is one of the reasons behind the scattering powers of the Raman bands in a SERS spectrum falling off with increasing vibrational energy.[3] Although the electromagnetic SERS enhancement does not require the direct contact between a

Raman active molecule and the metal nanoparticle surface (*d* does not have to be zero), it strongly decreases with growing distance described by the decay of the field of a dipole over the distance $[1/d]^3$ to the fourth power resulting in a $[1/d]^{12}$ distance dependence.[3-4] Maximum values for the electromagnetic enhancement for isolated single colloidal silver and gold spheroids are in the order of 10^6 to 10^7. [3,182] Strong enhancement of electromagnetic fields for sharp features and large curvatures on metal nanostructures have also been predicted.[182-183] It has been previously shown that the electromagnetic SERS enhancement was as high as 10^{11} in "special" circumstances at interstitial sites between particles in nanoparticle clusters and at locations outside sharp surface protrusions in single nanoparticles.[183]

Experimental observations, however, provide compelling evidence to conclude that SERS is not an exclusively electromagnetic mechanism. If it were only an electromagnetic mechanism, then it is expected that a strong SERS signal should exist for any Raman active molecule in close proximity to an appropriate silver or gold nanoparticle surface. This however, is not so and is illustrated in the case of methanol which has a strong Raman signature but fails to show any SERS enhancement.[3] Experimental results indicate that the SERS effect has strong molecular selectivity and dependence on the chemical nature of the Raman molecule. These findings indicate the existence of an additional "chemical" SERS enhancement mechanism**.** Several mechanisms have been proposed that can be grouped together to explain this "chemical" effect of SERS. These include electronic coupling between the adsorbed Raman active molecule and the metal and formation of an adsorbate-surface complex resulting in an

increase in the Raman cross section of the adsorbed molecule, resonance Raman effects which occurs due to shifted and broadened electronic levels in the adsorbate molecule as a result of the influence of the metal, the direct charge transfer between the Raman active molecule and metal and others.[2-7] Of the different chemical mechanisms proposed, the charge transfer mechanism is the most common and involves the following steps: (a) an incident photon with energy given by frequency ω induces an intraband transition in the silver or gold nanoparticle (an electron below the Fermi level undergoes a promotion to the wise sp level over it, creating a hole in the place the electron comes from); (ii) this new "excited" electron transfers from the metal to the lowest unoccupied molecular orbital (LUMO) of the Raman active adsorbate via tunneling for physisorbed adsorbates or via hybridization for chemiadsorbates; (iii) the electron with slightly altered energy due to interactions with internal molecular vibrations in the molecule transfers from the LUMO of the adsorbate back to the metal; (iv) the electron then recombines with the hole below the Fermi level in the metal causing a photoemission at Stokes shifted frequency.[2-3]

One common element that all the proposed chemical enhancement mechanisms have is an alteration (temporary and/or permanent) in the actual Raman matrix element of the adsorbed molecule by the metal surface (i.e. there is a change in the chemical nature of the adsorbed Raman active analyte due to the influence of the metal surface).[3] Thus the chemical enhancement contributes in altering the actual Raman scattering cross section of the adsorbed analyte. The SERS enhancement caused by the chemical mechanism is generally limited to those analyte molecules in the first monolayer that are

in direct contact with the metal surface and thus is a shorter range enhancement process. In general, the chemical SERS enhancement mechanisms contribute enhancement factors on the order of 10-10^2. [3]

The Raman spectrum of a molecule is characterized by the frequency shifts, line widths and relative intensities of the Raman lines. As a result of different enhancement mechanisms for different Raman modes, a SERS spectrum can show some deviations in relative intensities when compared with a normal Raman spectrum of the same molecule. The direct interaction between molecule and metal in SERS can also cause the Raman lines of an adsorbed molecule to be slightly shifted in frequency and changed in line width when compared with a 'free' molecule. Often it is observed that the SERS spectra of an adsorbed molecule is missing some of the peaks that occur regularly in a normal Raman spectra of a "free" molecule. This can happen because the nature of the adsorption of the molecule to the metal surface as well its relative orientation to the metal can sometimes favor the selective enhancement of Raman scattering from bonds in a localized area of the molecule as opposed to others.

The total SERS signal from a Raman active molecule adsorbed on a silver or gold nanoparticle structure can be represented as:[2, 3, 7]

$$P^{SERS}(\nu_s) = N'\sigma_{ads} I(\nu_L) |A(\nu_L)|^2 |A(\nu_s)|^2 \qquad \text{Eq. B.3}$$

where $|A(\nu_L)|^2$ and $|A(\nu_s)|^2$ express the electromagnetic enhancement factors at the incident frequency (ν_L) and Raman scattered frequency (ν_s) respectively, σ_{ads} describes the increased cross section of the adsorbed Raman active molecule (due to the influence chemical enhancement mechanisms), $I(\nu_L)$ is the excitation laser intensity, and N' is the

number of analyte molecules involved in the SERS process. It can thus be seen from the above equation that the SERS signal is directly proportional to the number of molecules of the analyte in favorable proximity to the metal surface.

VITA

Name: Mustafa Habib Chowdhury

Address: Center for Fluorescence Spectroscopy, University of Maryland School of Medicine, Department of Biochemistry , 725 West Lombard Street, Baltimore, MD 21201

Email Address: nanomustafa@gmail.com

Education: B.S., Electrical Engineering, Purdue University, 1998
M.S., Electrical Engineering, California State University, Long Beach, 2000
Ph.D., Biomedical Engineering, Texas A&M University, 2005